Advancing Microbial Electrolysis Cells (MECs)

for Efficient Wastewater-to-Energy Conversion

Dissertation (monograph) approved by the Doctoral Degree Committee of
Hamburg University of Technology

in pursuit of the academic degree of

Doktorin der Naturwissenschaften (Dr. rer. nat.)

written by

Mahshid Golalikhani

from

Gorgan, Iran

2026

Reviewers:	Prof. Dr. rer. nat. Johannes Gescher
	Prof. Dr.-Ing.Ralf Pörtner
Chairman of examination committee	Prof. Dr. Felix Löffler
Date of oral examination:	27.05.2026

DOI:	https://doi.org/10.15480/882.17307
Handle:	https://hdl.handle.net/11420/63475
ORCid:	https://orcid.org/0000-0002-3856-1730

Abstract

The global energy crisis and fossil fuel impacts highlight the need for sustainable energy carriers such as hydrogen. Microbial electrolysis cells (MECs) can generate hydrogen from organic waste, but their optimization under complex feedstock conditions remains challenging. Accordingly, this study focused on optimizing key parameters to enhance MEC performance.

Variation in flow velocity (0.2 and 0.8 mm/s) in *Geobacter sulfurreducens* and *Shewanella oneidensis* co-culture biofilms, cultivated in a microfluidic bioelectrochemical system, showed that *S. oneidensis* exhibited a pronounced flow-dependent response. Higher shear stress produced thinner but more electroactive biofilms, linked to biofilm formation through mechanosensing pathways. To further evaluate system performance, the effects of substrate concentration (20–60%), pH (5–8), and applied anodic potential (−0.2 to +0.4 V vs standard hydrogen electrode [SHE]), in a cylindrical microbial electrolysis cell (Cylindrical-MEC) were also studied. Optimal performance was achieved at 40 % hydrolysate, pH 8, and +0.4 V vs. SHE, yielding a mean current density of 3.4 A/ m² and coulombic efficiencies (CE) of 95 %. Metagenomic and PCA analyses revealed that high anodic potential and alkaline pH enriched *Geobacter*-dominated communities while suppressing methanogens. In a 10-L rotating disk bioelectrochemical reactor (RDBER), operation at 0.4 V vs. SHE achieved a hydrogen production rate of 30.57 L/m²·d with minimal methane formation. The hydrogen produced under these conditions was subsequently utilized for the autotrophic synthesis of acetoin.

Zusammenfassung

Die globale Energiekrise und die Auswirkungen fossiler Brennstoffe unterstreichen die Notwendigkeit nachhaltiger Energieträger wie Wasserstoff. Mikrobielle Elektrolysezellen (MECs) können aus organischen Abfällen Wasserstoff erzeugen, doch ihre Optimierung unter komplexen Rohstoffbedingungen bleibt eine Herausforderung. Dementsprechend konzentrierte sich diese Studie auf die Optimierung wichtiger Parameter zur Verbesserung der MEC-Leistung.

Variationen in der Strömungsgeschwindigkeit (0,2 und 0,8 mm/s) in Biofilmen aus *Geobacter sulfurreducens* und *Shewanella oneidensis*, die in einem mikrofluidischen bioelektrochemischen System kultiviert wurden, zeigten, dass *S. oneidensis* eine ausgeprägte strömungsabhängige Reaktion zeigte. Eine höhere Scherspannung führte zu dünneren, aber elektroaktiveren Biofilmen, die über mechanosensorische Wege mit der Biofilmbildung in Verbindung stehen. Um die Systemleistung weiter zu bewerten, wurden auch die Auswirkungen der Substratkonzentration (20–60 %), des pH-Werts (5–8) und des angelegten anodischen Potenzials (−0,2 bis +0,4 V gegenüber der Standard-Wasserstoffelektrode [SHE]) in einer zylindrischen mikrobiellen Elektrolysezelle (Cylindrical-MEC) untersucht. Die optimale Leistung wurde bei 40 % Hydrolysat, pH-Wert 8 und +0,4 V gegenüber SHE erreicht, was eine mittlere Stromdichte von 3,4 A/m² und eine Coulomb-Effizienz von 98 % ergab. Metagenomische und PCA-Analysen zeigten, dass ein hohes anodisches Potential und ein alkalischer pH-Wert zu einer Anreicherung von *Geobacter*-dominierten Gemeinschaften führten und gleichzeitig Methanogene unterdrückten. In einem 10-L-Scheibentauchkörper, der als bioelektrochemischer Reaktor ausgelegt wurde, wurde bei einem Betrieb von 0,4 V gegenüber SHE eine Wasserstoffproduktionsrate von 30,57 L/m²·d bei minimaler Methanbildung erreicht. Der unter diesen Bedingungen erzeugte Wasserstoff wurde anschließend für die autotrophe Synthese von Acetoin verwendet.

Table of Contents

Table of Figures

List of Tables

Abbreviations

GHG	greenhouse gas
BES	bioelectrochemical systems
MEC	microbial electrolysis cells
VFA	volatile fatty acids
SHE	standard hydrogen electrode
Eeq	equilibrium potential
ARB	anode-respiring bacteria
EAB	electrochemically active bacteria
OMC	outer membrane cytochromes
EET	extracellular electron transfer
HER	hydrogen evolution reaction
COD	chemical oxygen demand
EPS	extracellular polymeric substance
c-di-GMP	cyclic di-guanosine monophosphate
DGC	diguanylate cyclases
MCR	methyl coenzyme M reductase
2-BES	2-bromoethanesulfonate
HRT	hydraulic retention time
DI water	deionized water
TOC	total organic carbon
TC	total carbon
IC	inorganic carbon
RDBR	rotating disk bioelectrochemical reactor
C-BES	cylindrical bioelectrochemical system
$OD_{600\ nm}$	optical density with $\lambda = 600$ nm
OCT	optical coherence tomography
M	molar concentration (mol/L)
EPS	extracellular polymeric substances
EET	extracellular electron transfer
H_2	hydrogen

CO_2	carbon dioxide
CO	carbon monoxide
d	day
LB	lysogeny Broth
min	minute
PDMS	Polydimethylsiloxan
rpm	rounds per minute
s	second
m	meter
mm	millimeter
Pa	pascal
CH_4	methane
PEM	proton exchange membrane
AEM	anion exchange membranes
CEM	cation exchange membranes
NADH	nicotinamide adenine dinucleotide
CE	coulombic efficiency
TCA	tricarboxylic acid
PHB	polyhydroxybutyrate

1. Introduction

Global energy demand is rising with population growth, economic development, technological progress, and changing consumption patterns. Although the use of renewable energy sources such as solar, wind, hydropower, and biofuels is growing rapidly, fossil fuels, including oil, coal, and natural gas, still dominate global energy consumption (Figure 1). This continued dominance is concerning, as they are limited resources and major contributors to greenhouse gas (GHG) emissions.

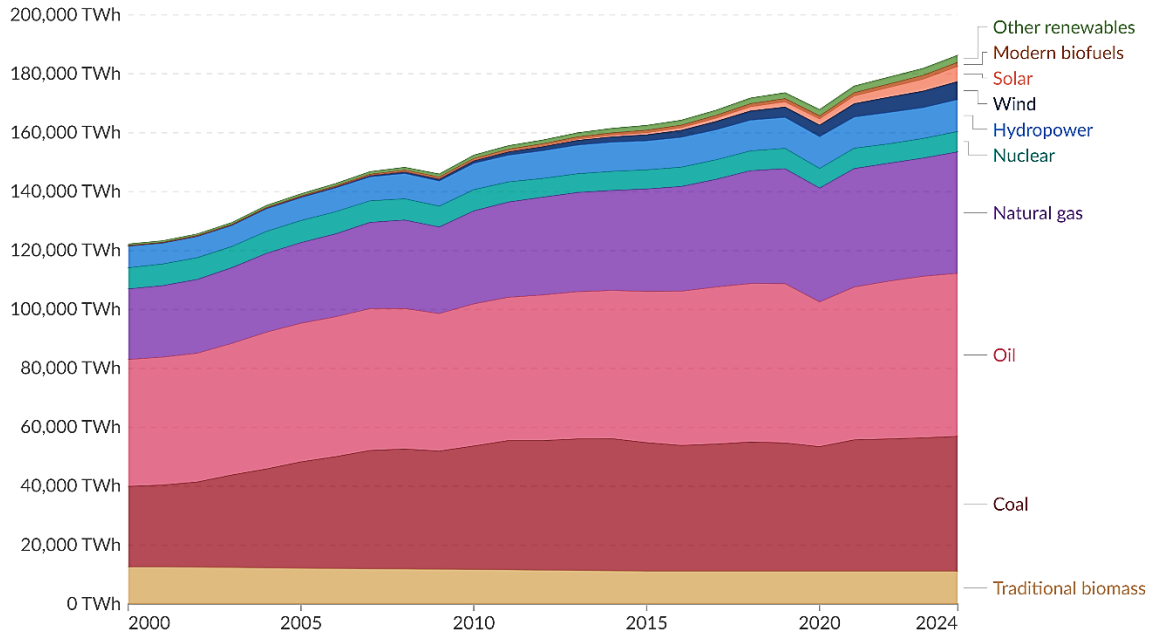

Figure 1. Global energy consumption by source, 2000–2024 (Modified from Energy Institute and Our World in Data, 2025).

To secure future energy supply and protect the environment, new technologies that are both clean and efficient are needed. Hydrogen (H_2) is now seen as an important option in this transition. It has several advantages as an energy carrier: it produces only water when used in fuel cells, it has a high energy density by weight, it can be stored and moved in different forms, and it helps integrate variable renewable energy into energy systems (Abbasian Hamedani et

al., 2024; Le et al., 2023; Reda et al., 2024). Currently, hydrogen demand is mainly in oil refining, ammonia production, and methanol synthesis (Figure 2a). However, global efforts are in progress to expand hydrogen's role in the energy mix by 2030 (Figure 2b).

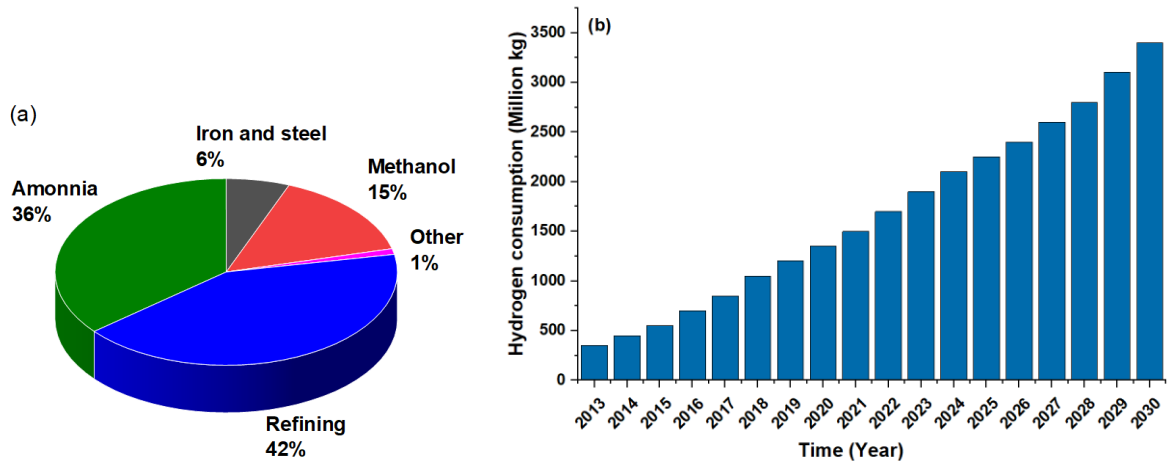

Figure 2. (a) Global hydrogen distribution by sector in 2021 (Tymofiiv et al., 2022) ; (b) Annual worldwide hydrogen consumption (Güçyetmez et al., 2025)

Currently, more than 95% of hydrogen is produced from fossil fuels, primarily through the reforming of natural gas and coal gasification. Renewable hydrogen, or green hydrogen, remains limited but is essential for reducing the carbon footprint of production. Biohydrogen contributes less than 0.1% of total output. The World Energy Council estimates that hydrogen production costs could decrease by about 50% by 2030 and may be reduced even further if hydrogen generation is integrated with wastewater treatment systems (Silva et al., 2024). Such integration supports circular economy principles by linking energy recovery with mitigating environmental pollution.

Bioelectrochemical systems (BESs) represent one of the promising technologies in this context. These systems use electroactive microorganisms to convert organic substrates into electrical or chemical energy carriers such as hydrogen, while simultaneously being able to treat wastewater and recover valuable by-products. This multifunctionality positions BESs as a valuable

complement to renewable energy systems, helping to balance variable renewable generation and contributing to sustainable hydrogen production. In this thesis, Microbial electrolysis cells (MECs) are studied as a technology to produce hydrogen while degrading organic compounds in hydrolysate from primary sludge. The following chapters focus on optimization of different parameters that influence the performance of this system and their potential for practical application in the clean energy transition.

1.1. Microbial electrolysis cells

MECs are a type of BES that combines microbial metabolism with electrochemical processes to recover energy from organic matter. MECs operate under a small applied voltage that drives additional reactions, enabling the production of reduced compounds. They have been studied for applications such as wastewater treatment, hydrogen generation, and the synthesis of value-added chemicals (Logan and Rabaey, 2012; Sleutels et al., 2012). MECs are a promising approach for sustainable energy production and integration into future low-carbon systems (Raheem et al., 2016).

1.1.1. Key components of MECs

MECs consist of main compartments that play important roles in the performance of the system:

i. Anode: Under anaerobic conditions, the anode functions as the electron acceptor, capturing electrons released when exoelectrogenic bacteria oxidize organic matter in the substrate. Carbon-based materials such as carbon felt, mesh, cloth, and graphite brushes are commonly used as anodes because they offer high conductivity, large surface area, and good biocompatibility, all of which promote microbial growth and efficient electron transfer (Banerjee et al., 2022).

ii. Cathode: the cathode functions as the reduction electrode, where electrons transferred from the anode through the external circuit combine with protons. This process predominantly yields hydrogen gas; however, depending on the system design, other reduced products, such as methane, formate, or acetate, may also be formed. To maximize hydrogen evolution efficiency, cathodes are typically fabricated from conductive and catalytically active materials, including stainless steel, nickel, carbon-based substrates, or platinum-coated electrodes (Farhangi et al., 2014; Manuel et al., 2010).

iii. Biocatalyst: Electroactive microorganisms act as biocatalysts in MECs by oxidizing organic matter and transferring the released electrons to the anode. They are found in bacteria, archaea, and eukaryotes, with well-studied examples including *Geobacter sulfurreducens*, *Shewanella oneidensis*, and *Pseudomonas aeruginosa* (Pérez-rodríguez, 2025).

iv. Substrate: The substrate refers to the organic matter oxidized by microorganisms to release electrons. Its chemical composition, biodegradability, and concentration are critical factors that influence system performance and microbial activity. Substrates may range from simple compounds such as glucose, acetate, and lactate to more complex sources, including wastewater, sludge, food waste, and lignocellulosic biomass (Pérez-rodríguez, 2025).

v. Membrane: membranes are commonly used to separate the anodic and cathodic chambers. Several types of membranes have been tested in MECs. The most common is the proton exchange membrane (PEM), such as Nafion, which allows selective proton transfer. Other options include anion exchange membranes (AEMs) like AMI-7001, cation exchange membranes (CEMs) such as CMI-7000 and Flemion, as well as

nanofiber-reinforced PEMs, forward osmosis membranes, bipolar membranes, and charge-mosaic membranes (Dange et al., 2021).

The use of membranes offers some clear advantages. They enhance hydrogen purity by reducing gas crossover and preventing oxygen diffusion into the anode chamber. This makes them useful in dual-chamber MECs, where separation between electrodes is critical. However, membranes also present significant drawbacks. They contribute to ohmic resistance, create pH gradients that reduce microbial activity and hydrogen yield, and can lead to potential losses. Membranes are also costly, prone to fouling, clogging, and biodegradation, and complicate scale-up of MEC systems due to their expense and structural complexity (Dange et al., 2021; Koul et al., 2022).

To overcome these limitations, membraneless (single-chamber) MECs have been developed. By removing the membrane, internal resistance and pH gradients are minimized, resulting in higher current density and hydrogen production rates. In addition, membraneless MECs offer simpler and more cost-effective construction while avoiding long-term challenges such as fouling and degradation, making them a promising option for practical applications (Call and Logan, 2008; Wang et al., 2023). A simplified representation of an MEC configuration is shown in Figure 3.

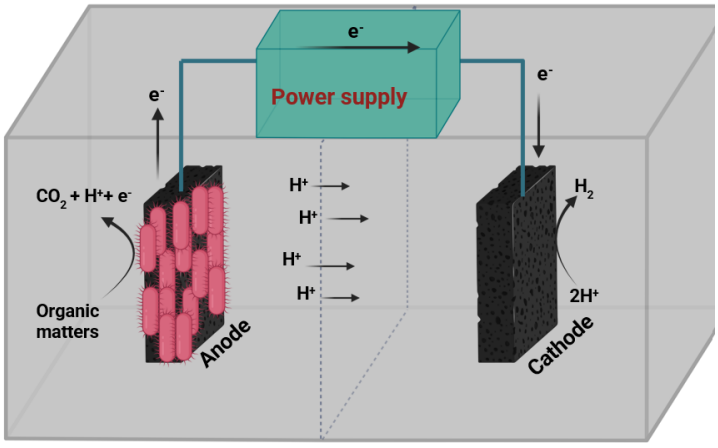

Figure 3. Schematic representation of a microbial electrolysis cell (MEC)

1.1.2. Basic principle of MEC

In MECs, electroactive microorganisms degrade organic substrates, releasing carbon dioxide (CO_2), protons, and electrons. The electrons are transferred to the anode and subsequently flow through an external circuit to the cathode, while the protons migrate through the solution. At the cathode, electrons and protons can combine to form hydrogen gas. Since this reaction is not thermodynamically favorable on its own, a small external voltage must be applied to drive the process under biologically assisted conditions.

In case acetate is used as a substrate in MEC, electrode reactions and their corresponding redox potential vs normal hydrogen electrode (NHE) are as follows:

Anode:

$$C_2H_4O_2 + 2H_2O \rightarrow 2CO_2 + 8e^- + 8H^+ \qquad (+0.279\ V) \qquad (1)$$

Cathode:

$$8H^+ + 8e^- \rightarrow 4H_2 \qquad (-0.414\ V) \qquad (2)$$

1.1.3. Thermodynamics of biohydrogen production

Due to thermodynamic limitations, many organic compounds, such as volatile fatty acids (VFAs) and solvents (e.g., butanol and ethanol), are not efficient substrates for fermentative hydrogen production. In MECs, this limitation is overcome by applying an external voltage through a power source, which supplies the additional energy required to drive hydrogen evolution. For the process to proceed, the applied voltage must exceed the equilibrium potential (Eeq) of the electrochemical cell (Sharma et al., 2024).

$$E_{eq}=E_{cat}-E_{an} \qquad (3)$$

Here, E_{eq} represents the equilibrium voltage of the electrochemical cell, while E_{cat} and E_{an} correspond to the cathodic and anodic half-cell potentials, respectively. To obtain these values, the Nernst equation must be applied to each half reaction under the given operating conditions. For instance, when acetate is used as the electron donor at the anode, its corresponding potential can be calculated according to Eq. 4.

$$E_{an} = E^{0}_{an} - \frac{RT}{8F} \ln \frac{[CH_3COO^-]}{[HCO_3^-]2[H^+]9} \quad (4)$$

Here, the standard anode potential (E^{0}_{an}) is 0.187 V. R is the gas constant (8.314 J/K), F is the Faraday constant (96,500 C/mol e^-), and T is the absolute temperature (K). Under normal biological conditions, the anode potential is about –0.279 V. In the same way, the expected cathode potential for hydrogen generation can be calculated (Eq. 5):

$$E_{cat} = E^{0}_{cat} - \frac{RT}{2F} \ln \frac{p_{H_2}}{[H^+]2} \quad (5)$$

p_{H_2} is the partial pressure of hydrogen, and the standard cathode potential (E^{0}_{cat}) is taken as 0 V. Under normal biological conditions, this potential is about –0.414 V. From equations 3–5, the equilibrium cell potential (E_{eq}) is about –0.14 V. This indicates that hydrogen production at the cathode requires an applied potential greater than +0.14 V. However, in practice, a higher voltage (generally between 0.2 and 1 V) is required due to electrode overpotentials and other system inefficiencies (Wang and Ren, 2013).

1.1.4. Microbial biocatalyst

Microorganisms act as essential biocatalysts in MECs, facilitating the conversion of organic substrates into biohydrogen. The choice of inoculum significantly affects system performance,

with approaches including the transfer of pre-enriched electrodes, the addition of effluents or biofilms from established systems, or the use of wastewater, anaerobic sludge, or pure bacterial isolates. Electrode biofilms can be formed from either pure or mixed cultures. Pure cultures allow methane-free gas production and offer greater control, while mixed cultures are generally more versatile, stable, and resilient under variable conditions, although substrate competition may occur (Kumar et al., 2017).

Within microbial communities, exoelectrogens are particularly important because they mediate electron transfer from organic substrates to the anode and, in some cases, also participate in cathodic reactions. These microorganisms, often referred to as anode-respiring bacteria (ARB) or electrochemically active bacteria (EAB), have been isolated from a wide range of environments, including wastewater, marine sediments, and anaerobic sludge (Kadier et al., 2016). A broad range of genera of these microorganisms has been characterized, such as α-Proteobacteria (e.g., *Rhodopseudomonas*, *Ochrobactrum*, and *Acidiphilium*), β-Proteobacteria (e.g., *Rhodoferax*), γ-Proteobacteria (e.g., *Citrobacter, Shewanella, Klebsiella*, *Enterobacter*, and *Aeromonas*), δ-Proteobacteria (e.g., *Geobacter*, *Geopsychrobacter*, and *Desulfobulbus*), Actinobacteria (e.g., *Propionibacterium*), Epsilonproteobacteria (e.g., *Arcobacter*), Firmicutes (e.g., *Clostridium* and *Thermincola*), and Acidobacteria (e.g., *Geothrix*) (Jiang et al., 2016).

Among known exoelectrogens, *S. oneidensis* and *G. sulfurreducens* stand out as key models for investigating microbe–electrode interactions. Their co-culture biofilm and electroactivity features are studied in this thesis. Co-cultivating *S. oneidensis* and *G. sulfurreducens* results in a cooperative interaction by combining the strengths of both species. *S. oneidensis* is metabolically flexible, able to use a wide range of substrates, and helps maintain anaerobic conditions by consuming oxygen, conditions that are essential for *G. sulfurreducens* (Knoll et al., 2023). While *S. oneidensis* produces a thin biofilm and transfers electrons mainly through

outer-membrane cytochromes and soluble redox shuttles, *G. sulfurreducens* utilizes conductive pili and multi-heme cytochromes for direct electron transfer, forming strong, conductive biofilms (Engel et al., 2019). In co-culture, *S. oneidensis* metabolizes lactate into acetate that supports the growth of *G. sulfurreducens*. In return, *S. oneidensis* benefits from the conductive biofilm produced by *G. sulfurreducens*, which facilitates its direct electron transfer to the anode (E. Klein et al., 2024). This mutual interaction leads to a more functional efficiency.

1.1.5. Extracellular electron transfer mechanisms in MEC

Exoelectrogenic bacteria transfer electrons to the anode through three principal mechanisms (Figure 4). The first is direct contact, where outer membrane cytochromes (OMCs), particularly multiheme c-type cytochromes, mediate electron transfer from the cell surface directly to the electrode (Figure 4a). These heme-containing proteins, located in the outer membrane, are integral components of the electron transport chain and act as key conduits for extracellular electron flow. This mechanism is well documented in exoelectrogens, where outer membrane cytochromes, including OmcZ, OmcS, and OmcE in *G. sulfurreducens* and MtrC and OmcA in *S. oneidensis*, play essential roles in mediating electron transfer to the electrode (Bond and Lovley, 2003; Yang et al., 2012). The second mechanism is nanowire-mediated transfer, which relies on electrically conductive pili, often termed bacterial nanowires, that enable long-range electron transport across biofilms (Figure 4b); *Geobacter* species are known to produce electrically conductive pili (Yang et al., 2012). The third mechanism involves soluble electron shuttles, which are small redox-active molecules that accept electrons during cellular respiration and diffuse to the electrode (Figure 4c). These shuttles may be secreted endogenously, such as flavins in *S. oneidensis* or phenazines in *Pseudomonas aeruginosa*, or they can be supplied exogenously as synthetic mediators, thereby expanding the range of bacteria capable of extracellular electron transfer (EET) (Rabaey et al., 2004).

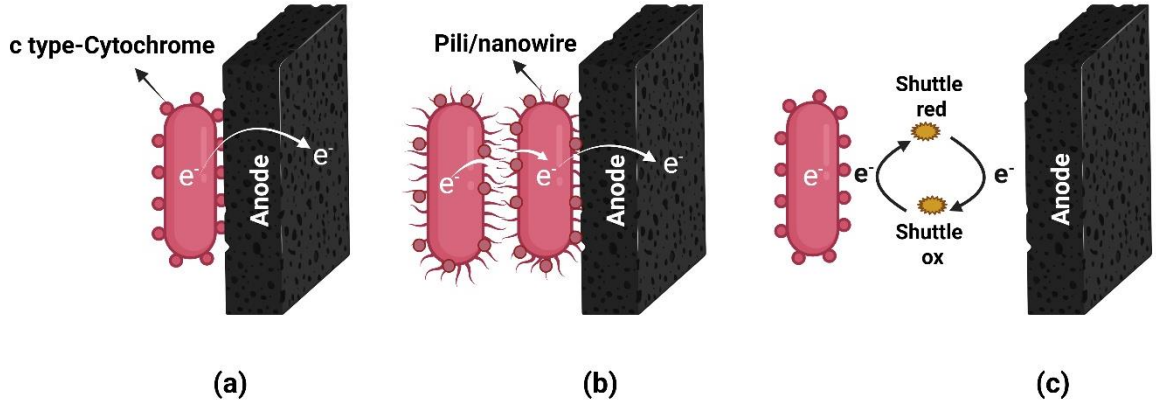

Figure 4. Schematic representation of the three principal mechanisms of extracellular electron transfer (EET) in exoelectrogenic bacteria: (a) direct electron transfer via outer membrane c-type cytochromes, (b) nanowire-mediated transfer through conductive pili, and (c) soluble electron shuttles that diffuse between the cell and the anode.

1.2. Parameters regulating the efficiency of MECs

The efficiency of MECs is governed by a combination of biological, physicochemical, and operational factors. Biological factors such as the type of microorganism, electron transfer mechanism, biofilm formation, and community structure influence MEC performance by determining the rate of organic matter degradation, the efficiency of electron transfer, and the stability of microbial activity (Cardeña et al., 2019; Gautam et al., 2023). Physicochemical factors such as substrate type, concentration, and conductivity, pH, and temperature control MEC performance by regulating microbial growth, metabolism rate, and electrochemical activity (Nam and Logan, 2012; Saravanan et al., 2023). Operational factors such as applied potential, electrode material and configuration, reactor design, and hydrodynamic conditions influence MEC performance. These factors control the microbial attachment, efficiency of mass transfer, and substrate distribution, as well as the driving force for hydrogen production (Spiess et al., 2021; Varanasi et al., 2018). In this thesis, the effects of hydrodynamic (flow

velocity), substrate concentration, pH, and applied potential were investigated, with particular attention to how each parameter influences microbial activity as well as the electrochemical performance and overall efficiency of MECs.

1.2.1. Hydrodynamic

1.2.1.1. Hydrodynamic effects on biofilm formation and stability

Biofilms are surface-associated microbial communities embedded within a self-produced extracellular polymeric substance (EPS) matrix, which provides structural protection and enables cooperative metabolic interactions (Valiei et al., 2024). The EPS matrix, composed of polysaccharides, proteins, nucleic acids, and lipids, forms a three-dimensional matrix that embeds and connects cells within the biofilm (Flemming et al., 2016). Biofilm formation begins with the attachment of planktonic cells to a surface, followed by cell proliferation and EPS production. After maturation, cells become irreversibly attached, although dispersal of individual cells can occur (Sauer et al., 2022). In biotechnological systems, biofilms enable high cell densities, efficient nutrient exchange, and enhanced resistance to environmental stress (Barceló et al., 2016). Among them, electroactive biofilms on anode or cathode are central to the operation of MECs. These biofilms establish conductive interfaces that link microbial communities to electrode surfaces, thereby enabling the transfer of metabolic electrons either through direct contact or via redox mediators (Rago et al., 2016). The formation of such biofilms is a complex, multi-step process influenced by diverse environmental and physiological factors. Among these, hydrodynamic forces, particularly shear stress, have emerged as a critical regulator of bacterial adhesion, biofilm growth, and structural organization (Godain et al., 2024; Liu et al., 2022).

Hydrodynamic conditions regulate biofilm development by modulating nutrient and oxygen transport, controlling bacterial attachment rates, and shaping the delivery of nutrients from the

bulk fluid to the biofilm matrix. These forces further influence key structural properties such as density, porosity, and mechanical stability, which in turn control the diffusion of nutrients and signaling molecules within the microbial community (Alotaibi, 2021). In BESs, hydrodynamic force is a key factor influencing the structure and performance of electroactive biofilms (Rago et al., 2016). Low shear stress can cause diffusion limitations resulting in a metabolically active outer layer surrounding an inactive, nutrient-depleted core, which limits electron transfer and reduces current output (Islam et al., 2019). In contrast, high shear stress may exceed adhesion and cohesion limits, resulting in the detachment of cells, extracellular polymeric substances (EPSs), or entire biofilm clusters, which reduce long-term stability (Wang et al., 2022a). Controlled shear force offers a balance and promotes faster biofilm development, increases cell density, and enhances metabolic activity. Additionally, it can alter the microbial community composition, helping to enrich exoelectrogenic species and improve overall electrochemical performance (Godain et al., 2024).

In this thesis, the influence of hydrodynamic forces through different flow velocities on the development and electrochemical functionality of biofilms formed by *G. sulfurreducens* and *S. oneidensis* co-culture was investigated.

1.2.1.2. Cyclic di-Guanosine Monophosphate signaling

Cyclic di-GMP (bis-(3′–5′)-cyclic di-guanosine monophosphate) is a key bacterial second messenger that coordinates motility, virulence, and biofilm development (Fang et al., 2025). Its intracellular concentration is maintained by the antagonistic activities of diguanylate cyclases (DGCs), which synthesize c-di-GMP from GTP, and phosphodiesterases (PDEs), which degrade it into pGpG or GMP. Two major PDE families are known: those containing EAL domains, which cleave c-di-GMP to pGpG, and those with HD-GYP domains, which hydrolyze it to GMP. As shown in Figure 5, elevated levels of c-di-GMP generally promote

the transition from planktonic to sessile states by stimulating EPS production and biofilm maturation, while reduced levels favor motility and dispersal (Elgamoudi et al., 2022). Previous studies demonstrated that, beyond chemical cues, physical forces such as hydrodynamic shear also influence c-di-GMP signaling (Fang et al., 2023). The genome of *S. oneidensis* MR-1 is predicted to encode numerous GGDEF- and EAL-domain proteins (50 and 31, respectively), including a substantial proportion of multidomain enzymes such as those containing both GGDEF and EAL domains (Chao et al., 2013). Although c-di-GMP is known to play a central role in biofilm development in this organism, the specific regulatory pathways through which these proteins act remain poorly understood. This thesis investigates how flow dynamics influence gene regulation and their effects on c-di-GMP signaling and biofilm formation in *S. oneidensis*, in addition to their effect on the bioelectrochemical performance and interactions of *G. sulfurreducens* and *S. oneidensis* co-culture.

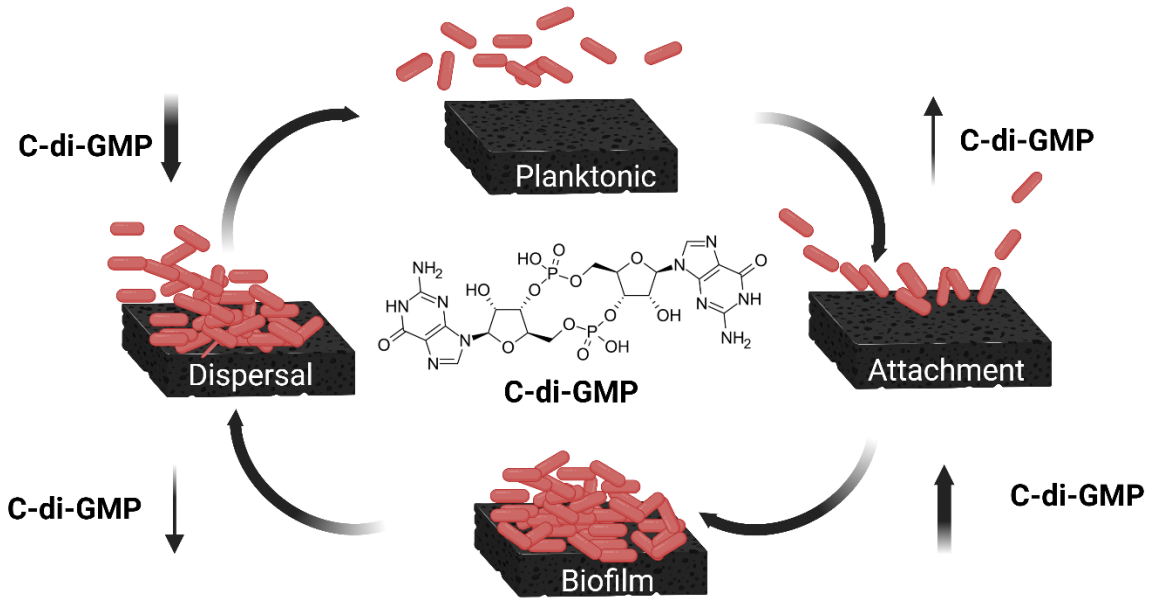

Figure 5. Schematic representation of the most common effects of c-di-GMP levels on biofilm dynamics.

1.2.2. Substrate

The type of substrate, ranging from simple compounds such as acetate to complex mixtures like hydrolysates, is a critical factor influencing MEC performance, as it directly affects biodegradability and shapes microbial community dynamics (Hua et al., 2019). Simple substrates are easily degraded, leading to higher coulombic efficiency (CE), faster start-up, and more stable operation. In contrast, complex industrial substrates often release intermediates that slow microbial activity and reduce system stability (Jadhav et al., 2019). Substrate concentration is another critical factor; at optimal levels, it supports microbial growth and improves hydrogen yield. However, excessive loading may cause substrate inhibition, accumulation of VFAs, and the proliferation of methanogens, which compete with exoelectrogens and divert electrons toward methane rather than hydrogen (Asrul et al., 2024; Elreedy et al., 2024).

While the potential of MECs for sustainable hydrogen production is well established, the majority of investigations have relied on synthetic substrates, which limits the direct applicability of their findings to practical scenarios. In contrast, real feedstocks such as hydrolysates derived from dark fermentation processes are rich in organic acids and readily available but introduce significant challenges. Their inherent variability in composition, frequent nutrient imbalances, and the presence of inhibitory compounds (e.g., ammonia, sulfides, and heavy metals) can adversely affect MEC stability and overall performance. Moreover, the response of microbial communities to such complex feedstock remains insufficiently understood, complicating efforts to optimize operational strategies and to predict performance at scale with reliability. These difficulties become even more pronounced during scale-up, where physical and operational heterogeneities often lead to reduced efficiency and greater instability. Indeed, numerous studies have reported marked declines in MEC performance when transitioning from laboratory-scale systems to larger reactors, particularly

when using real wastewater as the substrate (Baeza et al., 2017; Cusick et al., 2011; de Fouchécour et al., 2022; Escapa et al., 2015; Guerrero-Sodric et al., 2023). In this thesis, the influence of varying hydrolysate concentrations on MEC performance was systematically examined to address these gaps.

1.2.3. pH

At the microbial level, pH regulates enzymatic activity, metabolic pathways, and community stability, thereby influencing the degradation of organic matter and the transfer of electrons to the anode. Within biofilms, it shapes proton gradients that are essential for energy metabolism and efficient electron transport. At the cathode, local pH strongly affects the kinetics of the hydrogen evolution reaction (HER) by controlling proton availability (Kyazze et al., 2010). Neutral to slightly alkaline conditions (pH 7–8) have generally been reported to support optimal exoelectrogenic activity and hydrogen recovery (Nam and Logan, 2011; Sun et al., 2019). Typically, maximal enzyme activity and biofilm performance occur under near-neutral conditions, whereas exposure to highly acidic or alkaline environments results in diminished catalytic efficiency, reduced biofilm stability, and lower electrochemical output. These adverse effects are largely attributed to disruptions in the transmembrane electrochemical gradient, alterations in intracellular pH, ionic imbalance, and impaired proton transfer dynamics (Nawaz et al., 2020). Moreover, pH shapes microbial community composition by enhancing or suppressing specific functional groups, directing metabolic fluxes and fermentation product profiles, and thereby modulating the balance among exoelectrogens, fermenters, and methanogens. However, the optimum pH may shift depending on the buffering capacity of the substrate, nutrient composition, and the operational goal, whether focused on maximizing hydrogen yield, improving chemical oxygen demand (COD) removal, or sustaining microbial community resilience (Latif et al., 2017). Thus, maintaining appropriate pH through buffering

or controlled operation is essential to ensure stable MEC performance, maximize hydrogen production, and adapt the system to specific applications.

1.2.4. Applied potential

The anode potential is considered a critical operational parameter in MECs, as it directly governs electron transfer processes and microbial community dynamics. From a thermodynamic perspective, applying a more positive anode potential increases the driving force for electron transfer from microbial cells to the electrode, whether via direct contact through *c-type* cytochromes and conductive pili or indirectly through redox mediators (R. C. Wagner et al., 2010). Although higher anode potentials often enhance current density and reduce start-up times, no universal optimal potential exists (X. Wang et al., 2009). The best-performing range depends strongly on microbial strains, electrode materials, inoculum source, and reactor configuration. For instance, the potential required for the effective functionality of *Geobacter* species is relatively lower than that of *Shewanella* species. The difference arises mainly from the redox potentials of their outer-membrane cytochromes and preferred electron transfer routes, yet, in both cases, the underlying mechanisms by which anode potential influences electron transfer pathways and microcolony dynamics are similar (Li et al., 2025).

At the molecular level, increasing anode potential drives adaptive responses in electroactive microorganisms aimed at maximizing energy conservation and EET. These adaptations include elevated expression of EET-related proteins, upregulation of protein synthesis machinery, and enrichment of c-type cytochromes at the electrode interface, along with the potential emergence of alternative cytochrome configuration or novel electron transfer pathways (Howley et al., 2023). The applied potential also influences the electron affinity of terminal acceptors, modulates the transmembrane proton electrochemical gradient, and alters the kinetics of electron transfer among carriers. Collectively, these adjustments accelerate the EET rate,

enhance the NAD^+/NADH ratio, and improve the utilization of thermodynamic energy derived from substrate oxidation. In this way, electroactive microorganisms adjust their respiratory strategies to optimize metabolic efficiency under varying electrode potentials. However, excessively high potentials may destabilize cytochrome structures, disrupt EET-related gene regulation, and ultimately impair electron transfer capacity (Grobbler et al., 2018; Peng et al., 2010).

From a community perspective, anode potential serves as a selective pressure that enriches the proliferation of highly electroactive populations, which not only improve current generation but also shape the overall diversity index of the anodic biofilm (Commault et al., 2013; Korth and Harnisch, 2019; Zhao et al., 2020). In this way, the applied potential enhances electrochemical performance while at the same time restructuring the microbial community to favor organisms with efficient energy-harvesting strategies.

1.3. Methanogenic interference in H_2 production

In MECs, exoelectrogenic microorganisms rarely exist in isolation; instead, they are accompanied by a broad spectrum of microorganisms, including methanogenic archaea. These methanogens are frequently represented by hydrogenotrophic groups such as the *Methanobacteriales* and *Methanomicrobiales*, as well as *acetoclastic* taxa belonging to the *Methanosarcinaceae* and *Methanosaetaceae* within the order *Methanosarcinales* (Lu et al., 2012b). Their consistent occurrence across mixed inocula indicates that methanogens are highly adaptable to MEC conditions and are likely to play a substantial role in shaping reactor performance.

Methanogenic activity significantly hinders hydrogen production at the cathode, as both acetate and hydrogen can be diverted toward methane formation (Lu et al., 2012a). Acetoclastic

methanogens compete with exoelectrogens for acetate, thereby decreasing electron transfer efficiency to the anode and reducing biohydrogen production (Eq. 6). In addition, hydrogenotrophic methanogens directly consume cathodically generated H_2, which lowers hydrogen recovery at the cathode (Eq. 7) (Lu et al., 2011). For this reason, controlling methanogenic growth is essential to improve both substrate utilization and hydrogen recovery in MECs.

Co-production of CH_4 by methanogens

$$CH_3COOH \rightarrow CH_4 + CO_2 \quad (6)$$

$$4H_2 + CO_2 \rightarrow CH_4 + 2H_2O \quad (7)$$

The suppression of methanogenic activity is critical for enhancing hydrogen yields in MECs. A variety of strategies have been explored to mitigate these competing pathways, which can generally be classified into chemical inhibition and physicochemical regulation.

1.3.1. Chemical inhibition of methanogens

Numerous studies have shown that adding methanogenesis inhibitors can improve MEC performance. A common inhibition strategy targets the terminal enzyme methyl coenzyme M reductase (MCR), with compounds such as 2-bromoethanesulfonate (2-BES) and lumazine acting as cofactor analogs to block methane production, though their effectiveness depends on community and operating conditions. Other sulfonate derivatives and halogenated hydrocarbons inhibit corrinoid-dependent enzymes; chloroform, for example, suppresses methanogens over multiple cycles and sustains high hydrogen yields. Additional inhibitors such as alamethicin and certain antibiotics (e.g., neomycin sulfate) restrict methanogenic growth while promoting alternative pathways like acetogenesis, thereby improving CE (Karthikeyan et al., 2017).

1.3.2. Physicochemical inhibition of methanogens

Besides chemical inhibitors, adjusting operational conditions can also mitigate methanogenesis. For example, acidification can temporarily suppress methane formation, but it may also harm exoelectrogens and generally provides only short-term control (Hu et al., 2008). Similarly, lowering the temperature to 4–15 °C can suppress methanogenic activity more strongly than that of exoelectrogens. However, this strategy also reduces overall metabolic rates and hydrogen production, making it unsuitable for sustained MEC operation (Lu et al., 2011). Adjusting the applied voltage provides another control option. Wang et al. (2009) reported that at lower applied voltages (0.4 V), methane often dominates the biogas, whereas higher voltages (0.7 V) favor hydrogen production with methane levels reduced to below 4%. While increasing the voltage enhances hydrogen yield, it also raises energy consumption, creating a trade-off between efficiency and cost. Operating at higher voltages with shorter cycles can further suppress methane, though complete elimination is rarely achieved (Nam et al., 2011).

While physicochemical strategies can reduce methanogenesis to some extent, chemical inhibitors remain the most reliable option for long-term suppression because they directly target methanogenic pathways. Nonetheless, their effectiveness depends on dosage, the potential for microbial adaptation, and economic feasibility. An integrated approach is therefore essential for effective methanogenesis control in MECs, combining the specificity of chemical inhibition with the complementary benefits of operational adjustments, while also considering factors such as cost, long-term stability, and microbial adaptation (Karthikeyan et al., 2017). In this thesis, methanogenic suppression was investigated by regulating pH, applying positive anodic potentials, and optimizing substrate concentration balance.

1.4. MECs versus water electrolysis

MECs offer distinct advantages over conventional water electrolysis, particularly in terms of energy efficiency and safety. From an energy perspective, MECs are inherently more efficient because hydrogen production requires substantially lower electrical input, with part of the energy supplied through microbial oxidation of organic matter at the anode (Dange et al., 2021). Depending on the configuration, MECs have achieved energy yields up to 10–11 times higher than those of water electrolysis (Muddasar et al., 2022). In addition to these energy benefits, MECs present important safety advantages. Unlike conventional electrolysis, they do not generate oxygen, thereby eliminating the risk of hydrogen–oxygen mixing and crossover during pressurized hydrogen production (Patil et al., 2011). MECs also operate under neutral pH conditions, which support microbial activity while simplifying electrolyte handling and disposal compared with the highly alkaline electrolytes (e.g., KOH at pH 14) used in water electrolysis. Taken together, these features highlight MECs as a safer, more sustainable, and energy-efficient alternative for hydrogen generation.

1.5. Scale-up challenges and emerging solutions in MECs

MECs are increasingly recognized as a sustainable approach for hydrogen production and wastewater treatment; however, their transition from laboratory-scale to practical applications remains challenging.

Among these bottlenecks, high capital cost is particularly critical, as electrodes and current collectors account for more than 90% of total system expenses. Platinum-based cathodes, while exhibiting excellent catalytic activity, are unsuitable for large-scale applications due to their cost, environmental concerns, and susceptibility to poisoning. As a result, alternative materials such as stainless steel, nickel alloys, carbon nanomaterials, and biocathodes have been explored

to reduce costs while maintaining acceptable performance. On the anode side, graphite fiber brushes reinforced with metal cores provide enhanced mechanical stability, improved electrical conductivity, and a large surface area that supports high microbial colonization (Baudler et al., 2015; Dange et al., 2021).

Reactor design remains a significant challenge in scaling up MECs. Enlarged electrodes introduce higher internal resistance, mass transfer limitations, and uneven current distribution, all of which reduce hydrogen yields. Membrane-less configurations are cost-effective but subject to methane contamination, whereas membrane-based systems enhance gas separation but suffer from fouling and high costs. However, even with membrane integration, gas management remains problematic, as hydrogen purity is often reduced by mixing with CO_2 and CH_4. To overcome these limitations, advanced strategies such as hollow fiber membranes, gas diffusion electrodes, and in situ hydrogen recovery are being actively investigated (Fudge et al., 2021).

Long-term stability is a critical limitation in MECs, as systems often experience biofilm deterioration, cathode deactivation, fouling, and clogging. To address these issues, strategies such as resilient biofilm enrichment, methanogen suppression, optimized continuous-flow operation, and the use of pre-enriched inocula are being explored. At larger scales, additional complexity arises from multiple modules and wiring, increasing maintenance requirements. This challenge may be mitigated through simplified modular designs, advanced membranes, and optimized hydrodynamic conditions that improve mass transport and overall system efficiency (Pérez-rodríguez, 2025).

Beyond hydrogen, expanding MEC applications is essential for improving economic feasibility. MECs can be employed to produce value-added chemicals such as formic acid and acetate, recover nutrients, and remove pollutants. Coupling MECs with anaerobic digestion or conventional wastewater treatment plants is regarded as a practical approach, enabling them to

function as supporting units rather than stand-alone systems. Moreover, integration with renewable energy sources can lower operational costs and facilitate energy storage by converting surplus electricity into hydrogen or other useful products (Hua et al., 2019).

1.6. Acetoin production with MEC-derived hydrogen

Acetoin (3-hydroxy-2-butanone) is an important bio-based multi-purpose chemical with applications in the food, agriculture, cosmetics, biofuel, and pharmaceutical industries (Wang et al., 2013; Xiao and Lu, 2014). Although it is conventionally synthesized from fossil resources, microbial production offers a sustainable alternative. The biosynthetic pathway starts from pyruvate, which is converted by acetolactate synthase into α-acetolactate and subsequently decarboxylated by acetolactate decarboxylase to yield acetoin. Under different cellular conditions, acetoin can then be oxidized to diacetyl or reduced to 2,3-butanediol (Xiao and Xu, 2007). To enhance production efficiency, *Cupriavidus necator* has been engineered by deleting competing pathways (*acoABC* and *phaC1/phaC2*) and introducing acetoin biosynthesis genes from *Bacillus subtilis*, achieving nearly 100% yield under lithoautotrophic conditions using CO_2 as a carbon source and hydrogen as an electron donor (Härrer et al., 2021; Wang et al., 2013). Building on this concept, the present thesis demonstrates acetoin production through a similar system, in which hydrogen was supplied by MECs operated on hydrolysate, thereby establishing a sustainable route that couples renewable H_2 generation with microbial CO_2 conversion to acetoin.

1.7. Aim of this thesis

This thesis aims to optimize the performance of MECs for hydrogen production when treating wastewater containing organic matter and to clarify how key operational and physicochemical parameters influence the process efficiency. The abundant primary sludge hydrolysate was

considered for this purpose as a model wastewater for MECs. Hydrolysate, enriched in VFAs, provides high availability of electron donors, e.g., acetate, propionate, but also introduces inhibitory compounds and stimulates competing microbial pathways that can suppress hydrogen generation.

For this reason, a systematic investigation was therefore aimed here to examine how hydrodynamic conditions, substrate concentration, pH, and applied anodic potential shape current generation, biofilm development, and microbial community structure.

A specific objective was to determine how hydrodynamic conditions influence biofilm development, structure, and electroactivity through mechanosensing responses in *S. oneidensis* and *G. sulfurreducens* coculture.

Particular attention was given to assess the impact of such parameters to enrich electroactive bacteria while suppressing methanogens, which are competing H_2-consuming microorganisms.

In addition, experiments were extended from bench-scale MECs to larger bioreactor setups to address questions of scalability and to reflect practical operating scenarios better.

Alongside the experimental optimization, a techno-economic analysis was aimed at evaluating the potential of MECs to integrate wastewater treatment with renewable energy recovery.

Finally, the thesis also considered the coupling of MEC-derived hydrogen with microbial conversion pathways, using *C. necator*, to explore the broader potential of linking renewable hydrogen production with CO_2 fixation and sustainable chemical production.

2. Materials and Methods

2.1. Microbial methods

2.1.1. Microorganisms

The bacterial strains used in this study, along with their respective strain numbers, relevant genotypes, and corresponding references, are listed in Table 1.

Table 1. Strains with relevant genotype used in this study.

Strain no.	Relevant genotype	Reference
JG 407	*G. sulfurreducens* PCA	(Caccavo et al., 1994)
JG7	*S. oneidensis* MR-1	(Venkateswaran et al., 2008)
JG 2036	*S. oneidensis* MR-1 Δ*bpfD*	This thesis
JG 1884	Δ*acoABC*, Δ*phaC1*, Δ*phaC2*, *kan*^{R}, *mob*, *oriV*, *rep*, P_{ph}b–*alsSD–budC* (from *K. pneumoniae*).	(Weiler et al., 2024)

2.1.2. Chemicals and gases

All gases used in this study were provided by Westfalen AG (Münster). Chemicals were supplied from AppliChem (Darmstadt), Sarstedt AG & Co. (Nümbrecht), Merck (Darmstadt), Carl Roth (Karlsruhe), Thermo Fisher Scientific (Waltham, USA), and Sigma Aldrich (Steinheim).

2.1.3. Culture media and general preparations

Ultrapure water (PURELAB Plus, Veolia Water Technologies Germany, Celle) was used to prepare all media and buffers (see Table 2-10). The solutions were autoclaved for 20 minutes

at 121 °C and 1 bar overpressure, then stored at room temperature. Anoxic media were stored in bottles sealed with septa and purged for at least 30 minutes with repeated gassing cycles (N_2 or 80% N_2/20% CO_2) to ensure complete oxygen removal before autoclaving.

For autotrophic experiments, culture bottles were evacuated under vacuum for 20 minutes and subsequently filled with the cultivation gas mixture under atmospheric pressure.

Thermolabile substances (Tables 5 and 8) were sterilized by filtration (0.2 µm, Sarstedt AG & Co., Nümbrecht) and added to the autoclaved media.

For cultivation on solid media (Table 7), before pouring the agar plates, the medium was boiled and subsequently cooled to 60 °C. When required, thermo-sensitive components were added after cooling and before pouring the plates.

To ensure complete removal of electron acceptors from the preculture medium before BES reactor inoculation, the precultures were washed. *G. sulfurreducens* and *S. oneidensis* were centrifuged at 6000 rpm for 10 min (Sorvall RC-5C Plus, Thermo Fisher Scientific, Waltham, MA, USA). The supernatant was discarded, and the pellet was resuspended in 50 mL of washing buffer solution. The cells were centrifuged again under the same conditions, the supernatant discarded, and the pellet resuspended in 5 mL of washing buffer solution. The optical density of the suspensions (GENESYS™ 20, Thermo Fisher Scientific, Waltham, MA, USA) was then measured, and the required inoculation volume was determined.

Table 2. Composition of the NB trace element solution (100X).

Component	Amount
Nitriloacetic acid	2.140 g/l
$MnCl_2$ x 4 H_2O	0.100 g/l
$FeSO_4$ x 7 H_2O	0.300 g/l
$CoCl_2$ x 6 H_2O	0.170 g/l
$ZnSO_4$ x 7 H_2O	0.200 g/l
$CuCl_2$ x 2 H_2O	0.300 g/l
$AlK(SO_4)_2$ x 12 H_2O	0.005 g/l
Na_2MoO_4 x 2 H_2O	0.110 g/l
$NiSO_4$ x 6 H_2O	0.110 g/l
Na_2WO_4 x 2 H_2O	0.200 g/l
H_3BO_3	0.005 g/l
pH= 7	

Table 3. Composition of salt solution (10X).

Component	Amount
KH_2PO_4	4.20 g/l
K_2HPO_4	2.20 g/l
NH_4Cl	2.00 g/l
KCl	3.80 g/l
NaCl	3.60 g/l

Table 4. Composition of the selenite-tungstate solution (1000X).

Component	Amount
NaOH	500 mg/l
Na_2SeO_3	3 mg/l
Na_2WO_4 x 2 H_2O	4 mg/l

Table 5. Composition of vitamin solution (1000X).

Component	Amount
Biotin	2.0 mg/l
Folic acid	2.0 mg/l
Pyridoxine-HCl	10.0 mg/l
Thiamine-HCl	5.0 mg/l
Riboflavin	5.0 mg/l
DL-Ca-Pantothenate	5.0 mg/l
Nicotinic acid	0.1 mg/l
***p*-Aminobenzoic acid**	5.0 mg/l
Lipoic acid	5. 0 mg/l

Table 6. Composition of BES medium for the cultivation of *G. sulfurreducens.*

Component	Amount
KH_2PO_4	0.42 g/l
K_2HPO_4	0.22 g/l
NH_4Cl	0.20 g/l
KCl	0.38 g/l
NaCl	0.36 g/l
$NaHCO_3$	1.80 g/l
Na_2CO_3	0.50 g/l
$MgCl_2$ x 6 H_2O	0.21 g/l
Casamino acids	0.10 g/l
Vitamin solution (see Table 5)	1 .00 ml/l
Selenite tungstate solution	1.00 ml/l
NB trace element solution (see Table 2)	10.00 ml/l
Autoclave and then anaerobized with 80% N_2/20% CO_2. Complement with 10 ml vitamin solution (see Table 5), 1 ml 0.2 M Na-ascorbate solution, and 1 ml 0.4 M $CaCl_2$ x $2H_2O$ (filtered before). pH = 7.	

Table 7. LB media used for oxic cultivation of *S. oneidensis* cells. For the liquid medium, no agar was added.

Component	Amount
Tryptone	10 g/l
Yeast extract	5 g/l
NaCl	10 g/l
Agar (2 %)	20 g/l

Table 8. Complementary solutions were used in this study.

Component	Amount
Kanamycin	50 μg/ml
IPTG	0.8 mM
Diaminopimelic acid (DAP)	0.3 mM

Table 9. Media derived from the BES medium used for *G. sulfurreducens* cultivation (see Table 6)

Application	Microorganism	Na-DL-Lactate (60%)	Na-Acetate	Fumarate	HEPE
Washing buffer	*S.onedensis*	-	-	-	-
	G.sulfurreducens	-	-	-	-
	Co-culture	-	-	-	-
Pre-culture	*S.onedensis*	13.07 g/l	-	16.00 g/l	-
	G.sulfurreducens	-	1.24 g/l	6.40 g/l	1.00 g/l
BES medium	*S.onedensis*	3.73 g/l	-	-	-
	G.sulfurreducens	-	1.65 g/l	-	-
	Co-culture	3.73 g/l	-	-	-

Table 10. Composition of minimal medium number 81.

Component	Amount
Na_2HPO_4 x 2 H_2O	2.9 g/L
KH_2PO_4	2.3 g/L
NH_4Cl	1 g/L
$MgSO_4$ x 7 H_2O	0.5 g/L
$NaHCO_3$	0.5 g/L
Kanamycin	0.125 g/L
$CaCl_2$ x 2 H_2O	10 mg/L
$NaVO_3$ x H_2O	5 mg/L
$FeNH_4$ Citrate	2.5 mg/L
Thiamin-HCl x 2 H_2O	2.5 mg/L
Nicotinic acid	2.5 mg/L
Pyridoxin-HCl	2.5 mg/L
Ca-Pantothenate	2.5 mg/L
H_3BO_3	1.5 mg/L
$CoCl_2$ x 6 H_2O	1 mg/L
$ZnSO_4$ x 7 H_2O	0.5 mg/L
Riboflavin	0.5 mg/L
$MnCl_2$ x 4 H_2O	0.15 mg/L
Na_2MoO_4 x 2 H_2O	0.15 mg/L
$NiCl_2$ x 6 H_2O	0.1 mg/L
$CuCl_2$ x 2 H_2O	0.05 mg/L
Vitamin B_{12}	0.05 mg/L
Folic acid	0.01 mg/L

2.1.4. Cultivation of *S.oneidensis*

S. oneidensis cells were obtained from cryo culture (section 2.1.6), spread on LB agar plates (Table 7), and incubated under oxic conditions at 30 °C (Incubator I, Memmert, Schwabach, Germany). Single colonies from these plates were used to inoculate liquid LB medium (Table 7) and incubated overnight under oxic conditions at 30 °C with shaking at 180 rpm (New Brunswick Innova® 44, Eppendorf, Hamburg, Germany).

Growth of wild-type and mutant strains of *S. oneidensis* was monitored using an Infinite200Pro plate reader (Tecan Trading AG, Switzerland) over a period of 24 h, until cultures reached the plateau phase. Precultures were grown overnight in LB medium at 30 °C with shaking at 180 rpm. For measurements, 96-well plates were filled with 200 µl of the prepared medium per well, and inoculated to an initial OD_{600} of 0.1. During the experiment, OD_{600} was recorded every 30 min following an automated cycle consisting of 2 min shaking at 180 rpm and a 1 min rest phase before measurement.

2.1.5. Cultivation of *G. sulfurreducens*

To grow *G. sulfurreducens*, 2 ml of a cryo culture (section 2.1.7) was transferred into 1 L of anaerobic preculture medium (see Table 6). The culture was incubated at 30 °C for at least 2 days and then kept at room temperature for a maximum of 4 weeks before initiating a new culture. Two days before a BES experiment, 5% of the cell suspension from this culture was transferred into fresh cultivation medium to ensure harvesting during the exponential growth phase.

2.1.6. Cultivation of *C. necator*

For *C. necator*, cells were derived from cryo culture (section 2.1.7), spread on LB agar plates (Table 7), and incubated at 30 °C. Single colonies from these plates were used to inoculate an LB liquid preculture. Minimal medium no. 81 (Table 10) was then inoculated with the LB preculture to an initial OD_{600} of 0.05 and cultivated at 30 °C and 180 rpm for 72 h.

2.1.7. Conservation of strains

Long-term preservation of the bacterial strains used in this study was achieved by preparing cryo cultures. For this, 1 mL of cell suspension in the lag growth phase was mixed with 0.5 mL of sterile glycerol and immediately frozen in liquid N_2. The cryo cultures were stored at -80°C.

2.1.8. Hydrolysate characteristics

The hydrolysate utilized in this study was derived from a semi-technical pilot-scale system located at the Büsnau wastewater treatment plant in Stuttgart, Germany (equivalent population 10,000). It was produced via dark fermentation of primary sludge, as substrate, operated under controlled conditions, including hydraulic retention time (HRT) of 36 hrs, pH of 7, and temperature of 32 °C. Following fermentation, a two-step particle separation process was performed using a chamber filter press and subsequent microfiltration. Afterwards, the hydrolysate was centrifuged, step-filtered using a 0.45 µm filter, and stored at 4°C until use in experiments. The detailed characteristics of the hydrolysate are shown in Table 11.

Table 11. Characteristics of the hydrolysate used in this study.

Component	Amount
Total organic carbon (TOC)	350 mM
Total inorganic carbon (TIC)	11 mM
Total nitrogen (TNb)	37.3 mM
Total Phosphorus (TP)	269 mg/L
Acetate	34.28 mM
Propionate	25.67 mM
Butyrate	3.4 mM
Lactate	ND
NH_4^+-N	154 mg/L
NO_3^-	2.58 mg/L
Ca^{2+}	421 mg/L
Fe^{2+}	1.1 mg/L
K^+	60.84 mg/L
Mg^{2+}	51.77 mg/L
Mn^{2+}	0.92 mg/L
Na^+	114 mg/L
S	25.1 mg/L
Si^{4+}	11.2 mg/L
Zn^{2+}	3.01 mg/L
Cl^-	164 mg/L
SO_4^{2-}	20.85 mg/L
Ionic conductivity	8.75 mS/cm
pH	4.2

ND, not detected

2.2. Molecular biology methods

2.2.1. Metagenomic analysis

To examine microbial community composition, whole genome sequencing was performed using Nanopore sequencing (Oxford Nanopore Technologies, Oxford, UK); it was carried out using a MinION Mk1b device fitted with a R10.4.1 flow cell and run with MinKNOW software

version 22.10.7. DNA was extracted using the DNeasy PowerBiofilm Kit (Qiagen, Hilden, Germany). The concentration and purity of the extracted DNA were assessed using a NanoDrop 2000 spectrophotometer and a Qubit dsDNA assay Kit (Thermo Scientific, Waltham, MA, USA). DNA samples were stored at −20°C until the MinION sequencing. Basecalling and demultiplexing were performed with dorado version 7.3.9 in super accuracy mode. Sequencing reads were aligned against metagenome-assembled genomes (MAGs) from the MiDAS database with BLAST v2.12 for taxonomic identification and abundance estimation. In order to enable subsequent analysis, metagenomic bins were prepared. Accordingly, a sample-based read assembly was performed with Flye v2.9.1.-b1768, including the parameters -nano-hq and -meta. Read mapping was then performed using Minimap2 v2.24. By Metabuli v1.9.0.2 and the GTDB database r214, contigs were annotated. Contig coverage was evaluated with Minimap2 as well as Samtools 1.13. Binning was conducted with Taxvamb v4.1.4.

2.2.2. Transcriptomic analysis

RNA was isolated from anodic biofilm cocultures of *S. oneidensis* and *G. sulfurreducens* using the RNeasy PowerBiofilm kit (Qiagen, Hilden, Germany) according to the manufacturer's instructions. Library prep and Illumina sequencing were conducted by Eurofins Genomics (Ebersberg, Germany). A strand-specific library of cDNA was prepared and sequenced with a target of 50 million read pairs (2 ×150 bp) per sample. A biological triplicate was prepared for each experimental condition. Sequencing of two samples failed to achieve adequate sequencing and/or mapping quality and were therefore excluded from subsequent analysis.

2.2.3. Stop-codon integration

Stop codon integration was carried out using a CRISPR/dCas9 as previously described by Fritz et al. (2025) to generate targeted gene disruptions. All primers and oligonucleotides (forward and reverse) used are listed in the Appendix, Tables S2–S3.

2.3. Analytical methods and calculations

2.3.1. Spectrophotometry

Optical density at 600 nm was measured using a GENESYS™ 20 photometer (Thermo Fisher Scientific, Waltham, MA, USA). Samples were measured undiluted up to an OD_{600} of 0.4; samples above this value were diluted accordingly. Deionized water (DI water) served as the reference blank. In addition, the turbidity of the cultivation medium was measured and compared with DI water as a reference.

2.3.2. High-performance liquid chromatography (HPLC)

Organic acids were quantified using HPLC. An UltiMate 3000 SD HPLC system (Thermo Fisher Scientific, Waltham, USA) equipped with a RefractoMax520 refractive index detector (ERC, Riemerling, Germany) was employed. Before analysis, 150 µL of each sample was filtered through a 0.2 µm polyethylene tetrafluoroethylene (PTFE) filter (VWR, Darmstadt, Germany) and mixed with 50 µL of 0.5 mM sulfuric acid in a 96-well microtiter plate. Separation was carried out using an Aminex HPX-87H column (BioRad, Munich, Germany) at 60 °C. The mobile phase consisted of 5 mM sulfuric acid with a flow rate of 0.6 mL/min. Retention times, determined by the interaction of each analyte with both stationary and mobile phases, were compared with external standards to identify and quantify chemicals (Acetate, lactate, propionate, butyrate, and acetoin).

2.3.3. Gas chromatography

Gas chromatography was applied to determine the concentrations of H_2, O_2, N_2, CH_4, and CO_2. Measurements were carried out using a 490 Micro-GC (Agilent Technologies, Waldbronn, Germany) and evaluated with Agilent OpenLAB CDS (EZChrom Edition) software. The system was equipped with two columns. The first was an MS5A column (10 m length), operated with argon as carrier gas at 70 °C and 150 kPa. The second was a PPQ column (10 m length), operated with helium as carrier gas at 45 °C and 150 kPa. Detection was performed using a thermal conductivity detector (TCD; Agilent Technologies, Waldbronn, Germany). The method included a stabilization time of 5 s, a sampling time of 20 s, an injection time of 50 ms, and a transfer line temperature of 110 °C.

2.3.4. Total organic carbon (TOC) analysis

The TOC content in the samples was measured using a DIMATOC® 2100 analyzer (DIMATEC Analysentechnik GmbH, Germany). This instrument quantifies TOC by catalytic combustion at high temperature, where all carbon compounds are oxidized to CO_2. The released CO_2 is then detected by a non-dispersive infrared (NDIR) sensor, and TOC is calculated automatically as the difference between total carbon (TC) and inorganic carbon (IC).

2.3.5. Ion chromatography (IC)

The anions (NO_3^-, SO_4^{2-}, and Cl^-) were quantified by IC with a 790 Personal system (Metrohm, Switzerland). All other inorganic elements were determined using inductively coupled plasma–optical emission spectroscopy (ICP-OES, 5110; Agilent, USA).

2.3.6. Optical coherence tomography (OCT)

The development of biofilms on electrode surfaces was quantified non-invasively using optical coherence tomography (OCT) with a Ganymede II–LSM04 system equipped with an LSM03-BB objective lens (Gan210-SP4, Thorlabs, Dachau, Germany). An infrared light source (930 nm, 100 nm bandwidth) generated a beam that was split into reference and measurement paths. After interacting with the sample, the measurement beam was recombined with the reference beam in an interferometer, and the resulting interference signal was detected spectroscopically to obtain structural information. This enabled three-dimensional reconstructions from cross-sectional images along the X-, Y-, and Z-axes (Klein et al., 2022; M. Wagner et al., 2010). Images were acquired at 100 kHz with voxel dimensions of 4 × 4 × 2.14 µm (x/y/z) using ThorImage 5.1.1, and subsequently processed in Fiji (ImageJ 1.53/2.1.0; Schindelin et al., 2012). Raw OCT images with 32-bit depth were converted to 8-bit images (0–255 gray levels) for processing. Biomass was distinguished from background noise by applying an intensity threshold and binarizing the images, yielding two classes (white = biofilm, black = background), which served as the basis for all further analyses.

2.3.7. Statistical analysis

Biofilm porosity was calculated by comparing the actual measured height to the theoretical height expected under the assumption of full density (normalized biovolume) (Eq. 8).

$$\text{Porosity } (\%) = \frac{h_{\text{real}} - h_{\text{theoretical}}}{h_{\text{real}}} \times 100 \quad (8)$$

Shear stress within the microfluidic channel was calculated based on the wall shear rate and the dynamic viscosity of the electrolyte. For a rectangular laminar flow channel, the wall shear rate ($\gamma^{\cdot}$) was estimated using Eq. 9:

$$\gamma^{\cdot} = \frac{6Q}{wh^2} \tag{9}$$

where Q is the volumetric flow rate (m^3/ s), w is the channel width (m), and h is the channel height (m). The corresponding wall shear stress (τ) was then determined as Eq. 10, where μ is the dynamic viscosity of the fluid (Pa·s).

$$\tau = \mu\, \gamma^{\cdot} \tag{10}$$

Current data were normalized to the projected surface area of the working electrode, which was 0.3 cm^2 in the microfluidic bioelectrochemical flow cell, 36 cm^2 in the cylindrical MEC (Cylindrical-MEC), and 0.5 m^2 in the rotating disk bioelectrochemical reactor (RDBER). Accordingly, the current density (I) was calculated by dividing the measured current i (A) by the projected surface area (A) of the working electrode (Eq. 11).

$$I = \frac{i}{A} \tag{11}$$

The mean current density ($\bar{I}$) over the entire experimental period was calculated by dividing the integrated current density (I) by the experimental time (t) (Eq. 12).

$$\bar{I} = \frac{\int_0^t I\,dt}{t} \tag{12}$$

CE was calculated as shown in Eq. 13, where I (A) is the current generated over time t (s), F is Faraday's constant (96,485 C/mol), b is the number of theoretical moles of electrons released per mole of oxidized compound (4 for TOC and 8 for acetate), and $\Delta(M)$ (moles) represents the electron donor consumption during this period.

$$CE\ (\%) = \frac{\int_0^t I\,\mathrm{d}t}{F\,b\,\Delta(M)} \tag{13}$$

Hydrogen energy efficiency (η_{H_2}) was determined by quantifying the energy content of hydrogen produced relative to the electrical energy input, using Eq. 14; n_{H_2} represents the moles of hydrogen generated, and ΔH_{H_2} is the calorific value difference of hydrogen in comparison to electrical energy of 285.83 kJ/mol. The electrical energy input (E_{input}, in kJ) was computed by integrating the product of voltage (V) and current (A) measured over the experimental period.

$$\eta_{H_2} = \frac{n_{H_2}\,\Delta H_{H_2}}{E_{\text{input}}} \tag{14}$$

Cathodic hydrogen recovery efficiency ($\eta_{\text{cat, H}_2}$) was calculated to evaluate the efficiency of hydrogen production at the cathode relative to the electrical current supplied. It was determined by dividing the experimentally measured moles of hydrogen ($n_{H_2,\text{measured}}$) by the theoretical moles of hydrogen ($n_{H_2,\text{theoretical}}$), calculated using Faraday's law based on the total charge transferred. The calculation is presented in Eq. 15, and theoretical hydrogen production is defined in Eq. 16.

$$\eta_{\text{cat},H_2} = \frac{n_{H_2,\text{measured}}}{n_{H_2,\text{theoretical}}} \quad (15)$$

Theoretical

$$H_2 \text{ production} = \frac{I \int dt}{2F} \quad (16)$$

To assess energy efficiency, hydrogen yield per unit of energy input (kg H_2/kWh) was calculated (Eq. 17), m_{H_2} is the mass of hydrogen produced (kg/day m²), and E_{input} is the electrical energy input (kWh/day m²).

$$Y_{H_2/E} = \frac{m_{H_2}}{E_{\text{input}}} \times 100 \quad (17)$$

The H_2 production cost (€/kg H_2) quantifies the energy-related expense associated with producing one kilogram of hydrogen, calculated using the system electrical energy input and the unit electricity price, as shown in Eq. 18, using current electricity price of 0.18 €/kWh (Eurostat, 2025); E_{input} is electrical energy input (kWh), C_{elec} is unit cost of electricity (€/kWh) and m_{H_2} is the theoretical mass of hydrogen produced (kg). The net economic yield of hydrogen (€/kg H_2) represents the financial return per kilogram of hydrogen generated. It is calculated as the difference between the average market selling price of hydrogen (10 €/kg) and its production cost (Mission Innovation Hydrogen Valley Platform, 2025). In this study, only the cost of electrical energy input was taken into account (Eq. 19).

$$H_2 \text{ production cost} = \frac{E_{\text{input}} \times C_{\text{elec}}}{m_{H_2}} \quad (18)$$

$$H_2 \text{ net economic yield} = H_2 \text{ market price} - H_2 \text{ production cost} \quad (19)$$

To quantify the efficiency of gas utilization in acetoin production, two metrics were calculated: yield on H_2 and carbon capture efficiency. The yield on H_2 was defined as the molar ratio of produced acetoin (n_{acetoin}) to the amount of supplied H_2 (n_{H_2}) at 25 °C, 1 atm (Eq. 20)

$$Y_{\text{acetoin/H}_2} = \frac{n_{\text{acetoin}}}{n_{\text{H}_2}} \quad (20)$$

Carbon capture efficiency was determined as the fraction of carbon atoms incorporated into acetoin relative to the carbon supplied as CO_2, taking into account the four carbon atoms per acetoin molecule (Eq. 21):

$$\eta_{C_{\text{acetoin}}} = \frac{4\, n_{\text{acetoin}}}{n_{\text{CO}_2}} \quad (21)$$

Here, $\eta_{C_{acetoin}}$ corresponds to the molar amount of acetoin produced, while n_{H_2} and n_{CO_2} represent the molar amounts of H_2 and CO_2 supplied, respectively.

2.3.8. Principal component and network analyses

Principal Component Analysis (PCA) was performed as a multivariate statistical tool to evaluate the combined effects of different parameters on performance indicators using Minitab 22.3. In addition, co-occurrence network analysis based on Spearman's rank correlations was carried out to identify global interrelations among genera under the experimental conditions.

Only significant correlations ($p < 0.1$) were included in the network, which was constructed and visualized using R (version 4.1.0) and Gephi (version 0.10).

2.4. Electrochemical methods

Chronoamperometry was employed to evaluate the electrochemical activity of the biofilms based on current generation. The working electrode potential was controlled at –0.199 V vs Ag/AgCl (unless otherwise specified), equivalent to 0 V vs the standard hydrogen electrode (SHE). The resulting current was recorded at 60 s intervals. Potentiostats, including Interface 1000B, 1000E, 1010E, and 5010E (Gamry, Philadelphia, PA, USA), as well as a SensorStat system (Uniscan Instruments Ltd., UK), were used to apply and maintain the defined electrode potentials.

2.5. Bioelectrochemical setups

2.5.1. Microfluidic BES flow cell

The microfluidic BES consisted of a straight culture channel 61.75 mm in length with a total volume of 354 µL. Reactors were fabricated from Sylgard® 184 silicone elastomer (Michigan, USA) by casting polydimethylsiloxane (PDMS) into a brass mold, followed by polymerization for 2 h at 60 °C. During molding, placeholder cannulas were inserted to create access ports for medium supply, removal, and inoculation. After curing, the channel was sealed with a 1-mm glass microscope slide, which was covalently bonded to the PDMS using oxygen plasma treatment (Plasma Flecto 10, Plasma Technology, Herrenberg). The assembled reactor was then incubated for 10–20 minutes at 100 °C to reinforce the bond. Blunt cannulas were inserted into the prepared ports, with diameters of 0.95 mm for medium supply and removal and 0.57 mm for inoculation and chamber access, and connections were established via Luer fittings.

The Custom Ag/AgCl reference electrodes were produced electrochemically. A 3 cm long silver wire (0.8 mm diameter; ChemPur, Karlsruhe) was cleaned, dried, and placed inside a fine platinum mesh. The assembly was immersed in 0.1 M degassed hydrochloric acid, while the beaker surface was flushed with nitrogen. The silver wire functioned as the working electrode, the platinum mesh as the counter electrode, and a commercial Ag/AgCl electrode as the reference. The system was equilibrated at open-circuit voltage (5 min) and then polarized at +50 mV vs OCV for 50 min. The prepared electrodes were dried after fabrication.

Graphite–polypropylene composite electrodes (PPG 86, Eisenhuth GmbH & Co. KG, Germany; 3 × 10 mm surface area and an electrical conductivity of 60.15 S/ cm^2) were embedded within the culture channel.

The complete system consisted of two reactors connected in series, each comprising three microchannels to allow triplicate measurements. The upstream reactor contained the working electrode and the custom-made Ag/AgCl reference electrode, while the cathodic compartment was exposed to air and remained oxic. In contrast, anoxic conditions in the anodic compartment were maintained by continuous flushing with 80% N_2 / 20% CO_2. The working electrode potential was controlled with a SensorStat potentiostat (Uniscan Instruments Ltd, UK), connected through 0.1-mm silver foil (Chempur, Germany), and set to 0 V vs SHE. Before microbial inoculation, electrodes were sterilized with 70% ethanol and conditioned by circulating medium through the system.

Media were supplied to the reactors through silicone tubing with an inner diameter of 1.5 mm (Carl Roth, Karlsruhe, Germany). A constant flow rate was maintained using Reglo ICC peristaltic pumps (ISMATEC Industry Solutions GmbH, Grevenbroich, Germany), and reactor effluents were collected in waste bottles. For inoculation, a mixed culture of *G. sulfurreducens* and *S. oneidensis* (OD_{600} = 4; ratio 1:10) was introduced using fluoro rubber tubing (Cole-

Parmer, Vernon Hills, IL, USA) using an L160 syringe pump over a period of 2 h (Landgraf Laborsysteme HLL GmbH, Langenhagen, Germany). A schematic of microfluidic BES designs and compartments is shown in Figure 6.

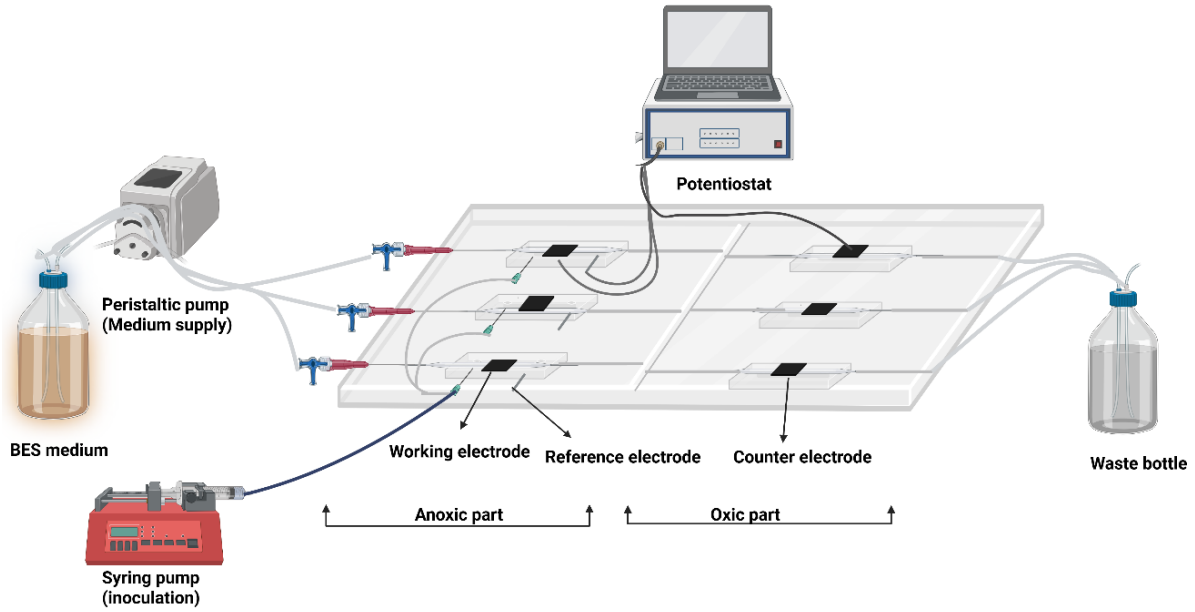

Figure 6. Schematic representation of the microfluidic bioelectrochemical system.

2.5.2. Cylindrical-MEC

The current generation of microorganisms was investigated in batch mode using a Cylindrical-MEC. The working electrode consisted of graphite felt (6 × 3 cm, GFD 2.5, SGL Group, Germany) with a projected surface area of 36 cm². Before use, the electrode was rinsed sequentially with isopropanol and deionized water. The counter electrode was a platinum mesh (99.9%, 10.24 meshes/mm², ChemPur, Karlsruhe, Germany) with an active surface area of 1.25 cm², connected via a platinum wire (Ø 0.1 mm, 99.9%; ChemPur, Karlsruhe, Germany). An Ag/AgCl reference electrode was used to set the anodic potential. The reactor had a working volume of 250 mL and was sealed with four M5 screws. Before the experiment, it was filled with DI water and autoclaved.

Anoxic conditions were maintained by continuously purging the reactor headspace with a gas mixture of 80% N_2 and 20% CO_2. A magnetic stirrer with a stirring rod (Topolino, IKA-Werke, Staufen, Germany) ensured constant mixing of the medium. A schematic representation of the Cylindrical-MEC is shown in Figure 7.

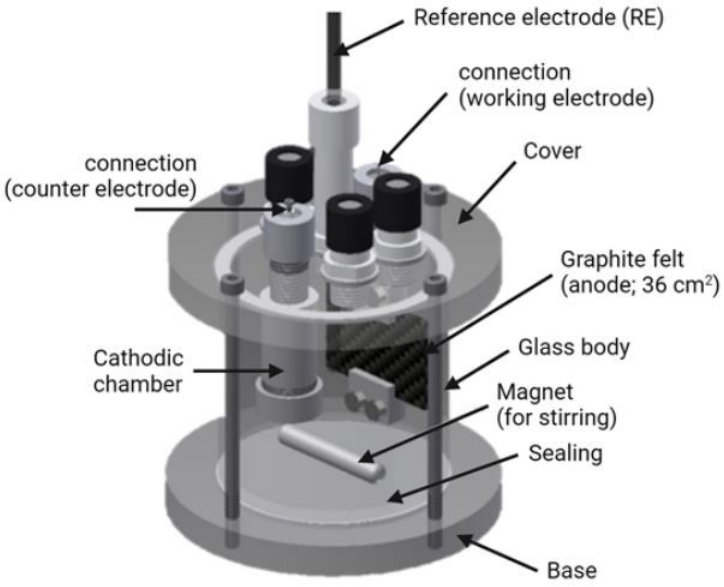

Figure 7. Schematic of the cylindrical microbial electrolysis cell (Cylindrical-MEC) (according to Härrer et al., 2022)

The wild-type *G. sulfurreducens* PCA strain was used as the inoculum to establish a stable, electroactive biofilm. The BES medium, supplemented with 15 mM acetate, was inoculated with *G. sulfurreducens* at a final OD_{600} of 0.1. After biofilm enrichment, the medium was replaced with hydrolysate. Figure 8 shows the experimental setup, which included biofilm enrichment with *G. sulfurreducens* followed by testing under varying hydrolysate concentrations (20%, 40%, 60%), pH values (5–8), and applied anodic potentials (−0.2 to +0.4 V).

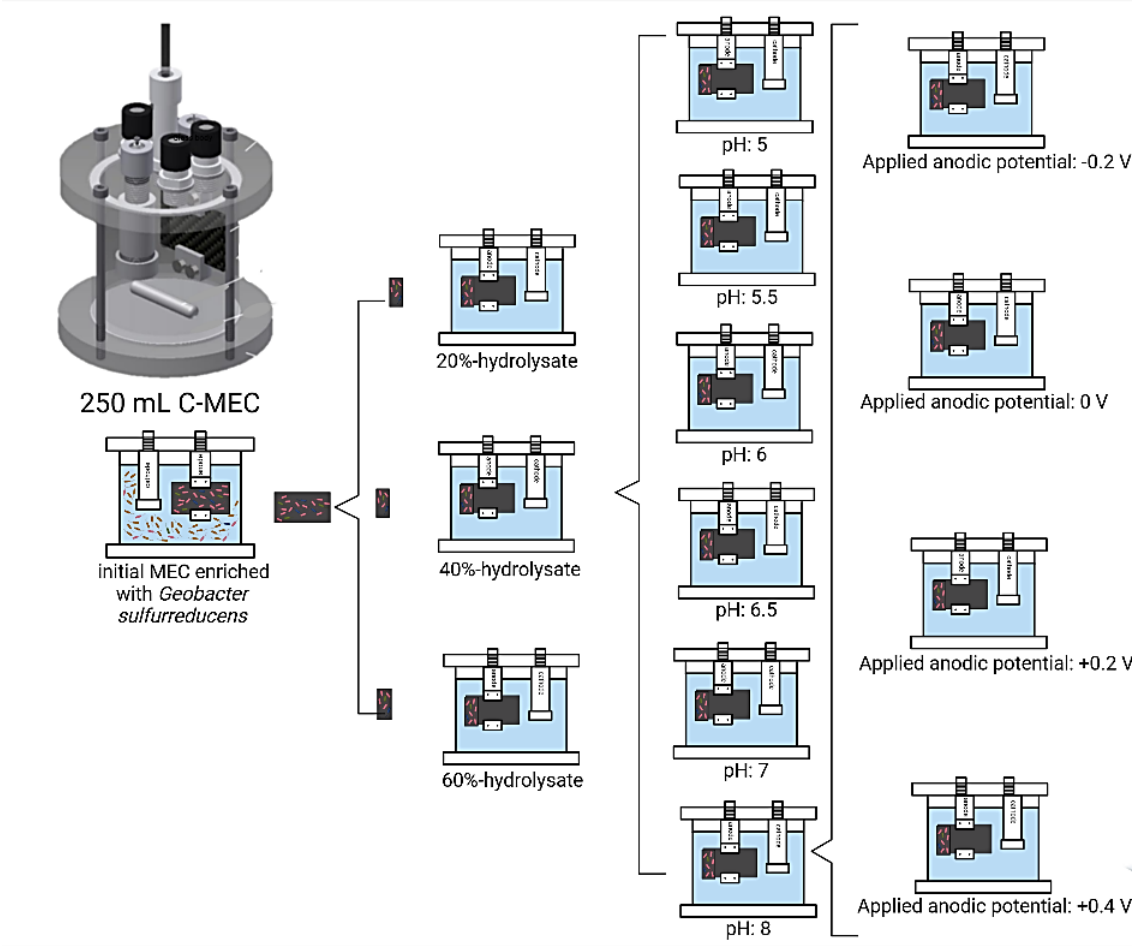

Figure 8. Schematic of the cylindrical microbial electrolysis cell (Cylindrical-MEC) setup and experimental design. The system was filled with unsterile hydrolysate and enriched with *Geobacter sulfurreducens* over 10 days. Subsequently, the carbon felt anode was distributed to fresh MECs operated under varying hydrolysate concentrations (20%, 40%, and 60%), pH values (5–8), and applied anodic potentials (−0.2 to +0.4 V vs. standard hydrogen electrode [SHE]).

2.5.3. Rotating disk bioelectrochemical reactor (RDBER)

The RDBER, used in this study, had a total volume of 12.6 L, comprising the reactor chamber and its peripheral system, and is shown in Figure 9. The RDBER design was formerly developed by Hackbarth et al. (2023) and Knoll et al. (2023). The peripheral setup consisted of stainless-steel tubing (10 mm diameter) and a peristaltic pump system (Masterflex™ L/S™ analog console pump with Easy-Load II pump heads, Fisher Scientific, Schwerte, Germany) equipped with gas-tight tubing (Masterflex™ L/S™ Viton™, FDA-compliant, Fisher

Scientific, Schwerte, Germany). The pH was automatically regulated in a mixing vessel using a Biostat® A fermenter control system (Sartorius AG, Göttingen, Germany) with an integrated pH probe. Both the mixing vessel and the rotating disk reactor chamber were maintained at 30 °C using silicone heating mats (LCS Isotherm GmbH & Co. KG, Frankfurt, Germany).

The working electrode consisted of seven graphite plates with a total projected surface area of 0.5 m², while the counter electrode comprised eight titanium-coated half-disks with a combined surface area of 0.25 m². Electrode rotation was controlled by a bipolar NEMA-11 stepper motor with a 100:1 gear ratio (Phidget, Calgary, Canada) and set to 1 rpm. Before the operation, the reactor system and all peripheral components were autoclaved and subsequently assembled under sterile conditions.

The process started with BES medium for *G. sulfurreducens* enrichment (final OD_{600} = 0.1) and was subsequently continued using unsterile 40% hydrolysate.

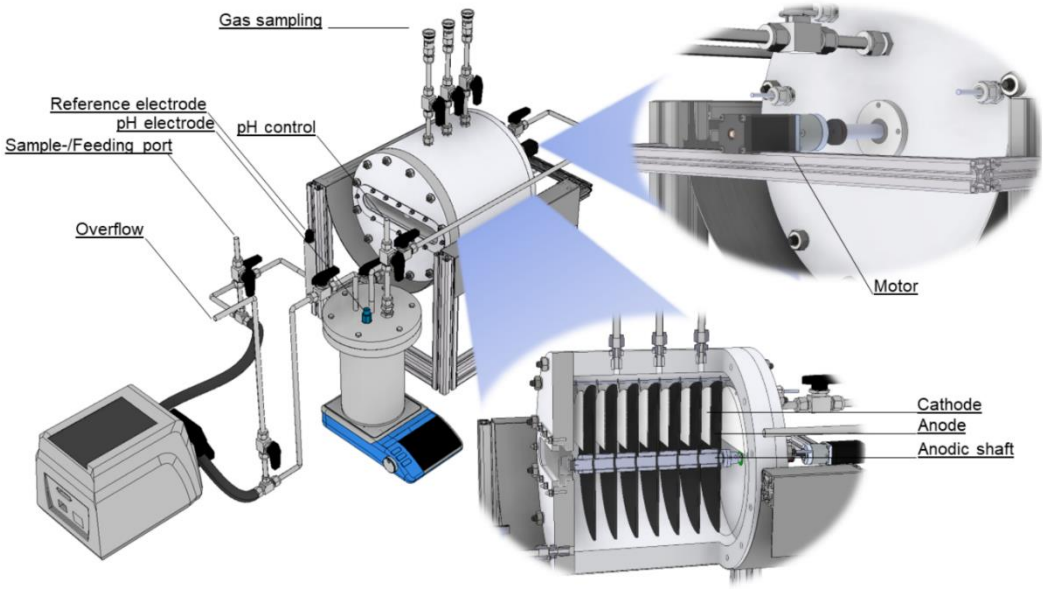

Figure 9. Schematic representation of the rotating disk bioelectrochemical reactor (RDBER) (according to Knoll et al., 2023).

2.6. Mathematical evaluations and graphs

2.6.1. Mathematical evaluations

Mathematical evaluations were performed using Origin 2023 (OriginLab, Massachusetts, USA).

2.6.2. Production of graphs

Origin 2023 (OriginLab, Massachusetts, USA) was used for graphical representations.

The illustrative figures were created using BioRender (https://www.biorender.com).

3. Results

Optimizing key operating parameters is essential for improving the performance and advancing the practical application of MECs. Even minor changes in system conditions can have a significant impact on efficiency, stability, and product yield. This chapter presents experimental results that investigate how different operating strategies influence MEC performance across multiple configurations and scales.

In the initial part of this thesis, the impact of hydrodynamic conditions, specifically flow velocity, on biofilm formation and electrochemical activity of *S. oneidensis–G. sulfurreducens* co-cultures was investigated in a microfluidic BES. The microfluidic system allowed precise control of flow velocity to directly study the effects of shear stress on biofilm morphology and current generation. Biofilm development was monitored every 24 hours using OCT to measure biovolume and porosity. A controlled shift in flow velocity was introduced to examine how dynamic shear stress affects biofilm structure and function. Transcriptomic analysis identified flow-responsive gene regulation, revealing molecular mechanisms underlying the biofilm response to shear stress. Based on these results, one *S. oneidensis* mutant strains were constructed by inactivating gene that showed significant differential expression under varying flow conditions. Its biofilm and electrochemical performance were compared to the wild type to determine gene-specific functional roles.

In the second part, the effect of substrate concentration, pH, and applied anodic potential on current density, substrate removal, CE, and microbial community composition was investigated in Cylindrical-MEC. These parameters were key to identifying conditions that improved electrochemical performance and enhanced biohydrogen yields.

Subsequently, to assess scalability, the optimized conditions from the Cylindrical-MECs were applied to a 10 L RDBER. Current density, substrate consumption, gas composition, and hydrogen production were continuously monitored. The effect of pH on suppressing methanogenic activity was examined, followed by an investigation of the impact of applied anodic potential on gas composition and overall electrochemical performance. Further, energy efficiency and techno-economic analyses were conducted to evaluate the feasibility of scaling up the process.

Finally, the hydrogen produced under these optimized conditions was used for acetoin synthesis, demonstrating the potential for integrating MECs into downstream value-added bioprocesses.

3.1. Effect of surface flow dynamics

3.1.1. Flow velocity effects on biofilm morphology–performance balance

A coculture of *G. sulfurreducens* and *S. oneidensis* was grown in microfluidic BES flow cells to investigate the influence of flow velocity on biofilm characteristics and current density. Biofilms were grown under two defined flow velocities (i.e., 0.2 and 0.8 mm/s), and their performance was compared based on current density, biovolume, and porosity. This approach enabled direct assessment of flow-dependent changes in biofilm morphology and electroactivity.

It was hypothesized that higher flow velocities would impose increased shear forces that could potentially compress biofilm structures. Such compression may increase the density of conductive extracellular structures, thereby enhancing current production. The effect of flow velocity was evaluated over time, and both the time-course data and corresponding mean values

are shown in Figure 10. Data was acquired until the point where the current reached a steady state.

Our experimental results initially appeared to support our hypothesis. As shown in Figures 10a-b, biofilms grown at a flow velocity of 0.8 mm/s initiated current production earlier and achieved a higher mean current density (86.3 $\mu A/cm^2$) compared to those grown at 0.2 mm/s (55.7 $\mu A/cm^2$). Systems operated at 0.8 mm/s also achieved the current plateau earlier, on day 6, whereas those at 0.2 mm/s reached it on day 8. In contrast, biofilms formed at 0.2 mm/s had approximately doubled the biovolume (4.9 mm^3/cm^2) of those at 0.8 mm/s (2.6 mm^3/cm^2) (Figure 10c–d). Porosity of grown biofilms was also affected by flow conditions. Biofilms at 0.2 mm/s were more porous (17%), while those at 0.8 mm/s were denser, with a porosity of 5.3%. The corresponding biofilm height profiles are shown in Figure 11 for days 2, 4, 6, and 8 at 0.2 mm/s, and for days 2, 4, and 6 at 0.8 mm/s. OCT analysis showed biofilms formed under higher flow remained thinner and more uniform, indicating the effects of shear stress on biofilm development and morphology.

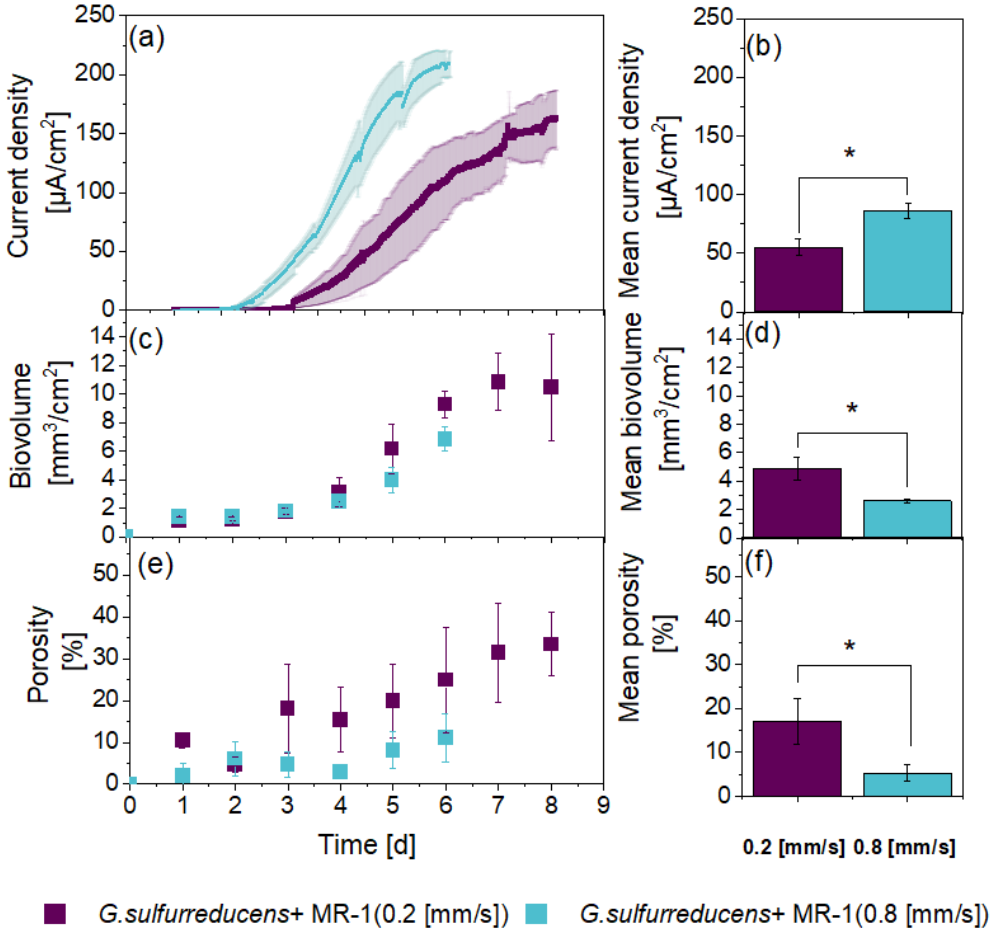

Figure 10. Biofilm development and electrochemical performance of *G. sulfurreducens–S. oneidensis* MR-1 cocultures under flow velocities of 0.2 and 0.8 mm/s. (a, b) current density, (c, d) biovolume, and (e, f) porosity over time with corresponding mean values. Statistical significance: * = $p < 0.05$; **= $p < 0.01$.

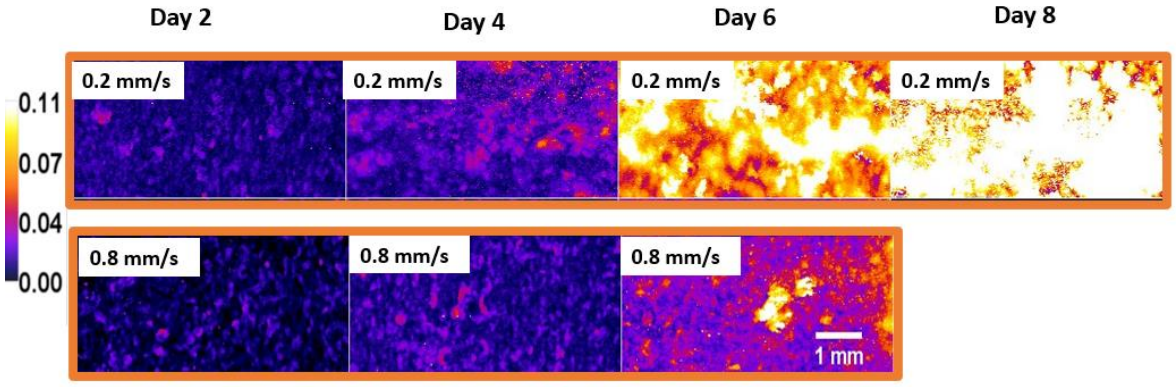

Figure 11. Optical coherence tomography (OCT) images showing biofilm development by *G. sulfurreducens–S. oneidensis* MR-1 cocultures on the anode surface under flow velocities of 0.2 and 0.8 mm/s. Biofilms were monitored over 8 days at 0.2 mm/s and 6 days at 0.8 mm/s; the biofilm at 0.8 mm/s was not imaged after day 6, as the experiment reached a steady state and therefore stopped). Each image represents the electrode surface where the flow direction was from left to right. Each panel presents a top-view, color-coded height map of the biofilm, with the legend indicating thickness in millimeters.

To determine whether the influence of flow velocity on biofilm structure is driven entirely by mechanical forces or also by cellular regulatory responses affected by the partnership between *S. oneidensis* and *G. sulfurreducens* or not, the system was operated using a mono-culture of *G. sulfurreducens* with acetate as the sole carbon and electron source under the same flow conditions (0.2 and 0.8 mm/s). This is to understand the potential dependency of the overall response to flow velocity on the catabolic activity of *S. oneidensis* and the corresponding role in biofilm structure.

Previous experiments had shown that *S. oneidensis* monocultures develop only minimal biofilm structures, which are below the detection limit of OCT analysis. The results of a similar experiment with *S. oneidensis* pure culture would therefore not be informative regarding the impact of flow velocity on biofilm structure (Figure 12). In contrast to the co-culture, where flow velocities of 0.2 and 0.8 mm/s resulted in pronounced differences in current density, biovolume, and porosity, the *G. sulfurreducens* monoculture showed no significant difference at both flow conditions. At 0.2 and 0.8 mm/s, mean current density of 87.8 and 90.4 $\mu A/cm^2$, mean biovolume of 1.83 and 2.02 mm^3/cm^2, and mean porosity of 11.3 and 9.7% were obtained, respectively. Moreover, the current density and biovolume reached a steady-state within 4 days at both flow velocities, which was earlier than in the co-culture. Besides the widely proved efficiency and robustness of *G. sulfurreducens* biofilms, this observation is attributed to the fact that no acetate limitation is expected throughout the experimental period.

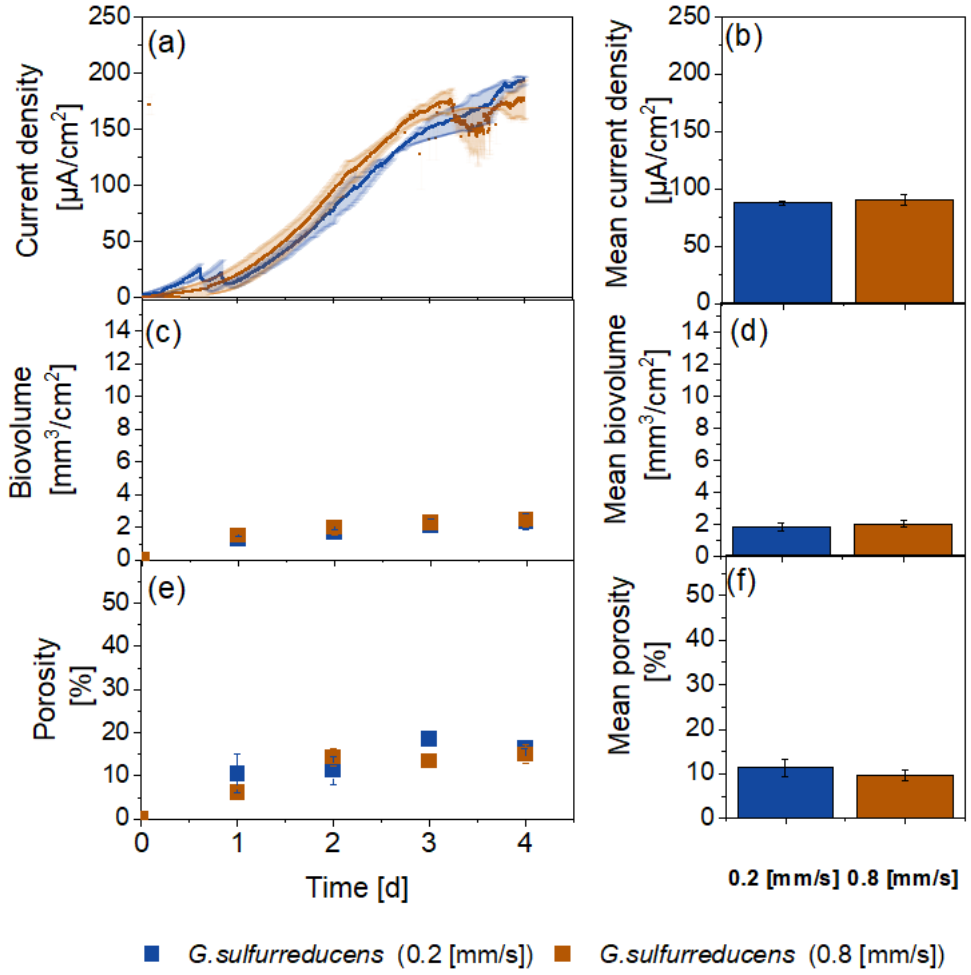

Figure 12. Biofilm development and electrochemical performance of *G. sulfurreducens* monocultures under flow velocities of 0.2 and 0.8 mm/s. (a, b) current density, (c, d) biovolume, and (e, f) porosity over time with corresponding mean values.

3.1.2. Response of developing co-culture biofilms to flow velocity shift

To test whether the response to flow condition was because of modulation of biofilm chemistry, which should be longer-lasting and not easily reversible, the coculture biofilms grew for four days (i.e., phase 1) in six independent microfluidic reactors under the higher flow velocity of 0.8 mm/s, then three of the reactors were switched to the lower flow velocity of 0.2 mm/s on day four (i.e., phase 2). Figure 13 shows the results of this analysis. Reducing the flow velocity from 0.8 to 0.2 mm/s resulted in only minor, statistically insignificant changes compared to biofilms grown at a constant 0.8 mm/s. In Phase 2, current density slightly decreased from 185

to 157 µA/cm², biovolume changed only slightly from 5.4 to 5.1 mm³/cm², and porosity increased modestly from 9.1 to 10.4%. Corresponding OCT images at days 2, 4, and 6 are shown in Figure 14 and show a similarity in biofilm morphology in both flow velocities.

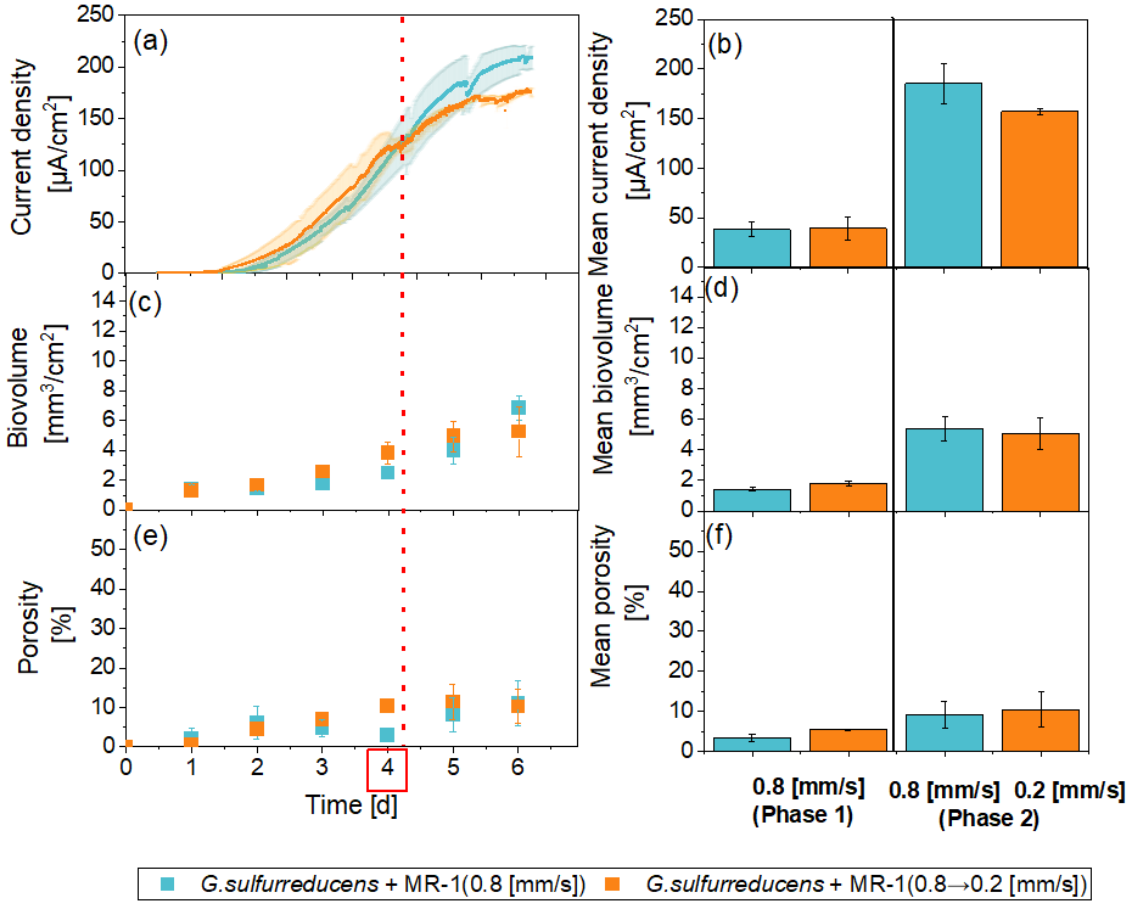

Figure 13. Effect of flow velocity (constant 0.8 mm/ s, shift from 0.8 to 0.2 mm/ s on day 4) on *G. sulfurreducens–S. oneidensis* MR-1 coculture biofilms. (a, b) Current density, (c, d) biovolume, and (e, f) porosity over time with corresponding mean values. The flow shift on day 4 is indicated by the red dashed line.

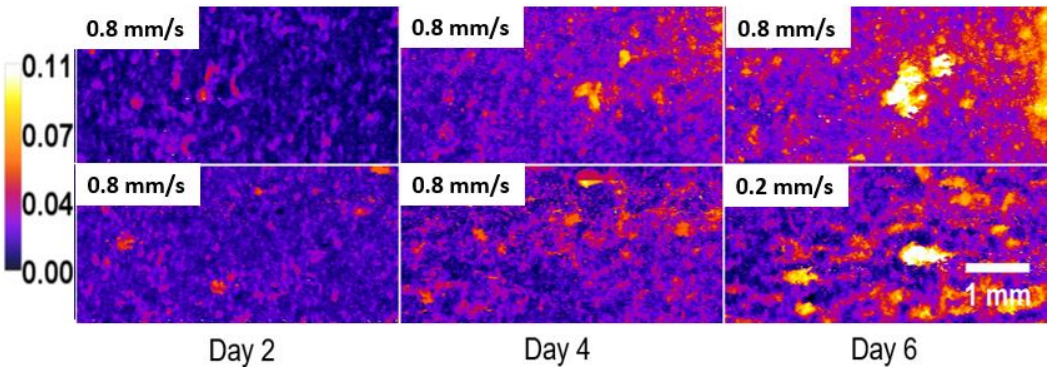

Figure 14. Optical coherence tomography (OCT) visualization of *G. sulfurreducens*–*S. oneidensis* MR-1 coculture biofilm development on the anode surface under a constant flow velocity of 0.8 mm/s and a shifted flow from 0.8 to 0.2 mm/s on day 4, over 6 days, with flow direction from left to right. Each panel shows a top view of the biofilm as a color-coded height map, where the legend indicates biofilm thickness in millimeters. The upper row corresponds to biofilms cultivated at constant flow, while the lower row shows biofilms exposed to the flow shift on day 4.

In the following, an experiment was conducted in reverse, starting with a low flow velocity in six individual microfluidic BES reactors (phase 1) and then switching to a higher flow velocity after four days in three of the reactors (phase 2). The results are depicted in Figure 15. When the flow velocity was increased from 0.2 to 0.8 mm/s, biofilms responded differently compared to those maintained at constant low flow (0.2 mm/s). After the shift, the mean current density rose to 151 µA/cm², significantly higher than the 98 µA/cm² observed under constant low flow. Biovolume, however, was lower in the shifted condition, reaching only 2.4 mm³/cm², compared to 9.1 mm³/cm² under constant low flow. Porosity also decreased substantially from 30.3% to 9.7%, indicating the formation of a denser biofilm.

The height profiles of biofilms developed under both flow conditions are shown in Figure 16, highlighting clear morphological differences between biofilms grown at a constant velocity of 0.2 mm/s, which exhibited greater thickness, and those exposed to a flow increase to 0.8 mm/s in Phase 2.

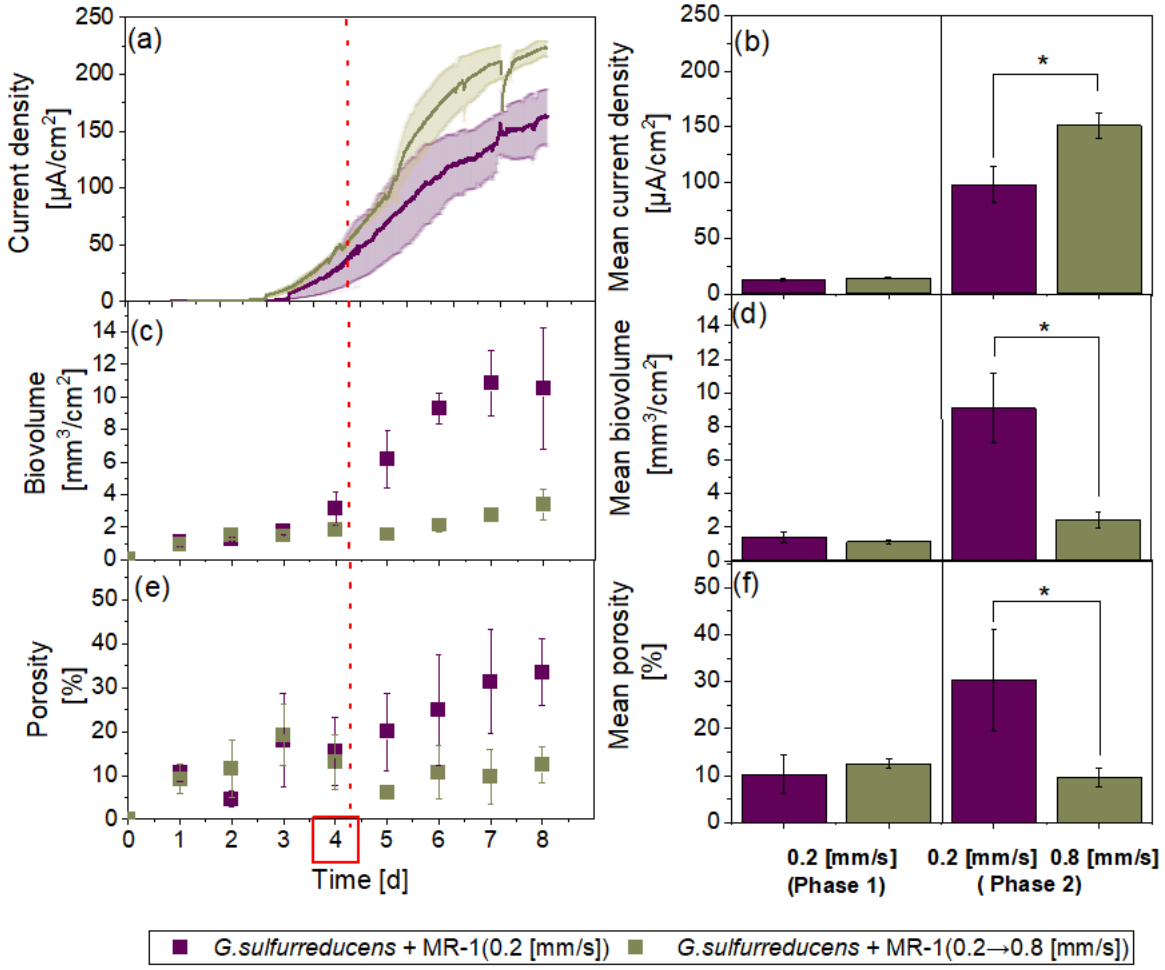

Figure 15. Effect of flow velocity (constant 0.2 mm/s vs. shift from 0.2 to 0.8 mm/s on day 4, indicated by the red dashed line) on *G. sulfurreducens–S. oneidensis* MR-1 coculture biofilms. (a, b) current density, (c, d) biovolume, and (e, f) porosity over time with corresponding mean values.

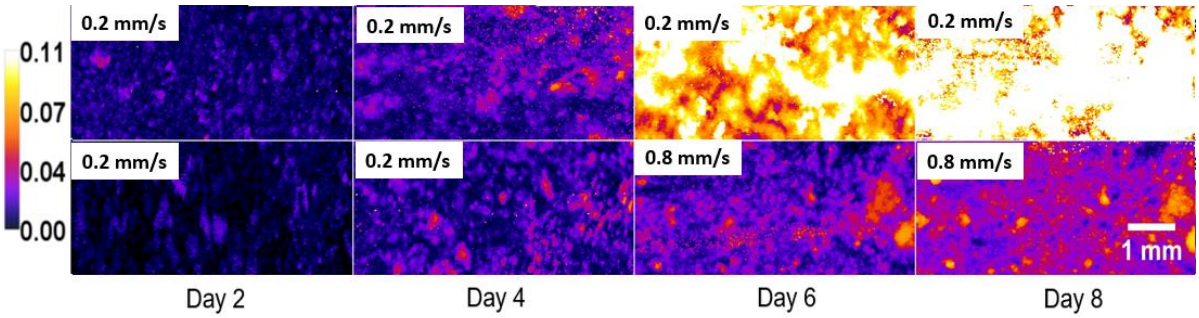

Figure 16. Optical coherence tomography (OCT) visualization of *G. sulfurreducens–S. oneidensis* MR-1 coculture biofilm development on the anode surface under a constant flow velocity of 0.2 mm/s and a shifted flow velocity from 0.2 to 0.8 mm/s on day 4 over 8 days, with flow direction from left to right. Each panel shows a top view of the biofilm as a color-coded height map, where the legend indicates biofilm thickness in millimeters. The upper row corresponds to biofilms cultivated at constant flow, while the lower row shows biofilms exposed to the flow shift on day 4.

3.1.3. Transcriptomic response of biofilms to flow velocity

As evidence from the previous experiments pointed towards a regulatory response of foremost *S. oneidensis* cells to shear stress, a transcriptomic analysis was performed on co-culture biofilms cultivated at constant flow velocities of 0.2 and 0.8 mm/s. The relative transcriptional activity was compared between the two flows at days 4, 6, and 8, correlating with active biofilm growth and steady state conditions, respectively. *G. sulfurreducens* was the dominant contributor to transcriptomic reads under all conditions, showing only a slight decrease in activity at higher flow velocities and steady state. In contrast, *S. oneidensis* exhibited a strong flow-dependent response, with low and declining activity at 0.2 mm/s but increased gene expression at 0.8 mm/s (Table 12).

Table 12. Relative transcriptional activity and corresponding TPM value of *G. sulfurreducens* and *S. oneidensis* in the co-culture biofilm when subjected to different flow velocities.

Flow velocity	Phase 1			Phase 2		
	G. sulfurreducens	*S. oneidensis*	*SD*	*G. sulfurreducens*	*S. oneidensis*	*SD*
0.2 mm/s	99.0 % [845749]	1.00 % [8959]	0.011	99.18 % [777570]	0.82 % [7296]	0.007
0.8 mm/s	97.49 % [821641]	2.51 % [21770]	0.014	95.85 % [804496]	4.15 % [35976]	0.017

SD: Standard deviation

Figure 17 presents the volcano plot of genes differentially expressed in Phase 1 for biofilms grown under flow velocities of 0.2 and 0.8 mm/s. This Phase also corresponds to the stage when strain-specific differences in biofilm formation were most evident. A total of 74 genes

showed differential expression between biofilms grown under 0.2 mm/s and 0.8 mm/s, with 98.6 % belonging to *S. oneidensis* (see Appendix; Table S1). Moreover, the eight *S. oneidensis* genes exhibiting the highest significant expression differences ($p < 0.1$, fold change > 5) between the two applied flow velocities are shown in Table 13.

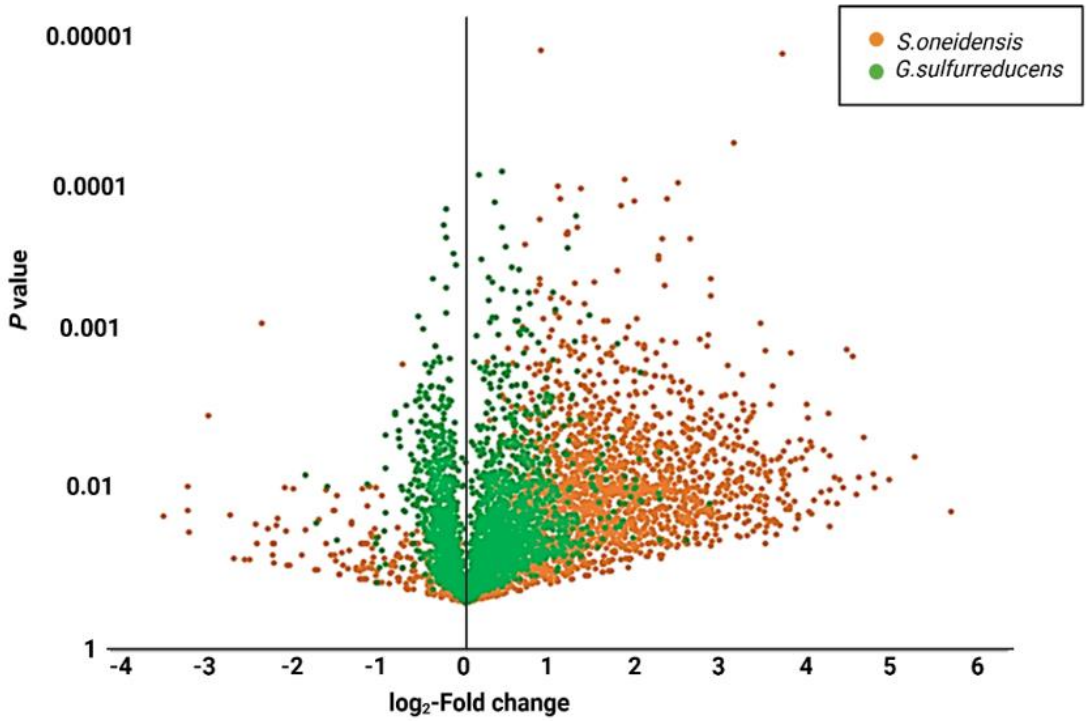

Figure 17. Volcano plot of differential gene expression between 0.2 mm/s and 0.8 mm/s in phase 1. Each point represents a gene, with fold change (log_2 scale) on the x-axis and statistical significance (*p*-value, log_{10} scale) on the y-axis.

Table 13. List of the most differentially expressed genes identified in the co-culture biofilm when subjected to different flow velocities.

Name	Function	Fold change	*p*-value
SO_2005	TraR/DksA C4-type zinc finger protein	-13.68	0.09
SO_3759	Sensor domain-containing diguanylate cyclase	-8.67	0.08
SO_3960	LPS export ABC transporter ATP-binding protein	-5.09	0.06
SO_3271	UDP-N-acetylglucosamine 4,6-dehydratase (inverting)	10.66	0.03
SO_4323	**EAL domain-containing protein**	**10.67**	**0.03**
SO_1531	tRNA uracil 4-sulfurtransferase ThiI	11.33	0.02
SO_2956	phage tail tube protein	11.77	0.002
SO_3191	Wzz/FepE/Etk N-terminal domain-containing protein	13.16	0.05

Among the top differentially expressed genes, SO_4323, which encodes the EAL domain-containing protein (*bpfD*), displayed the strongest differential expression response to different flow velocities (+10.67-fold).

Meanwhile, to further assess the potential contribution of *bpfD* on biofilm structure/efficiency when being subjected to different flow velocities, a mutant strain (MR-1 Δ*bpfD*) was constructed. Its planktonic growth was compared with the wild type, and its growth trend was completely similar to the wild type (see Appendix; Figure S1). Its biofilm formation and electrochemical responses were compared with those of the wild type under flow transitions (0.8 → 0.2 mm/s and 0.2 → 0.8 mm/s), in the following subsections, to assess the specific contribution of this gene to biofilm regulation under changing hydrodynamic conditions.

3.1.4. Role of the *bpfD* in biofilm response to flow velocity

To evaluate the role of SO_4323 (*bpfD*) in flow-dependent biofilm regulation, *G. sulfurreducens* was cocultured with either wild-type *S. oneidensis* MR-1 or MR-1 Δ*bpfD*. Biofilm formation and electrochemical performance were assessed under two flow transitions:

a decrease from 0.8 to 0.2 mm/s and an increase from 0.2 to 0.8 mm/s in flow velocity. Current density, biovolume, and porosity were measured to evaluate structural and functional responses to changing hydrodynamic conditions.

Under decreasing flow velocity from 0.8 to 0.2 mm/s (Figure 18), cocultures with MR-1 Δ*bpfD* produce significantly lower current densities compared to those with wild-type S. *oneidensis* MR-1. In Phase 1, the mutant produced a mean current density of 5.23 µA/cm², approximately 7.5-fold lower than that of the wild type (39.5 µA/cm²). In Phase 2, this difference remained substantial, with the mutant reaching 38.5 µA/cm² compared to 157 µA/cm² for the wild type. Despite the reduced electrochemical activity, the mutant formed biofilms with higher biovolume, 2.87 mm³/cm² vs. 1.8 mm³/cm² in Phase 1, and 8.6 mm³/cm² vs. 5.08 mm³/cm² in Phase 2. Porosity was also higher in the mutant, with values of 6.79% compared to 4.4% in Phase 1 and 19.33% compared to 10.2% in Phase 2. These results suggest that *bpfD* inactivation leads to the formation of thicker, more porous biofilms but compromises electrochemical performance under reduced flow conditions. Distinct differences in biofilm height and morphology were evident from day 4 in the OCT images, with the mutant biofilms showing increased thickness, particularly pronounced by day 6 (Figure 19).

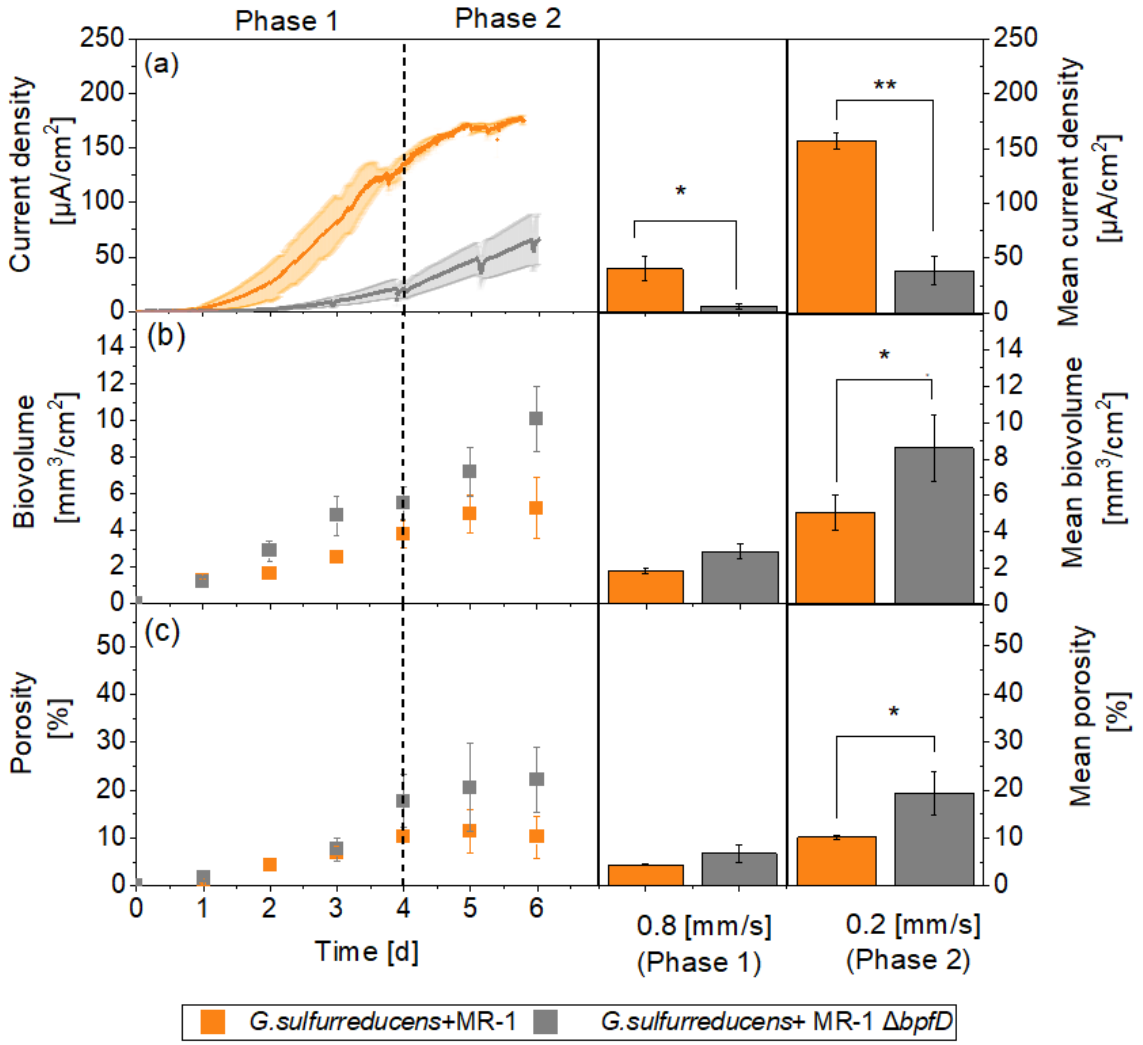

Figure 18. Effect of decreasing flow velocity (from 0.8 to 0.2 mm/s) on electrochemical performance and biofilm structure in *G. sulfurreducens–S. oneidensis* MR-1 and *G. sulfurreducens–S. oneidensis* MR-1 Δb*pfD* cocultures. Biofilms were compared under identical flow conditions: Phase 1 (0.8 mm/s) and Phase 2 (0.2 mm/s). (a, b) current density, (c, d) biovolume, and (e, f) porosity over time with corresponding mean values. Statistical significance: *= $p < 0.05$; **= $p < 0.01$.

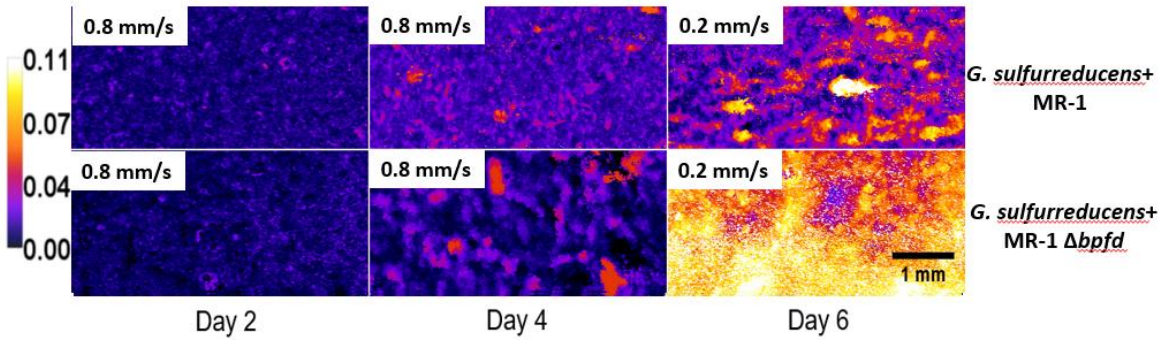

Figure 19. Optical coherence tomography (OCT) visualization of *G. sulfurreducens–S. oneidensis* MR-1 and *G. sulfurreducens–S. oneidensis* MR-1 Δ*bpfD* coculture biofilm

development on the anode surface under a flow regime decreasing from 0.8 to 0.2 mm/s over 6 days. Flow direction is from left to right. Each panel shows a top view of the biofilm as a color-coded height map; the scale bar indicates biofilm thickness in millimeters.

To assess the response of established co-culture biofilms to increased shear stress, the flow velocity was raised from 0.2 mm/s to 0.8 mm/s on day 4. In Phase 1, the wild-type coculture reached a mean current density of 14.3 µA/cm², while the *bpfD* mutant reached 3.16 µA/cm². In Phase 2, current densities increased to 152 µA/cm² for the wild type and 81 µA/cm² for the mutant. Biovolume remained comparable between cocultures in both Phases, with 1.13 and 1.10 mm³/cm² in Phase 1, and 2.43 and 2.33 mm³/cm² in Phase 2 for the wild type and mutant, respectively. As shown in Figure 20e-f, porosity was similar in Phase 1 (12.5 % and 14.7 %). Still, in Phase 2, the mutant biofilms showed a much higher mean porosity of 32.9 % compared with 9.7 % for the wild type, along with a more heterogeneous structure, as illustrated in Figure 21.

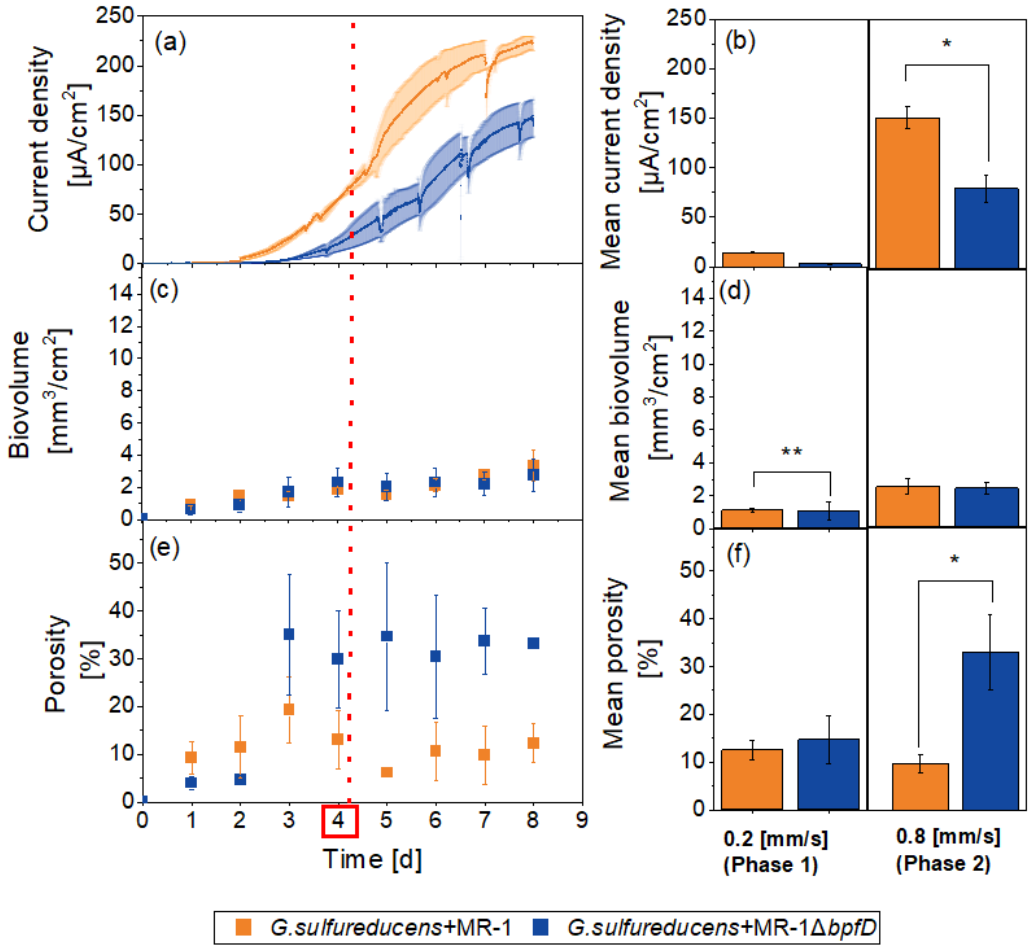

Figure 20. Effect of increasing flow velocity (from 0.2 to 0.8 mm/s) on electrochemical performance and biofilm structure in *G. sulfurreducens–S. oneidensis* MR-1 and *G. sulfurreducens–S. oneidensis* MR-1 Δ*bpfD* cocultures. Biofilms were compared under identical flow conditions: Phase 1 (0.2 mm/s) and Phase 2 (0.8 mm/s). (a, b) current density, (c, d) biovolume, and (e, f) porosity over time with corresponding mean values. Statistical significance: *= $p < 0.05$; **= $p < 0.01$.

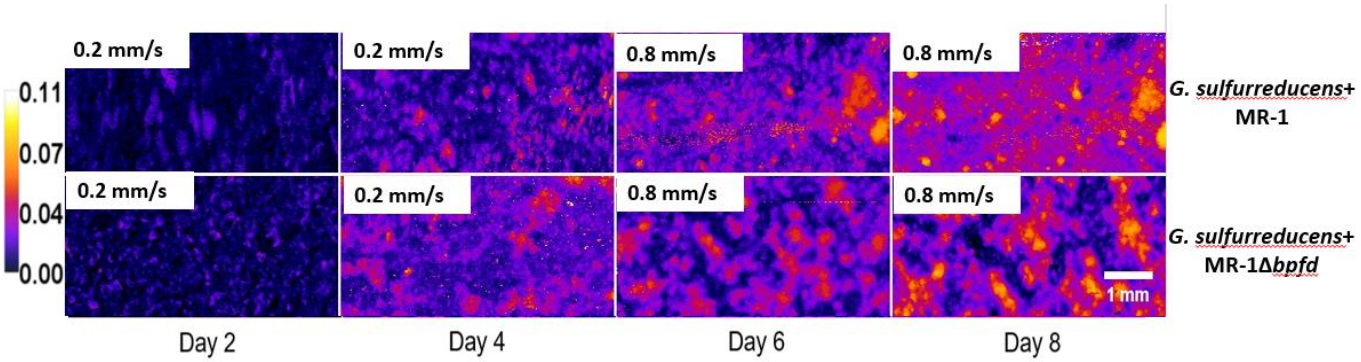

Figure 21. Optical coherence tomography (OCT) visualization of *G. sulfurreducens–S. oneidensis* MR-1 and *G. sulfurreducens–S. oneidensis* MR-1 Δ*bpfD* coculture biofilm development on the anode surface under a flow velocity increasing from 0.2 to 0.8 mm/s on day 4 over 8 days. Flow direction is from left to right. Each panel shows a top view of the biofilm as a color-coded height map; the scale bar indicates biofilm thickness in millimeters.

The smaller difference in current output compared to the decreasing flow experiment suggests that the effect of *bpfD* inactivation is less pronounced when biofilm formation begins under low-flow velocity conditions.

3.2. Effect of substrate concentration on MEC performance

The second operational parameter evaluated was the substrate concentration, which was studied for its influence on electrochemical performance, substrate utilization, and microbial community structure. The influence of substrate concentration on MEC performance was evaluated using hydrolysate concentrations of 20%, 40%, and 60% over 72 h, corresponding to the time required to reach the steady state current density (see Appendix; Figure S2). Substrate concentration was measured every 24 hours throughout the experiment (see Appendix; Figure S3). Concentrations above 60% were not tested, as preliminary trials showed a marked decrease in system efficiency at higher loadings. All experiments were conducted in a Cylindrical-MEC operated under anoxic, batch conditions using unsterile hydrolysate. Testing different substrate concentrations was important because both insufficient and excessive loading can influence microbial activity and overall system performance. The analysis focused on three main aspects: (i) substrate removal rates, specifically acetate, propionate, and butyrate, as indicators of carbon utilization; in(ii) system performance, assessed through the mean current density (average of current density values recorded during the experiment) and CE; and (iii) microbial community composition, to relate system performance to the anodic microbial population. CE was calculated using both VFAs and TOC to provide complementary information. VFA-based CE represented electron recovery from acetate, propionate, and butyrate, while TOC-based CE accounted for the total organic content of the hydrolysate, including complex and slowly degradable compounds. Comparing these

two parameters helped distinguish the fraction of substrate converted into current from that lost to competing processes. Additionally, carbon removal rates derived from TOC profiles were compared with those obtained from individual VFAs (see Appendix; Figure S4), allowing evaluation of the relative contribution of different carbon fractions to total substrate utilization. Mean current density varied with hydrolysate concentration (Figure 22a). The highest value was observed at 40% hydrolysate (0.46 A/m²), while both 20% and 60% hydrolysate resulted in lower current densities, 0.34 and 0.27 A/m², respectively. Substrate removal increased with hydrolysate concentration. At 60% hydrolysate, acetate, propionate, and TOC removal rates reached maximum values of 2.9, 2.2, and 32.6 mM/d, respectively. Acetate removal was the most efficient at all concentrations, while butyrate removal remained consistently low (Figure 22b). CE also varied with hydrolysate concentration (Figure 22c). The TOC-based CE was highest at 40% hydrolysate (12.7%), decreasing to 5.8% at 20% and 2.7% at 60%. VFA-based CE values were higher than TOC-based values across all concentrations, with similar levels at 20% and 40% (24%) and the lowest at 60% (5.53%), indicating that a larger proportion of the readily degradable VFAs contributed to the current generation compared with the total organic content. The microbial community composition at the domain level remained stable across all concentrations (Figure 22d). Bacteria dominated in all samples. At the same time, archaea accounted for a minor fraction, increasing from 1.9% at 20% hydrolysate to 3.9% at 40% and 60%. At the genus level (Figure 22e), *Azospira* was most abundant at 20% hydrolysate. At 40% hydrolysate, *Petrimonas*, *Macellibacteroides*, *Proteiniphilum*, and *Geobacter* were relatively more abundant. At 60% hydrolysate, *Azospira* and sulfate-reducing bacteria such as *Solidesulfovibrio* showed increased abundance.

The results showed that hydrolysate concentration affected MEC performance. The highest current density and CE were achieved at a 40% hydrolysate concentration, while substrate removal rates were highest at a 60% concentration. The 40% concentration was selected for

subsequent experiments because it provided a good balance between electrochemical performance and substrate conversion efficiency.

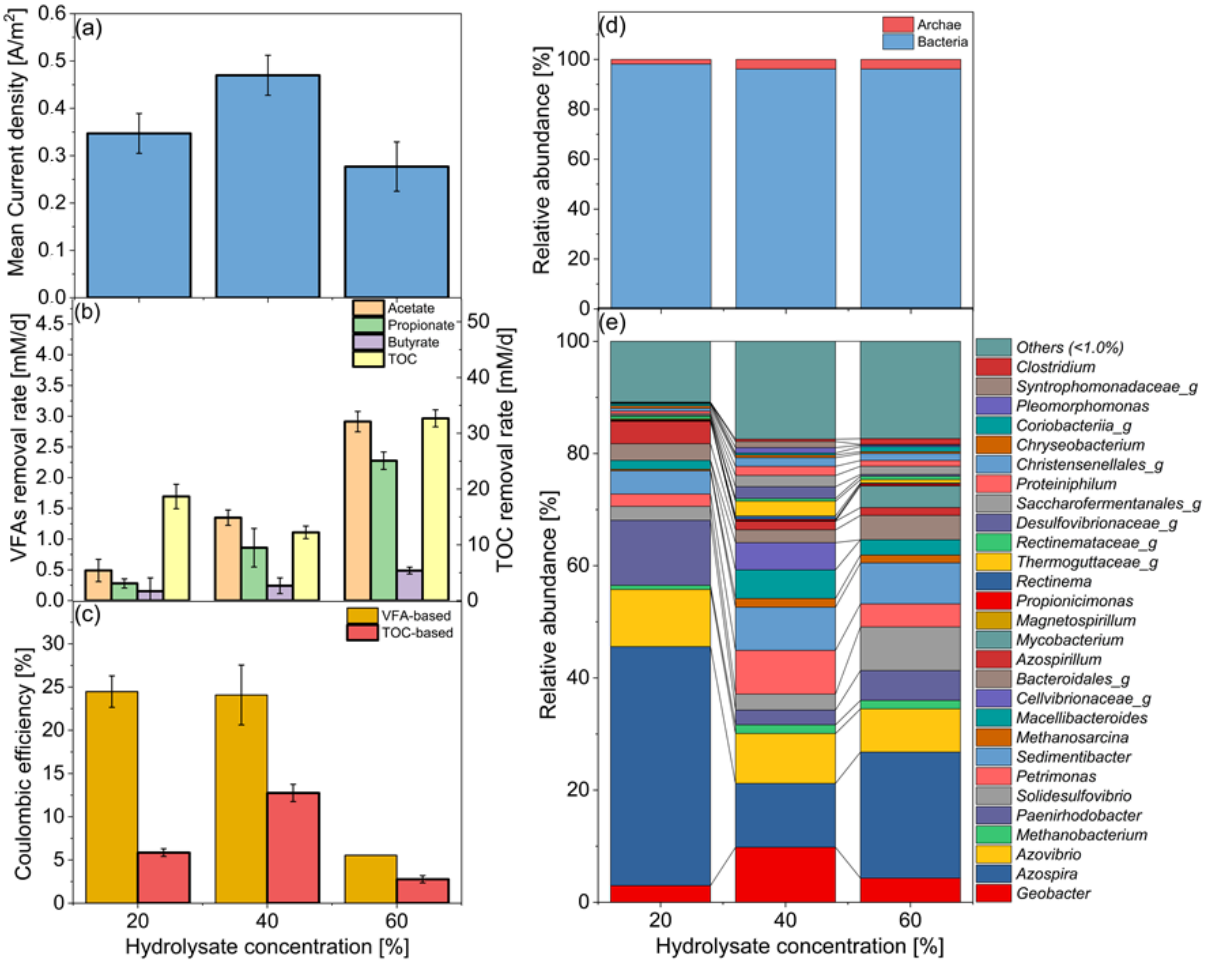

Figure 22. Effects of hydrolysate concentration (20%, 40%, and 60%) on microbial electrolysis cell performance. (a) Mean current density, (b) Volatile fatty acids (VFAs) and total organic carbon (TOC) removal rates, (c) Total organic carbon (TOC) and volatile fatty acid (VFA)-based coulombic efficiency (CE), (d) Microbial community composition at the domain level, and (e) Microbial community composition at the genus level.

3.3. Effect of pH on MEC performance

To evaluate the pH influence on MEC performance, experiments were conducted across a pH range of 5–8, covering acidic, neutral, and alkaline conditions commonly used in BESs and

suitable for electroactive microorganisms. MECs were operated at pH 5, 5.5, 6, 6.5, 7, and 8 using 40% hydrolysate (as determined in Section 3.2) and an applied potential of 0 V, with a 1-day operation period required to reach the current density plateau.

Mean current density increased with pH, from 0.06 A/m² at pH 5 to 1.03 A/m² at pH 8 (Figure 23a). Substrate degradation also showed pH dependence (Figure 23b). At pH 5–6.5, acetate and TOC removal were relatively high, while propionate accumulated at pH 5–5.5. The highest removal rates were at pH 6, with acetate, propionate, and butyrate consumed at 7.48, 2.70, and 1.36 mM/d, respectively, alongside TOC removal of 53.15 mM/d. CE increased with pH (Figure 23c). TOC-based CE remained below 1% at pH values below 6, but rose sharply above this level, reaching a maximum of 18.68% at pH 8. VFA-based CE showed no significant difference between pH 7 and 8.

Microbial community composition at the domain level remained stable across pH 5, 7, and 8, with bacteria always dominant (>90%) and archaea representing only a minor fraction (Figure 23d). At the genus level (Figure 27e), acidic conditions (pH 5–6) were associated with higher abundances of fermentative bacteria such as *Petrimonas*, *Sedimentibacter*, and *Macellibacteroides*, as well as methanogens such as *Methanosarcina*. *Azospira* was also more abundant at these pH values. At pH 7, the community shifted toward electrogenic activity, with an increased proportion of *Geobacter* and fewer fermenters. At pH 8, *Geobacter* dominated the anodic biofilm (44% relative abundance), while methanogens were strongly reduced.

Overall, MEC performance increased with rising pH. At pH 5–6, the mean current density and TOC-based CE were low, accompanied by propionate accumulation and higher abundances of fermentative bacteria and methanogens. Performance improved at pH 7, corresponding with an increased relative abundance of *Geobacter*. The highest performance was observed at pH 8, with a current density of 1.03 A/m², a TOC-based CE of 18.68%, efficient VFA utilization, and

Geobacter dominance in the anodic biofilm. Based on these findings, subsequent experiments were conducted at pH 8.

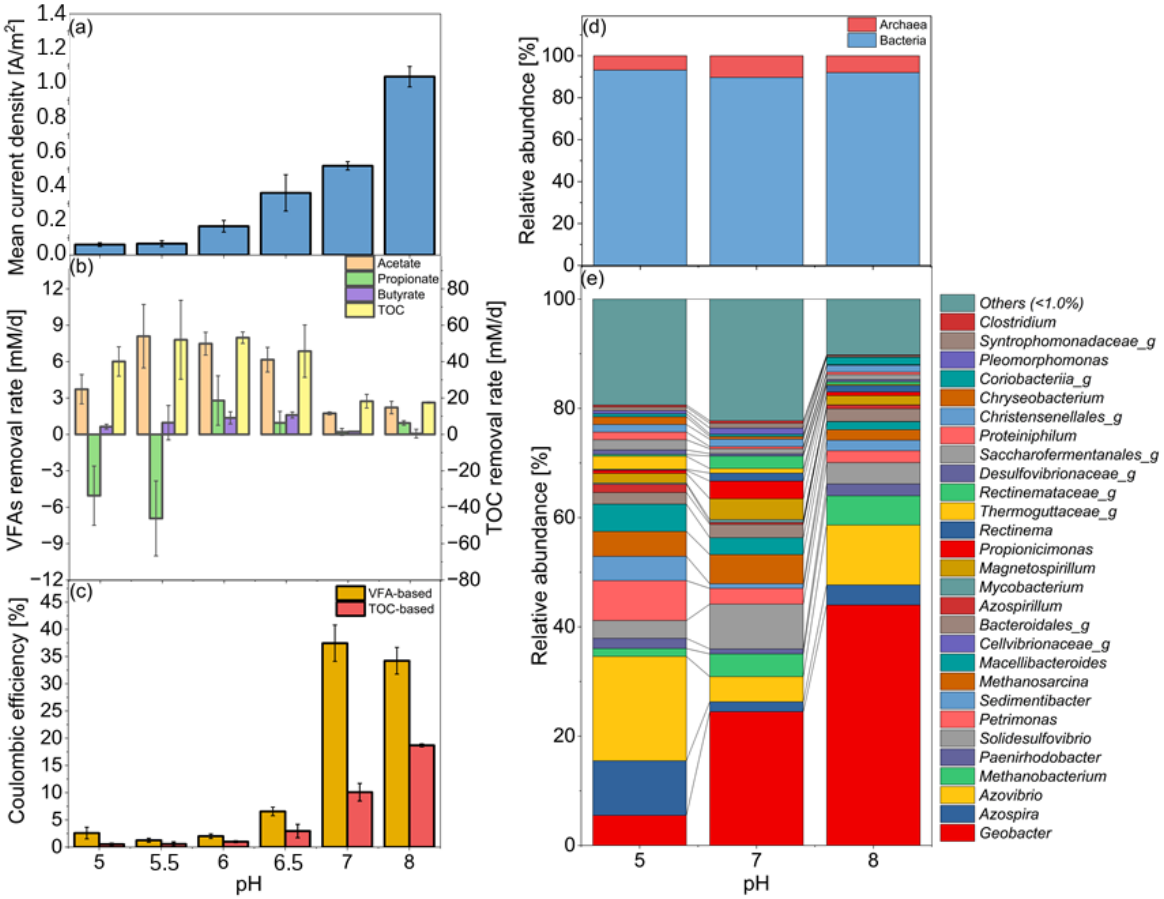

Figure 23. Effects of pH on microbial electrolysis cell (MEC) performance. (a) Mean current density; (b) Volatile fatty acids (VFAs) and total organic carbon (TOC) removal rates, (c) Total organic carbon (TOC) and volatile fatty acid (VFA)-based coulombic efficiency (CE), (d) Microbial community composition at the domain level, and (e) Microbial community composition at the genus level.

3.4. Effect of applied anodic potential on MEC performance

To assess the influence of applied anodic potential on system performance, MECs were operated under different applied potentials, and variations in current density, CE, substrate utilization, and microbial community composition were analyzed. The range of –0.2, 0, 0.2, and 0.4 V vs. SHE was selected to include conditions below, at, and above the commonly used

0 V, allowing assessment of MEC performance under different redox conditions. Potentials higher than +0.4 V were not tested, as they would require excessive energy input, may promote side reactions, and are less relevant for practical MEC operation. MECs were operated at these potentials with 40% hydrolysate at pH 8 for 1 day.

Mean current density increased with applied potential (Figure 24a). At –0.2 V, current density was minimal (0.08 A/m²), increased to 0.88 A/m² at 0 V, and further rose to 2.44 A/m² and 3.40 A/m² at 0.2 V and 0.4 V, respectively. Substrate removal also depended on potential (Figure 24b). TOC removal increased from 11.82 mM/d at –0.2 V to 30.24 mM/d at 0.4 V. Acetate removal rose from 0.67 mM/d to 3.92 mM/d across the same range. Propionate degradation peaked at 0–0.2 V but declined at 0.4 V, while butyrate removal remained minimal (<0.1 mM/d) under all conditions.

CE increased progressively with anodic potential (Figure 24c). TOC-based CE rose from 2.29% at –0.2 V to 38% at 0.4 V. VFA-based CE increased from 7.69% at –0.2 V to 95.76% at 0.4 V, indicating nearly complete electron recovery from VFAs at the highest potential.

Microbial community composition also shifted with potential. At the domain level, bacteria remained dominant, while the relative abundance of archaea declined with increasing potential (Figure 24d). At –0.2 V, archaeal abundance was higher (4.4%), with hydrogenotrophic methanogens such as *Methanobacterium* present, along with fermentative taxa such as *Sedimentibacter* (4.99%) and *Bacteroidales_g* (4.13%) (Figure 24e). Under these conditions, *Geobacter* was present at low relative abundance. With increasing potential, microbial community structure shifted toward higher proportions of exoelectrogens and lower proportions of methanogens and sulfate-reducing bacteria. At 0.4 V, MEC performance peaked, with *Geobacter* dominating the anodic biofilm, while methanogens and *Solidesulfovibrio* were strongly reduced.

Overall, MEC performance improved with increasing anodic potential. The highest current density (3.4 A/m²), substrate removal rate (30.24 mM/d), and TOC-based CE (95.76%) were obtained at 0.4 V. This condition was also characterized by a dominant presence of *Geobacter* in the anodic community and reduced abundances of methanogens and other competing microorganisms.

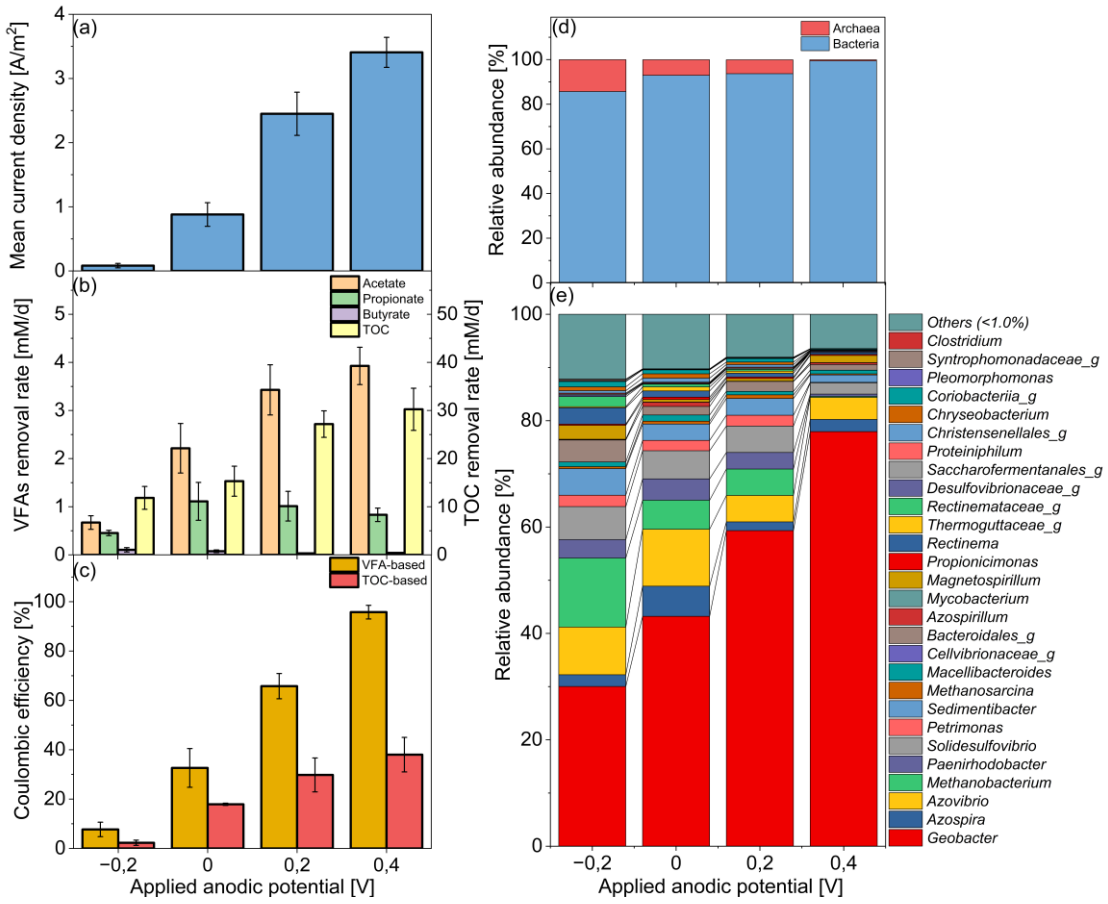

Figure 24. Effect of applied anodic potential (–0.2 to 0.4 V vs. SHE) on microbial electrolysis cell performance. (a) Mean current density, (b) VFAs (acetate, propionate, butyrate) and total organic carbon removal rates, (c) Total organic carbon (TOC) and volatile fatty acid (VFA)-based coulombic efficiency (CE), (d) Microbial community composition at the domain level, and (e) Microbial community composition at the genus level.

3.5. Multivariate analysis of MEC performance and microbial dynamics

To assess the relationships among the tested parameters, performance indicators, and anodic microbial dynamics, principal component analysis (PCA) was performed. For performance indicators, the first two principal components (PC1 and PC2) explained 75.2% of the total variance (Figures 25a and 25b). The score plot (Figure 25a) showed distinct separation of samples operated at acidic pH (<7) from those at higher pH values. Variations were also observed with changes in applied anodic potential from –0.2 to +0.4 V vs. SHE. The loading plot (Figure 25 b) indicated that pH and anodic potential contributed more strongly to the observed variance than hydrolysate concentration. Mean current density, CE, and anodic potential clustered closely, showing strong positive correlations. In contrast, acetate, butyrate, and TOC removal rates correlated more strongly with hydrolysate concentration and showed weaker correlations with current density and CE.

When analyzing microbial community composition, PCA of genus-level data (Figures 25c and 25d) showed that PC1 and PC2 together explained 68.3% of the total variance. pH contributed most strongly to the observed differences, while anodic potential and hydrolysate concentration had lower but comparable contributions. The loading plot (Figure 25d) showed a strong positive correlation between *Geobacter* and both pH and anodic potential. In contrast, *Geobacter* was negatively correlated with several other genera, including *Methanosarcina*. A positive correlation between *Geobacter* and *Methanobacterium* was also observed.

To further investigate microbial relationships, a co-occurrence network was constructed using significant Spearman correlations among genera with relative abundances above 1% (Figure 26). In the network, node size reflected the maximum abundance of each genus across all conditions. *Geobacter* was the most abundant genus and showed mainly negative correlations with other genera, including *Azospira*, *Clostridium*, *Petrimonas*, and *Azospirillum*. *Azospira*

was also abundant and exhibited a negative correlation with *Geobacter*. Positive correlations were observed among several non-exoelectrogenic genera such as *Clostridium*, *Methanosarcina*, *Petrimonas*, *Sedimentibacter*, *Desulfovibrionaceae*, and *Syntrophomonadaceae*. Analysis of closeness centrality indicated that *Geobacter* and these genera were the most connected taxa in the network, highlighting their central roles in the anodic community under the tested conditions.

The PCA and network analyses demonstrated that pH and anodic potential were the dominant factors shaping MEC performance and microbial dynamics, with *Geobacter* emerging as the most central and negatively correlated genus in the anodic community.

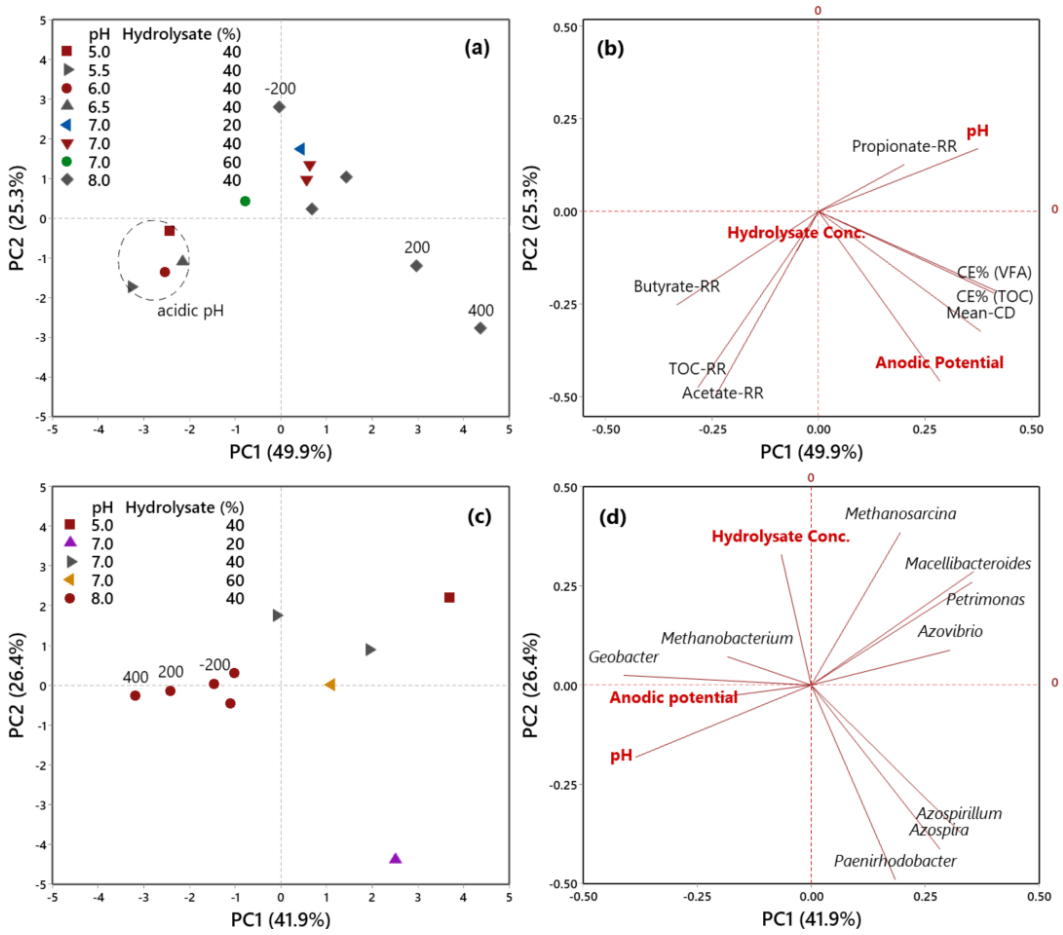

Figure 25. Principal component analysis (PCA) of tested parameters (hydrolysate concentration, pH, and anodic potential; potentials presented in mV and equal to 0 vs. SHE unless otherwise specified). (a, b) Score and loading plots based on MEC performance indicators; (c, d) Score and loading plots based on the relative abundance of major genera identified in the anodic community.

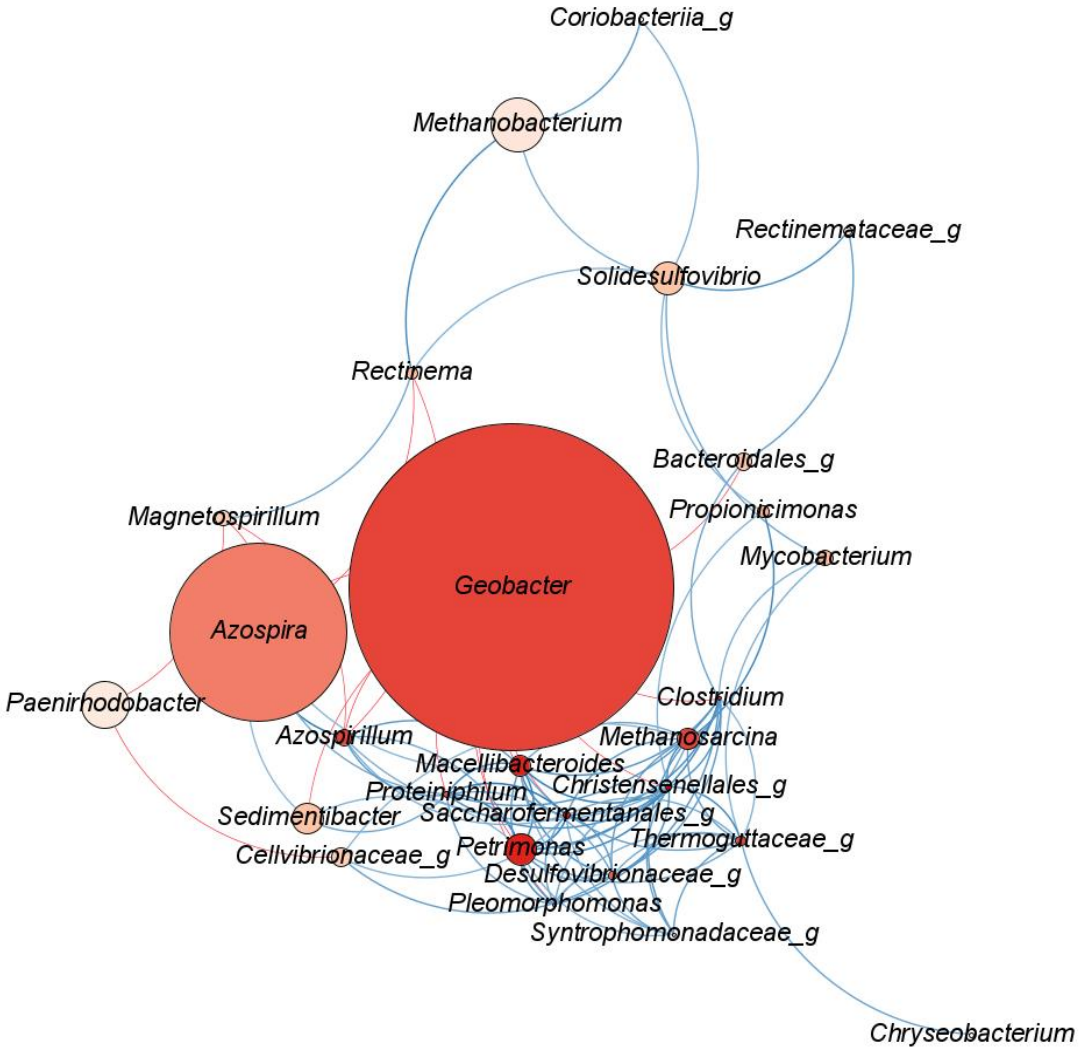

Figure 26. Network analysis showing microbial interactions within the anodic community under the tested conditions. Only significant correlations ($p < 0.1$) are displayed. Node size represents the maximum relative abundance of each genus across all samples. Blue and red edges indicate positive and negative correlations, respectively. Node color reflects the closeness centrality rank, with red indicating the highest and white the lowest.

3.6. Upscaling in a 10 L-RDBER

3.6.1. Effect of pH on MEC performance and methanogens

To assess whether the optimum parameters identified in the Cylindrical-MECs could be applied at a larger scale, experiments were carried out in a 10 L RDBER. Since the optimization experiments in 250 mL Cylindrical-MECs showed that pH strongly affects microbial activity,

substrate utilization, and electron transfer, different pH values were sequentially tested in the RDBER for validation and long-term assessment under scale-up conditions. Meanwhile, the objective was mainly to assess the long-term impact of pH changes on maintaining high hydrogen productivity while minimizing methanogenesis.

The system was first operated with BES medium containing 15 mM acetate and inoculated with *G. sulfurreducens* at an initial OD_{600} of 0.1. The reactor was maintained for 8 days at pH 7 to allow biofilm enrichment. When the current density declined due to substrate depletion, the medium was replaced with unsterile 40% hydrolysate. From that point, the effects of pH on current density, acetate, and TOC concentrations were monitored over 110 days of operation (Figure 27). Propionate and butyrate were also measured, but their consumption was negligible and therefore not shown.

At pH 7, the current density peaked at 1.1 A/m^2 on day 36. Acetate and TOC concentrations subsequently decreased to 1 mM and 46 mM, respectively, by day 44, after which 15 mM acetate was added. Methane production began after 37 days of operation (in another similar run conducted at pH 7, it began after 45 days; metagenomic analysis for this run is provided in the Appendix; Figure S5). To examine whether acidic conditions could suppress methanogenesis, the pH was lowered to 6. This caused the current density to drop to 0.13 A/m^2, yet methane formation continued, reaching 58%. Further reduction to pH 5 produced a similar outcome (CH_4 content of 56%). Although acetate and TOC were still consumed, the current remained near zero, indicating that carbon was mainly utilized by non-electrogenic microorganisms. The pH was cycled between 5 and 7 four times over extended periods, but acidic conditions failed to inhibit methanogenesis; CH_4 levels increased up to 84%, accompanied by a further decline in electrogenic activity. After 84 days, the pH was raised to 11 and maintained for five days, during which the current dropped to zero, indicating a

complete loss of exoelectrogen activity. When the pH was subsequently adjusted back to 8 and maintained for 48 hours, no recovery of electroactivity was observed.

To restore performance, the reactor was re-inoculated and supplemented with 15 mM acetate. Following reinoculation, the current generation recovered, and methane levels remained low (maximum 9% then reduced to 3 %) for approximately 20 days. Under these conditions, hydrogen became the dominant gas component (>97%), and the current density peaked at 2.02 A/m², reflecting a markedly higher system efficiency compared to other pH conditions.

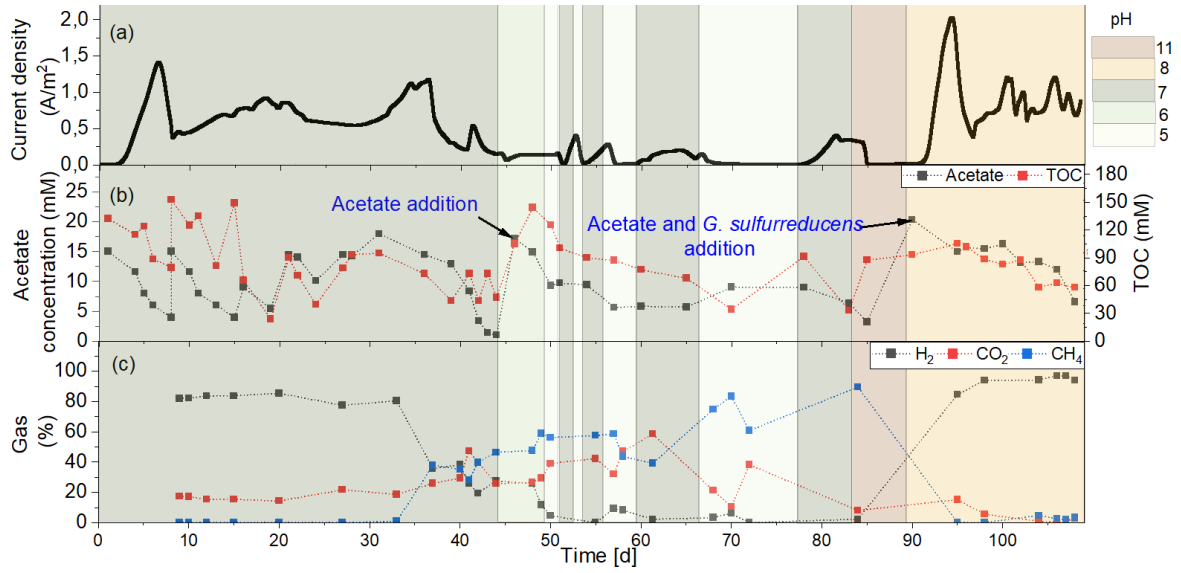

Figure 27. Effect of pH on RDBER performance over 110 days of operation. (a) Current density, (b) Acetate and TOC concentrations, and (c) Gas composition (%) (H_2, CO_2, and CH_4). Acetate and *G. sulfurreducens* additions are indicated by arrows. The shaded background colors represent different pH levels, as shown in the legend.

3.6.2. Effect of applied anodic potential on MEC performance

Based on the optimum parameters identified in the Cylindrical-MEC and the optimum pH determined in Section 3.6.1, the RDBER was operated with 40% hydrolysate at pH 8. To assess the effect of applying an anodic potential under scale-up conditions, the reactor was operated

at 0 V and +0.4 V vs. SHE, while monitoring current density, substrate consumption, gas composition, and hydrogen production as indicators of system performance and stability.

The experiment started with a 7-day enrichment Phase using *G. sulfurreducens* in synthetic medium. After enrichment, the medium was replaced with 40% unsterile hydrolysate at pH 8, and an anodic potential of 0 V vs. SHE was applied for 7 days. During this period, the current density gradually increased, reaching a maximum of 1.12 A/m² (Figure 28a). After acetate was depleted, the reactor was refed with 40% unsterile hydrolysate, and the anodic potential was increased to +0.4 V. Under these conditions, the current density rose to a peak of 1.94 A/m² (Figure 28a). Acetate and TOC concentrations decreased steadily throughout operation, while propionate and butyrate showed minimal consumption (Figure 28b). Substrate degradation increased during the +0.4 V Phase, with faster acetate and TOC removal rates. Gas analysis showed that hydrogen was the dominant product, accounting for over 80% of the total gas fraction. Methane concentrations remained negligible despite the use of unsterile hydrolysate, and only small amounts of CO_2 were detected, reaching a maximum of 15.8% (Figure 28c). Hydrogen production and cell voltage were monitored as indicators of energy recovery efficiency (Figure 28d). Monitoring cell voltage provided insight into the required energy of the system, representing the external energy input needed to maintain current generation and hydrogen production. Hydrogen yield increased with applied anodic potential, reaching a maximum of 30.57 L-H_2/m²·d at +0.4 V, compared with 20.37 L-H_2/m²·d at 0 V.

The results showed that operating the RDBER at a higher anodic potential (+0.4 V) resulted in higher current density, faster substrate degradation, and greater hydrogen production compared with 0 V. Methane levels remained low under both conditions, indicating stable performance of the optimized anodic biofilm against methanogenic activity. Overall, these results confirm

that the optimized conditions identified in the small-scale Cylindrical-MECs (pH 8 and +0.4 V) are effective at the reactor scale, demonstrating their suitability for MEC scale-up.

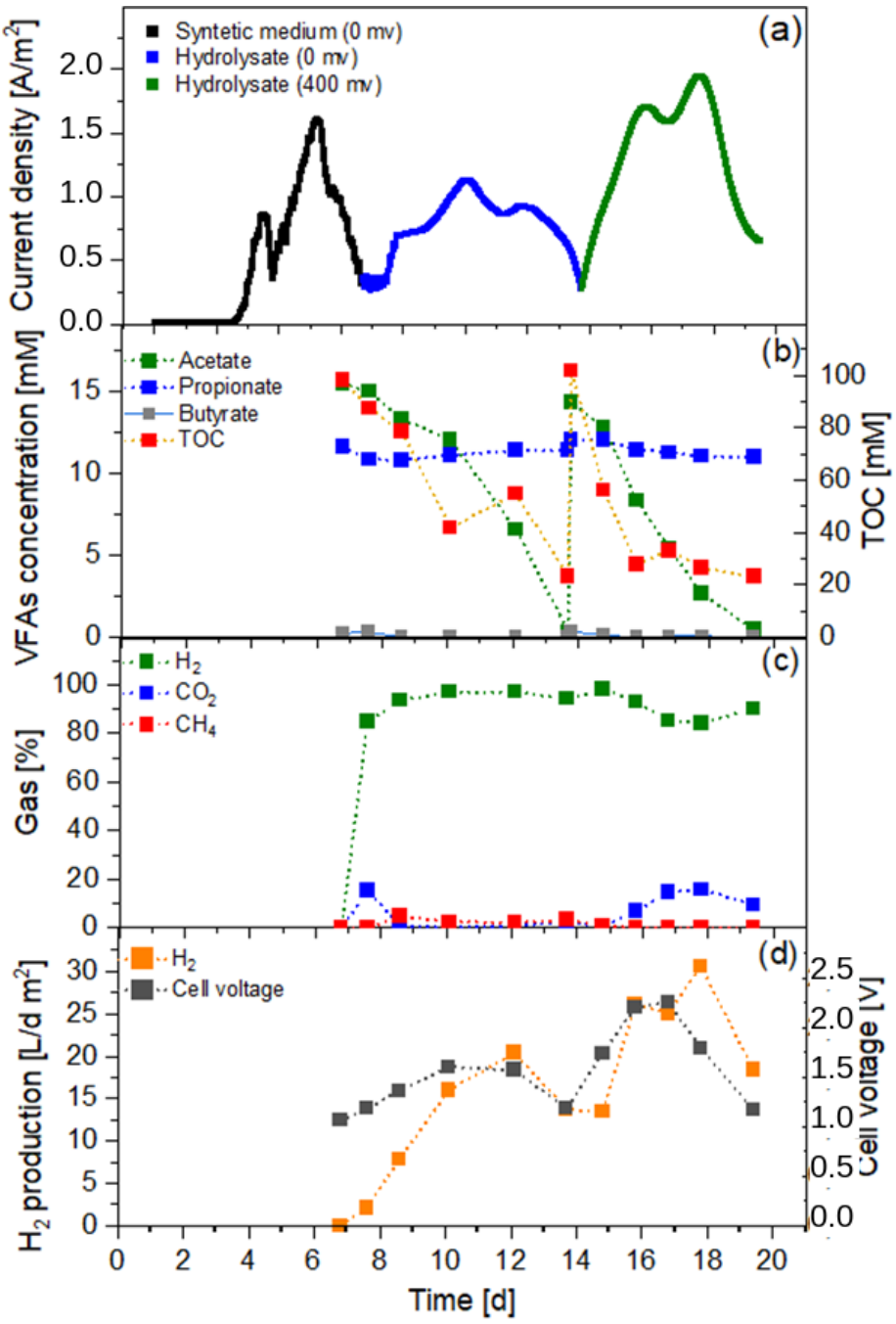

Figure 28. Effect of applied anodic potential on the performance of a 10 L rotating disk bioelectrochemical reactor (RDBER). (a) Current density under two applied potentials: 0 V vs. SHE with synthetic medium (black) and hydrolysate (blue), and 0.4 V vs. SHE with hydrolysate (green), (b) Acetate and total organic carbon (TOC) concentrations, (c) Gas composition (% H_2, CO_2, CH_4), (d) hydrogen production rate and cell voltage over time.

To evaluate the energy efficiency of the RDBER in relation to hydrogen production, electrochemical and energy efficiency metrics were calculated in relation to the applied anodic potential. These analyses were performed to determine not only the volumetric productivity of hydrogen but also how effectively the supplied electrical energy was converted into chemical energy in the form of H_2, providing a more comprehensive assessment of system performance and scalability.

As shown in Figure 32d, applying an anodic potential of +0.4 V increased the maximum cell voltage from 1.57 V (at 0 V) to 2.25 V. This rise in cell voltage was accompanied by higher hydrogen productivity, with maximum hydrogen evolution observed at the highest applied potential. At an applied potential of +0.4 V, hydrogen production was about 50% higher than at 0 V, demonstrating improved electrochemical efficiency under the higher potential condition. However, efficiency analysis showed that higher hydrogen production did not result in better energy efficiency (Figure 33). The hydrogen energy efficiency (η_{H_2}), defined as the ratio of the energy content of produced hydrogen to the electrical energy input, was higher at 0 V (83.7%) than at +0.4 V (59%). This indicates that although less hydrogen was produced at 0 V, the supplied energy was used more efficiently. The cathodic hydrogen recovery ($\eta_{cat,\ H_2}$) was also slightly higher at 0 V (88.5%) than at +0.4 V (81%), suggesting that a portion of the electrons at the higher potential may have been directed toward non-hydrogen-producing pathways.

In contrast, CE increased with applied anodic potential, showing that a greater proportion of electrons from substrate oxidation were captured as current at 0.4 V. Nevertheless, the difference between CE and hydrogen-based efficiencies indicates that not all electrons contributing to the current were ultimately reflected in the measured hydrogen output. This was

further supported by the hydrogen yield normalized to energy input (Figure 29), which was higher at 0 V (0.03 kg H_2/kWh) than at 0.4 V (0.02 kg H_2/kWh).

Overall, applying a higher anodic potential of +0.4 V increased hydrogen production and electron recovery from the substrate but reduced overall energy efficiency compared with 0 V. These results show a trade-off between achieving higher hydrogen output and maintaining energy efficiency during the scale-up of MEC systems.

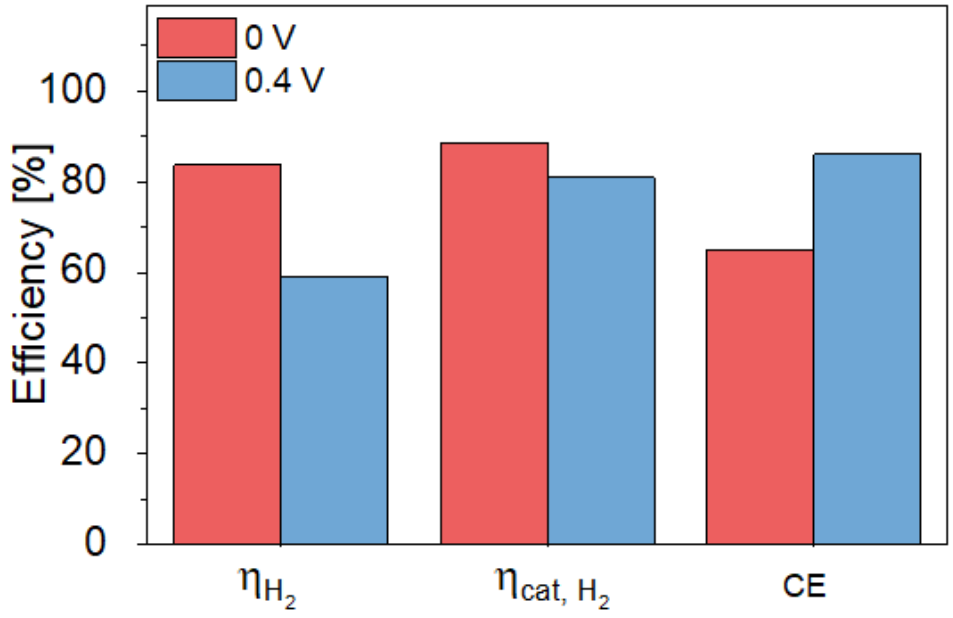

Figure 29. Influence of applied anodic potential (0 V and 0.4 V vs. SHE) on efficiency parameters in the 10 L rotating disc bioelectrochemical reactor (RDBER). Presented are hydrogen energy efficiency (η_{H_2}), calculated as the ratio of the energy content of produced H_2 to the electrical energy input; cathodic hydrogen recovery ($\eta_{cat,\ H_2}$), representing the fraction of electrons recovered as hydrogen; and TOC-based Coulombic efficiency (CE), reflecting electron recovery from substrate oxidation.

To complement the electrochemical and energetic analysis, the economic performance of the RDBER was also evaluated. This part of the study was carried out to determine whether increased hydrogen productivity at higher anodic potential could balance the additional energy input when considered from an economic perspective. Two key indicators were assessed:

hydrogen yield normalized to energy input ($Y_{H_2/E}$) and net economic gain from hydrogen production.

As shown in Figure 30**,** $Y_{H_2/E}$ was higher at 0 V, reaching 0.03 kg H_2/kWh**,** compared with 0.02 kg H_2/kWh at +0.4 V**.** This confirms that hydrogen generation was more energy-efficient at the lower applied potential. In contrast, the net economic gain, calculated based on the electricity consumption cost**,** remained nearly identical under both conditions, with values of 4.02 and 4.01 €/kg H_2 at 0 V and +0.4 V**,** respectively. This indicates that although the system consumed more energy at +0.4 V, the additional hydrogen produced compensated for the higher energy demand, resulting in similar overall economic performance for both operating conditions.

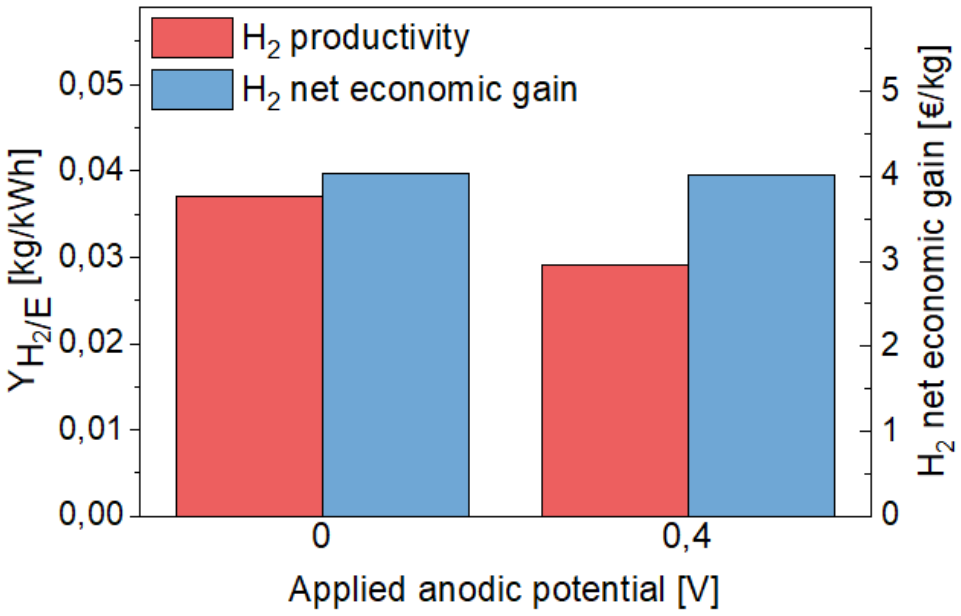

Figure 30. Influence of applied anodic potential (0 V and 0.4 V vs. SHE) on hydrogen yield normalized to energy input ($Y_{H_2/E}$, kg H_2/kWh) and net economic gain (€/kg H_2) in the 10 L rotating disc bioelectrochemical reactor (RDBER).

These results show a trade-off between energy efficiency and productivity. Operation at 0 V was more favorable for energy efficiency, while operation at +0.4 V provided higher hydrogen

output without a significant economic benefit over lower potential. Therefore, the choice between the two conditions depends on whether the priority is energy efficiency or hydrogen production.

3.7. Bioelectrochemical H_2 for acetoin production

The autotrophic growth of the engineered *C. necator* H16 strain was tested using a 1 L gas mixture supplied by the RDBER, which was then supplemented with oxygen and additional CO_2 to end up with the composition of $H_2/CO_2/O_2$ (73:12:15%). This gas composition adjustment was according to the optimum ratio reported by Weiler et al. (2024). This approach was considered to evaluate whether the hydrogen-rich gas produced under optimized electrochemical conditions could directly support microbial growth and product formation. The acetoin accumulation was used as an indicator of gas utilization and metabolic activity.

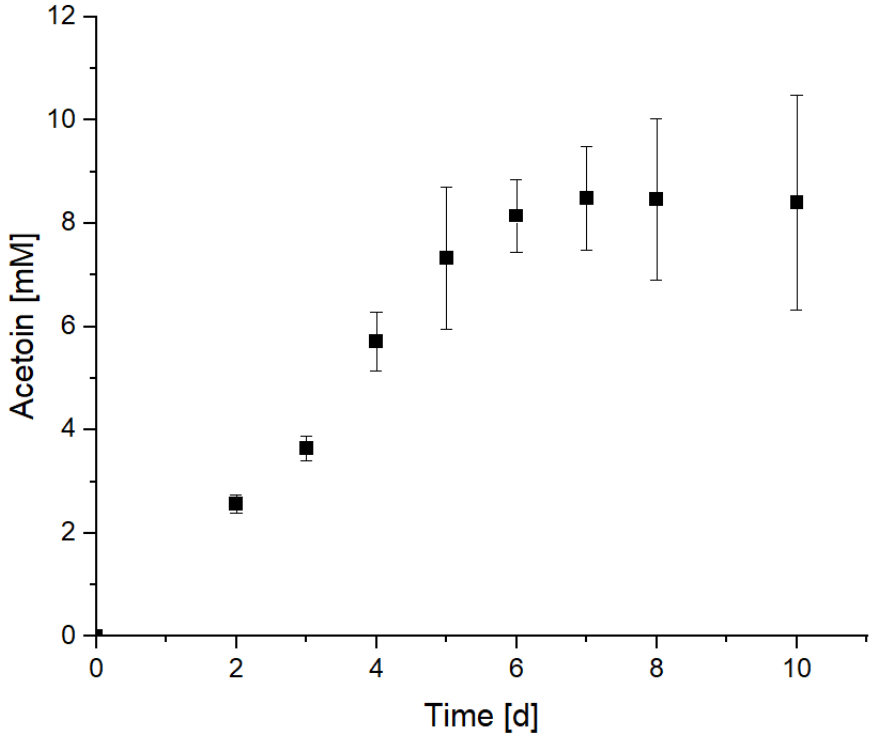

Figure 31. Acetoin production by the engineered strain of *C. necator* H16 (pBBR1_*alsSD*) cultivated autotrophically with the RDBER-derived gas mixture.

As shown in Figure 31, acetoin concentrations increased steadily over the 7 days of cultivation, reaching 8.5 mM by day 7, and then remained at a similar level until day 10. The steady increase confirmed that the cells grew autotrophically, utilizing CO_2 as the carbon source and H_2 as the electron donor. The total gas supplied (1.08 L; 43.5 mmol, calculated using the ideal gas law at 25 °C and 1 atm) corresponded to 31.8 mmol H_2, 5.22 mmol CO_2, and 6.53 mmol O_2. Based on the stoichiometry of acetoin formation (4 CO_2 and 10 H_2 per mol acetoin), the 0.85 mmol acetoin formed in the 100 mL culture corresponds to a minimum of 3.40 mmol CO_2 fixed into product and 8.50 mmol H_2 for product synthesis. Relative to the gas fed, this means 65.1% and 26.8% of the supplied CO_2 and H_2 ended up in acetoin.

These results show that the hydrogen-rich gas produced by the RDBER under optimized electrochemical conditions effectively supported autotrophic growth and targeted product formation.

4. Discussion

The increasing global demand for clean energy has accelerated the development of renewable technologies aimed at reducing dependence on fossil fuels and contributing to sustainable energy production. Among potential energy sources, hydrogen is considered highly promising due to its high energy density, clean combustion, and broad environmental and economic advantages (Shen et al., 2016; Yun et al., 2021).

MECs offer the advantage of producing hydrogen while simultaneously treating wastewater by removing organic and inorganic pollutants (Cusick et al., 2010; Hu et al., 2009). However, despite major advances in MECs research, their practical application remains limited. This is mainly due to the lack of studies under industrial-scale conditions, particularly those using complex wastewaters. Scaling up MECs introduces operational and biological challenges that can significantly reduce system efficiency (Baeza et al., 2017; Cusick et al., 2011; Escapa et al., 2015; Guerrero-Sodric et al., 2023). Real feedstocks, such as hydrolysate from dark fermentation, are rich in organic acids and readily available but pose several challenges. Their variable composition, nutrient imbalance, and potential inhibitory compounds (e.g., ammonia, sulfides, heavy metals) can negatively affect MEC performance and stability. Moreover, the limited understanding of microbial community behavior under such complex conditions makes it difficult to optimize system operation and reliably predict large-scale performance.

Advancing MEC technology for real-world application requires a mechanistic understanding of how operational parameters influence system performance under complex substrate conditions. In this thesis, a systematic investigation was carried out to evaluate the effects of flow velocity (with synthetic medium), substrate concentration, pH, and applied anodic potential on the performance of membraneless MECs operated with real hydrolysate obtained from primary sludge fermentation. This thesis aimed to elucidate biofilm structure and

metabolic function at the molecular level, suppress competing microbial pathways, enhance electroactive bacterial performance, and optimize hydrogen production toward scalable MEC operation. Furthermore, a techno-economic analysis was performed to assess the process feasibility and to elucidate the relationship between energy input and overall system efficiency. The produced hydrogen was further evaluated for its potential application not only as a sustainable energy carrier but also as a feedstock for the biosynthesis of value-added biochemicals.

4.1. Flow velocity–mediated modulation of anodic biofilm in MECs

4.1.1. Impacts on anodic biofilm development and electroactivity

Our findings demonstrate that flow velocity plays a crucial role in determining the balance between biofilm structure and electrochemical performance in *S. oneidensis* and *G. sulfurreducens* cocultures. The lower flow velocity (0.2 mm/s) resulted in more porous biofilm structures that, despite exhibiting greater overall biovolume, generated lower current densities. A thick electroactive biofilm can reduce current output due to diffusion limitations and the formation of inactive biomass. This aligns with findings by Netsch et al. (2025b), who reported higher biofilm thickness (40 µm vs 12 µm) and porosity (55% vs 25%) at a lower flow velocity (9 cm/s vs 27 cm/s) in mixed-species biofilms. Complemented this, Netsch et al. (2025a) observed that current density decreased when the mixed-species biofilm thickness exceeded 100–150 µm in an MEC flow cell operated at 0.5 cm/s.

Conversely, the higher flow velocity (0.8 mm/s) produced thinner and denser biofilm architectures that catalyzed significantly higher current densities. Under higher flow velocity, increased shear stress creates a constant risk of detachment. To withstand these conditions, cells adopt a strategy that minimizes detachment by forming denser biofilms and adhering more tightly to the surface, resulting in compact, shear-resistant structures that help maintain an

active basal layer (Paul et al., 2012; Wang et al., 2022b). Such adaptation seems to enhance cross-feeding and metabolic cooperation within the coculture of strongly attached electroactive cells. A thinner biofilm likely reduces diffusion limitations for acetate, flavins, protons, and other metabolites within the biofilm, facilitating metabolite and electron exchange between the two species (Jones and Buie, 2019), while excessive porosity might increase the separation between these two microorganisms and from the electrode (Pham et al., 2008; Yang et al., 2019).

These observations raised the question of whether the effect of flow velocity on biofilm structure is purely mechanical or whether higher flow velocities additionally trigger biological adaptations that alter cellular regulatory mechanisms governing biofilm formation.

The bioelectrochemical performance of *G. sulfurreducens* under the same flow velocities (0.2 and 0.8 mm/s) showed minimal sensitivity to changes in flow velocity. This indicates that *G. sulfurreducens* biofilms follow an intrinsic structural development mechanism that remains unaffected by the flow velocities tested in this study. The results are also in line with the findings of Jones (2018), which showed no significant changes in biofilm thickness and surface roughness for *G. sulfurreducens* at shear stresses of 0.01 and 1 Pa. Although *G. sulfurreducens* is known for its robust biofilm structure, the findings suggest that it can be affected when its growth depends on an additional species such as *S. oneidensis*. Consequently, the interaction between *S. oneidensis* and *G. sulfurreducens* appears to modulate biofilm architecture and, as a result, electrochemical performance.

4.1.2. Impacts on biofilm resilience and functional shifts

If modulation of biofilm chemistry occurs in response to flow conditions, leading to different biofilm characteristics, this difference should be longer-lasting and not easily reversible by changes in flow velocity.

When the flow velocity was reduced from 0.8 to 0.2 mm/s on day 4, only limited changes in current density, biovolume, and porosity were observed, indicating that biofilms established under higher flow are functionally resilient. Moreover, the persistent structure and functionality of the two-species biofilm after a switch in flow velocity pointed toward a regulatory program changing biofilm matrix composition rather than toward solely flow-rate-dependent compression of the biofilm. Nevertheless, it was also possible that the four-day time frame after the flow velocity switch was insufficient for biofilm rearrangements to occur.

Increasing the flow velocity from 0.2 to 0.8 mm /s led to a decrease in biovolume and porosity but an increase in current density compared to biofilms maintained under constant low flow. The results show that experimental duration was clearly sufficient to cause a change in biofilm structure and functionality. Within four days, both biofilm characteristics began to diverge progressively, with lower porosity and higher current density emerging as hallmarks of biofilms after the switch to a higher flow velocity.

4.1.3. Impacts on the transcriptional response

The transcriptomic analysis was performed on co-culture biofilms cultivated at constant flow velocities of 0.2 and 0.8 mm/s, showing that while *G. sulfurreducens* kept having the by far dominant relative gene expressions across hydrodynamic velocities, *S. oneidensis* expressions had more relative sensitivity to flow dynamics and increased when increasing flow velocity, suggesting that transcriptional regulation by this species plays a key role in the observed flow-

dependent biofilm behavior. The increased relative gene expressions of *S. oneidensis* at higher flow velocity (0.8 mm/s) likely support an induced adaptive regulatory response, either to shear force or to an increased metabolic rate resulting from lower mass transfer limitation as previously suggested by Jones and Buie (2019).

The majority of differential expression between biofilms grown under 0.2 mm/s and 0.8 mm/s, belonging to *S. oneidensis*, which again emphasizes the stronger transcriptional response of *S. oneidensis* to increases in flow conditions during the early stages of biofilm development.

Among the top differentially expressed genes, SO_4323 (*bpfD*) exhibited opposite transcriptional responses to flow velocity. To understand the potential contribution of the regulations of this gene, it was previously discussed that lower levels of intracellular c-di-GMP levels (Matsumoto et al., 2021), which then induces only partial binding of BpfD and incomplete interaction with BpfG**.** Under these conditions, BpfG is expected to remain proteolytically active, leading to BpfA cleavage and partial biofilm dispersal (Zhou et al., 2015). This likely explains the reduced biovolume and the formation of thinner, denser biofilms observed under high flow velocity. Dense biofilms are beneficial at high-shear stress, providing higher flow resistance and mechanical stability.

Overall, it was hypothesized that the coordinated regulation of *bpfD* and *dgc* likely contributes to the change in biofilm structure and efficiency, particularly the *S. oneidensis* fraction, in response to flow velocity, thereby optimizing the co-culture biofilm performance. c-di-GMP signaling is likely involved, given its association with the regulation of these two genes. Confirming this hypothesis still requires quantifying intracellular c-di-GMP levels and assessing Bpf system activity to link gene expression with phenotype directly.

4.1.4. Interplay between gene functions and the mechanosensing pathway

To study the potential contribution of *bpfD* on biofilm structure/efficiency, a mutant strain (MR-1 Δ*bpfD*) was constructed. Its biofilm formation and bioelectrochemical responses were compared with those of the wild type under flow transitions (0.8 → 0.2 mm/s and 0.2 → 0.8 mm/s).

Higher biovolume and porosity as well as lower current density were observed in the co-culture with the mutant compared to the wild type following the flow velocity decrease from 0.8 to 0.2 mm/s. Based on the transcriptomic findings and the observed upregulation of this gene, along with its associated effects on biofilm thickness, inactivation of *bpfD* was expected to promote biofilm formation, consistent with the higher biovolume observed in the mutant coculture. However, the greater biovolume, coupled with higher porosity, may also cause diffusional limitations and reduce the efficiency of electron transfer (Häuser et al., 2022). Although the EPS content of the biofilm was not evaluated, the very low current density associated with MR-1 Δ*bpfD* could be explained by having excessive increase in EPS fraction in the biofilm matrix. This overproduction likely represents a protective response to stress conditions (Shen et al., 2013) and, additionally, reflects the role of *bpfD* in c-di-GMP–related regulatory pathways, where its inactivation disrupts normal signaling balance and promotes EPS synthesis rather than the formation of a structured, conductive biofilm under shear stress. This observation is consistent with the study by Kitayama et al. (2017), who found that more EPS and a higher EPS-to-protein ratio reduced the electroactivity of *Shewanella* biofilms in electrochemical flow cells. Excessive EPS, particularly if it is less conductive, may interfere with cell–cell and cell–electrode interactions, limiting nutrient and acetate diffusion to deeper layers that are mostly dominated by *G. sulfurreducens* (E. Klein et al., 2024). Gao et al. (2019) also found in their study that the exopolysaccharides of the EPS layer substantially inhibit EET

processes by increasing charge transfer resistance and decreasing the biofilm conductivity of *S. oneidensis*. Increased porosity likely reduces biofilm conductivity by weakening cell–cell and matrix connectivity, thereby hindering electron transfer within the biofilm. These results indicate that the *bpfD* mutation affects biofilm architecture in a way that limits the current generation. Our findings complement those of Klein et al. (2024), which showed that overexpression of *bpfA* and *bpfG* in *S. oneidensis* positively affected current density, even though the resulting biofilm was too thin to be observed by OCT.

In flow transition from 0.2 to 0.8 mm/s despite the comparable biovolume, the co-culture with the *bpfD* mutant exhibited lower current production, likely reflecting structural and functional differences within the biofilm. The increased porosity in the mutant, together with the likely overproduction of carbohydrate-rich and therefore less conductive EPS, may reduce the conductivity of the biofilm matrix and increase the spatial separation between cells, thereby limiting electron transfer efficiency within the coculture. Comparison of the data obtained at 0.2 and 0.8 mm/s indicates that the negative effects of *bpfD* inactivation on biofilm structure and current output were more pronounced when the coculture developed under the higher initial flow velocity and corresponding shear stress in Phase 1. This suggests that elevated shear intensifies the impact of *bpfD* inactivation, highlighting the role of this gene in regulating biofilm response to mechanical stress.

4.2. Efficiency of MECs with hydrolysate as substrate

4.2.1. Role of hydrolysate concentration

Hydrolysate concentration strongly influences MEC performance by affecting both electrochemical activity and microbial community behavior. The current density results showed an optimum at 40% hydrolysate, while lower values were recorded at 20% and 60%.

At 20% hydrolysate, the low current density was most probably due to limited substrate availability and low solution conductivity (1.75 mS/cm). Reduced conductivity increases internal resistance and decreases electron transfer efficiency, consistent with previous studies showing a positive relationship between conductivity and power output in BESs (Liu et al., 2005). Although VFAs, especially acetate, were still consumed under these conditions, the high abundance of *Azospira*, a genus known to utilize VFAs (Becerril-Varela et al., 2021), indicates that substrate consumption did not necessarily result in efficient electron transfer. This aligns with previous findings showing that *Azospira* is not directly involved in extracellular electron transfer (Koch and Harnisch, 2016; Xiao et al., 2015).

At 40% hydrolysate, the system achieved the highest current density and CE, particularly the TOC-based CE. The microbial community composition helps explain this performance. A balanced consortium of fermentative bacteria (*Petrimonas, Macellibacteroides, Proteiniphilum*) and exoelectrogens (*Geobacter*) likely enabled efficient conversion of hydrolysate into VFAs and effective electron transfer to the anode (Board, 2015; Cardeña et al., 2019; Feng et al., 2023). This cooperative interaction between fermentative bacteria and exoelectrogens, also reported in previous studies (Ullah and Zeshan, 2020), supports the idea that optimal substrate availability enhances VFA conversion and current generation.

At 60% hydrolysate, system performance decreased even though VFA and TOC removal rates were higher. This is likely due to the higher substrate concentration, including various C-sources, which increases the microbial diversity, particularly in the planktonic phase, towards competing microbial pathways such as methanogenesis and/or sulfate reduction. By this, less carbon remains available for exoelectrogens within the anodic biofilm. A supporting observation was the increase in relative abundance of sulfate-reducing bacteria (i.e., *Solidesulfovibrio*) and the potential denitrifying *Azospira* was observed. Both genera can

oxidize VFAs through non-electrogenic pathways (Sun et al., 2022), thereby diverting electrons away from the anode and reducing overall electrochemical efficiency. A similar observation was reported by Darus (2011), who showed that decreasing the acetate concentration from 15 to 5 mM increased the CE from 50% to 75.3% by limiting the acetate available to acetoclastic methanogens.

The decrease in CE at high substrate loading indicates inefficient electron recovery despite higher organic removal. Excessive organic loading may alter interactions between hydrolysate components and the electrode surface. While increased organics can promote biofilm growth, they may also lead to electrode fouling and mass transfer limitations, reducing effective electron transfer to the anode (Wijeyekoon et al., 2004). Similar trade-offs between substrate concentration, microbial competition, and electron recovery have been reported in overloaded BESs (Sleutels et al., 2016; Ullah and Zeshan, 2020).

Acetate showed the highest removal rates under all conditions, confirming its role as the preferred substrate for exoelectrogenic oxidation. In contrast, butyrate removal remained low, likely due to its limited bioavailability and the reduced capacity of the community for chain elongation or syntrophic metabolism under the tested conditions (Choi et al., 2023; Elreedy et al., 2024). The difference between VFA-based and TOC-based CE indicates that, although VFAs were efficiently consumed, not all electrons were recovered as current, particularly at higher hydrolysate concentrations, where alternative metabolic pathways were more active.

4.2.2. Role of pH

The results show that pH strongly influences both the electrochemical performance and microbial activity in MECs. Within the tested pH range (5–8), current density and CE were

highly sensitive to pH, with performance improving as conditions shifted from acidic to near-alkaline.

At pH 5–6, acetate and TOC removal remained relatively high, but the current generation was very low. The accumulation of propionate at pH 5–5.5 suggested that its oxidation pathways were inhibited. Microbial community analysis supported this observation, showing an enrichment of fermentative bacteria such as *Petrimonas*, *Sedimentibacter*, and *Macellibacteroides*, together with methanogens (*Methanosarcina*) and VFA-utilizing bacteria like *Azospira* under acidic conditions. At the same time, electroactive bacteria such as *Geobacter* were present in low abundance. This imbalance likely caused electrons to be redirected toward non-electrogenic pathways, consistent with the low CE observed. In addition, microbial biofilms may have buffered local pH, creating near-neutral microenvironments that allowed limited metabolic activity to continue (Tran et al., 2024). Acidic conditions are also known to increase redox potential and promote proton accumulation, which hinders electron flow and suppresses EET (Kilicaslan et al., 2024). These outcomes align with previous reports that *Geobacter*-dominated biofilms are sensitive to moderately acidic environments, with significantly reduced activity below pH 6.5 (Dhar et al., 2017).

At neutral pH (7), system performance improved markedly. Both current density and CE increased, accompanied by a distinct shift in microbial composition. The relative abundance of *Geobacter* rose, while fermentative bacteria and methanogens declined. Although archaeal abundance was slightly higher than at pH 8, bacteria still accounted for more than 90% of the community, creating conditions more favorable for electrogenic activity. This demonstrates that under the tested conditions, neutral pH promoted a more effective balance between fermentative VFA conversion and exoelectrogenic electron transfer.

The highest performance was observed at pH 8. At this pH, *Geobacter* dominated the anodic biofilm (44% relative abundance), while methanogens were strongly suppressed, consistent with their reported alkaline sensitivity (Ma et al., 2024). The dominance of *Geobacter* at higher pH confirms that these bacteria are well adapted to moderately alkaline environments, where their multi-heme c-type cytochromes involved in EET operate most efficiently (Srivastava et al., 2024). These findings are in agreement with previous studies reporting that neutral-to-alkaline pH enhances electrogenic activity (Halim et al., 2021). These findings show that hydrolysate-fed MECs perform best at pH 7–8, where electron recovery is maximized and methanogenesis is effectively suppressed. Similarly, Sun et al. (2019) reported that the initial pH strongly affects anodic biofilm development and overall system performance. The highest efficiency was achieved at pH 8, with a CE of 46.4%, whereas acidic conditions (pH 5–6) resulted in low current generation. Although higher pH values were not examined in this study, exoelectrogens generally perform best near neutral pH (Li, 2018). Therefore, reduced efficiency would be expected under more alkaline conditions due to diminished microbial activity. However, confirming this assumption would require additional investigations. Cui et al. (2019) showed that operating MECs under alkaline conditions (pH 8.5–11.2) increased current density and hydrogen recovery, mainly due to the suppression of methanogenesis. Similarly, Choi et al. (2023) reported that acidic anodic conditions led to a strong decrease in current density and electron recovery in MECs fed with VFA mixtures, while neutral to alkaline pH promoted higher electrogenic activity.

4.2.3. Role of applied potential

The results show that the applied anodic potential strongly influences MEC performance. The current density increased by more than 42-fold from 0.08 to 3.42 A/m^2, indicating enhanced electrochemical activity under more positive redox conditions. Electron recovery showed a

similar pattern; TOC-based CE rose by more than 16-fold from 2.29 to 38 %, while VFA-based CE increased by over 12-fold from 7.69 to 95.76 %, approaching nearly complete electron capture. Substrate removal was likewise enhanced across the same potential range. These sharp increases highlight how higher anodic potentials establish more favorable redox conditions, simultaneously accelerating microbial oxidation of complex substrates and facilitating electron transfer to the electrode. Together, these results confirm that anodic potential directly governs both microbial metabolism and electron recovery efficiency. At negative potentials (–0.2 V), system performance was strongly constrained, with low current density, poor CE, and limited VFA degradation. Microbial community analysis revealed that this corresponded to a high relative abundance of hydrogenotrophic methanogens (*Methanobacterium*), which likely diverted electrons toward methane production rather than to the electrode. The enrichment of fermentative taxa such as *Sedimentibacter* and *Bacteroidales_g* further indicates that substrate breakdown occurred mainly via acidogenesis, without effective electron transfer. The low abundance of *Geobacter* under these conditions limited direct electron transfer to the anode, resulting in weak electrochemical performance. Under such unfavorable redox conditions, non-electrogenic pathways became dominant, leading to low energy recovery despite continued organic matter removal.

When the applied potential was increased to 0 and +0.2 V, system performance and the microbial community shifted toward conditions more favorable for electrogenesis. Current density rose compared with –0.2 V, along with higher CE and improved acetate and propionate removal. The enrichment of exoelectrogens such as *Geobacter* under these conditions shows that positive anodic potentials favor microorganisms capable of direct electron transfer. At the same time, the decline in methanogen abundance suggests that higher redox potentials suppress archaeal activity and reduce competition for electrons. Propionate degradation was highest at 0–0.2 V but declined slightly at +0.4 V. This suggests that microbial groups responsible for

syntrophic propionate oxidation were less competitive under strongly oxidative conditions, or that pathways using propionate for non-electrogenic metabolism were less active.

At higher anodic potentials, the anode serves as a stronger electron acceptor, reducing the energy barrier for electron transfer from microbial redox proteins such as multi-heme c-type cytochromes and conductive pili, which enhances electron flow to the electrode (Li et al., 2025). This thermodynamic advantage explains the strong increase in current density and CE when the potential was raised from –0.2 V to +0.4 V. Higher potentials also enhance electron transfer kinetics by providing a greater driving force for redox reactions at the biofilm–electrode interface (R. C. Wagner et al., 2010). A study by Grobbler et al. (2018) showed that applying more positive anodic potentials increased current density and reduced start-up time by promoting the expression of key EET proteins and elongation factors related to protein synthesis. At the metabolic level, higher potentials activate NADH-dependent pathways, stimulate branching in the tricarboxylic acid (TCA) cycle, and upregulate expression of metabolic genes (Grobbler et al., 2015; Hirose et al., 2018; Song et al., 2016), although excessively high potentials may deactivate the TCA cycle and disrupt cellular energy metabolism (Matsuda et al., 2013).

The best performance was achieved at +0.4 V, where current density, CE, and substrate removal reached their highest values. At this potential, *Geobacter* dominated the anodic biofilm, while methanogens and sulfate-reducing bacteria such as *Solidesulfovibrio* were largely suppressed. This indicates that exoelectrogens have a selective advantage under strongly oxidative conditions, where transferring electrons to the anode provides the greatest energetic benefit. The high VFA-based CE also shows that the microbial community was closely linked to the electrode, allowing efficient EET and minimal electron losses to competing pathways.

The multivariate analyses conducted in this thesis further highlight the dominant role of pH and anodic potential in shaping MEC performance and anodic microbial ecology. PCA revealed that the first two principal components explained 75.2% of the total variance among performance indicators, underscoring the robustness of the model. Variations induced by acidic pH (<7.0) and changes in anodic potential (–0.2 to +0.4 V) were the primary drivers of separation among samples, whereas hydrolysate concentration contributed less strongly. This pattern is consistent with our earlier results, where pH and anodic potential had the most pronounced effects on current density and CE. Importantly, strong positive correlations were observed between current density, CE, and anodic potential, confirming that anodic redox conditions were the main determinants of efficient electron transfer. Conversely, weak correlations of acetate, butyrate, and TOC removal with current density suggest the operation of competing carbon-utilization pathways, such as methanogenesis, which divert electrons away from the anode despite ongoing substrate degradation.

PCA of anodic microbial composition (68.3% variance explained by PC1 and PC2) provided additional mechanistic insight. While both anodic potential and hydrolysate concentration influenced community structure, their impact was secondary to that of pH. The strongest positive correlation was observed between *Geobacter* abundance and both anodic potential and pH, reinforcing the central role of this genus as the primary exoelectrogen under favorable electrochemical conditions. By contrast, *Geobacter* showed strong negative correlations with methanogenic archaea, particularly *Methanosarcina*, reflecting direct competition for carbon and electrons. The minor but positive correlation between *Geobacter* and *Methanobacterium* suggests the possibility of limited direct interspecies electron transfer (DIET), consistent with previous reports (Zheng et al., 2020). However, the marked increase in current density and CE at higher anodic potentials supports the conclusion that any DIET contribution remained minor relative to direct electron transfer to the anode.

The co-occurrence network analysis further highlighted the ecological interactions within the anodic biofilms. *Geobacter* emerged as the most functionally critical taxon, characterized by high abundance and predominantly negative associations with other genera, including *Azospira*, *Clostridium*, and *Petrimonas*. In particular, the strong negative correlation with *Azospira* indicates direct substrate competition, as this genus is known to oxidize a wide range of VFAs and has been repeatedly detected in BESs treating complex wastewater (Achenbach et al., 2001; Xiao et al., 2015; Xin and Qiu, 2021). Positive associations among fermentative and methanogenic taxa such as *Clostridium*, *Methanosarcina*, *Sedimentibacter*, and *Syntrophomonadaceae* are consistent with their cooperative roles in anaerobic degradation and methanogenesis (Yi et al., 2019). Network metrics, particularly closeness centrality, revealed that both *Geobacter* and these major competitors were highly connected, reflecting their central but counteracting roles in governing electron flux under the tested conditions.

4.3. Long-term stability and efficiency of a scaled-up MEC

4.3.1. Effect of pH on methanogenic and exoelectrogenic activity

pH proved to be a key factor influencing MEC efficiency and microbial stability under scale-up conditions. The initial enrichment of *G. sulfurreducens* at pH 7 under sterile conditions was highly beneficial, as it established an electroactive biofilm before the introduction of unsterile hydrolysate. This pre-enrichment gave exoelectrogens a competitive advantage at the anode, reducing early colonization by fermenters and methanogens and enabling efficient electron transfer with complex substrates. Similar strategies have been reported to improve start-up, reproducibility, and long-term stability (Logan et al., 2019), and these effects were confirmed in this study at this reactor scale.

After hydrolysate feeding began, the system operated stably at a pH of 7 for approximately 30 days before methane was detected. During this methanogen-free period, MEC performance

was strong, with current density closely linked to acetate and TOC removal, and hydrogen remaining the dominant gas product. These results show that exoelectrogens were mainly responsible for substrate oxidation, with electrons efficiently transferred to the anode and recovered as hydrogen instead of being diverted to competing pathways. This phase represented an efficient operating state, with optimal alignment between substrate use, electron recovery, and gas composition. Temporary increases in acetate and TOC were observed during this period. These fluctuations were likely caused by the hydrolysis and fermentation of complex organics in the hydrolysate, which produced soluble intermediates faster than the exoelectrogenic biofilm could oxidize them. Such imbalances between fermentative release and anodic consumption are common in complex-substrate MECs and reflect the dynamic interplay between primary fermenters and exoelectrogens within the biofilm (Hodgson et al., 2016). The continued dominance of hydrogen production and stable current generation during this period indicates that exoelectrogenic metabolism remained predominant, maintaining system efficiency until methanogens eventually appeared.

The decline in current density after day 37, despite continued decreases in acetate and TOC, suggests that methanogenesis began to outcompete exoelectrogenic activity. This shift likely diverted substrate from the electroactive organism toward methanogens, reducing electron recovery. The sustained low current density following acetate addition on day 47 further indicates that methanogens had established in the microbial community, limiting the system's ability to recover and resume efficient electrochemical performance. To suppress methanogenic activity, the pH was sequentially lowered to 6 and then to 5. However, methane production persisted, while current density declined further. This suggests that acidification had a stronger inhibitory effect on exoelectrogens than on methanogens. Lowering the pH to 5–6 was not an effective strategy for controlling methanogenesis, as it failed to suppress methanogen activity and significantly impaired electrochemical performance. This is in

contrast with findings by Qiu et al. (2023) and Sun et al. (2020), who observed strong inhibition of methanogenesis at similar pH levels. This discrepancy is likely due to buffering effects within the biofilms in this study, which created localized pH microenvironments that remained near-neutral, allowing methanogens to persist. Under acidic conditions, reduced exoelectrogenic activity likely limited hydrogen availability and thereby suppressed hydrogenotrophic methanogenesis, while acetoclastic methanogenesis became dominant, as indicated by continued substrate consumption (Jin et al., 2022; Lu et al., 2011). Since acidification failed to suppress methanogenesis, the pH was increased to 11 to test whether strong alkalinity could restore hydrogen production. This adjustment completely stopped the current generation, indicating severe inhibition of exoelectrogens such as *Geobacter*, which are highly sensitive to high pH. Even after the pH was restored to 8, current did not recover, confirming that extreme alkalinity had permanently damaged the anodic biofilm and disrupted electron transfer. After reinoculating with *G. sulfurreducens* and adding acetate, current production restarted at pH 8, and methane stayed low for about 20 days. During this recovery phase, acetate and TOC removal matched the increase in current, and hydrogen was again the main gas, similar to the early stage before methanogens appeared. At pH 8, both current density and hydrogen production reached their highest levels, confirming that pH 8 is more favorable than pH 7. This aligns with previous findings from Cylindrical-MEC systems. Some studies have reported improved MEC performance under highly alkaline conditions. For example, Cui et al. (2019) observed high current density (83.7 A/m³) and hydrogen recovery (85–90%) at pH 11.2, along with strong suppression of methanogens. However, in this study, operating at pH 11 led to a sharp decline in exoelectrogen activity and current generation, despite partial inhibition of methanogenesis. This contrast may be explained by differences in microbial community structure, biofilm maturity, or the type of substrate used. It is important to note that, since the experiment was stopped after 20 days at pH 8, it remains uncertain how long this pH

can effectively suppress methanogenic activity. Longer-term experiments are needed to confirm the sustained positive effect of this pH on MEC performance.

4.3.2. Effect of applied anodic potential on hydrogen yield and energy efficiency

The applied anodic potential had a strong effect on RDBER performance. At 0 V, current density increased gradually along with acetate and TOC removal. When the potential was raised to +0.4 V, the rise in current density was faster, accompanied by more rapid substrate consumption. These results show that a higher anodic potential improves electron transfer and stimulates microbial activity, strengthening the connection between substrate oxidation and current generation. The VFA profile showed that acetate was the main substrate supporting current generation, while propionate and butyrate remained largely undegraded. This is likely because *Geobacter* species, the dominant exoelectrogens in the system, preferentially use acetate as their primary electron donor. In contrast, propionate and butyrate require additional syntrophic microorganisms or conversion steps, which were less active under these conditions (Speers and Reguera, 2012). As a result, acetate was the main driver of the current generation, while the other VFAs had minimal contribution.

Hydrogen was the main gas under both operating conditions, while methane remained negligible, indicating that slightly alkaline pH and optimized anodic potential effectively limited methanogenesis. These conditions supported stable exoelectrogenic communities, consistent with earlier Cylindrical-MEC results. Although long-term suppression cannot be confirmed, since methanogens previously appeared after 37 days, it is hypothesized that operation at pH 8 and +0.4 V may have delayed their growth and activity, contributing to more stable performance with minimal methane production. This is consistent with trends observed in Cylindrical-MEC systems, which showed higher CE and current production under similar conditions.

Compared with other MEC studies using real wastewaters at volumes of 10 L or greater, our system achieved comparable hydrogen production rates. Table 14 presents a comparison of membrane-less MEC studies from the literature. The comparison underscores the importance of optimizing multiple operational parameters to enable successful MEC scale-up. This study shows strong performance compared to previous reports. Most systems treating real wastewaters achieved lower hydrogen production rates (≤0.19 L H_2/ L d) and required higher applied voltages (0.8–1.1 V). The reactor design, featuring a short distance between the anode and cathode and a rotating disk configuration, likely contributed to the improved efficiency by reducing internal resistance and enhancing mass transfer. Moreover, the optimum operating conditions identified in this study further enhanced biofilm activity and hydrogen generation performance.

Table 14. Comparison of hydrogen production and operating parameters in single-chamber, membrane-less MECs (10 ≥ L)

	Reactor volume/mode	Substrate	Max H_2 production (L H_2 /L d)	Anode	Cathode	Anode surface area	Cathode surface area	Applied potential/cell voltage	Reference
1	1000 L/continues	Winery wastewater	0.19	Graphite fibre brushes	SS 304	7.2 m^2	18.1 m^2	0.9 V cell voltage	(Cusick et al., 2011)
2	88 L/ continues	Domestic wastewater	0.006	Carbon felt	Stainless steel wool	1.44 m^2	0.3 m^2	1.1 V cell voltage	(Heidrich et al., 2014)
3	40 L/ continues	Industrial wastewater	0. 025	Graphite felt+stainless steel mesh	Graphite felt+stainless steel mesh	0.47 m^2	0.43 m^2	0.8 V cell voltage	(Huang et al., 2022)
4	10 L/batch	Lignocellulosic hydrolysate	0.71	Carbon cloth	Carbon cloth+ titanium	0.6 m^2	0.6 m^2	1.36 V cell voltage	(Wang et al., 2021)
5	10 L/batch	Synthetic medium	5.9	Carbon cloth	Carbon cloth - molybdenum phosphide (MoP) catalyst	1 m^2	0.28 m^2	1.2 V cell voltage	(Singh et al., 2021)
6	10 L/ batch	Municipal wastewater	2.6	Carbon felt	Sigracet GDL 25 BC carbon paper	Not reported	0.3 m^2	0.9 V applied potential	(Gil-Carrera et al., 2013)
7	**10 L/batch**	**Municipal wastewater**	**0.76 (30.57 L-H_2/m^2·d)**	**Graphite plate**	**Mixed-metal-coated titanium plate**	**0.5 m^2**	**0.25 m^2**	**0.4 Applied potential**	**This thesis**

The evaluation of RDBER performance under different anodic potentials highlights the trade-offs between hydrogen productivity, energy efficiency, and economic viability during scale-up. Increasing the applied potential from 0 to +0.4 V enhanced maximum hydrogen production. This increase coincided with higher cell voltages, reflecting the stronger driving force for electron transfer and improved activity of electroactive biofilms. The CE observed at +0.4 V (86%) further suggests more effective electron recovery from the substrate in 0 V (65%). At higher anode potentials, electrogens become more active, consume more substrate, and transfer more electrons to the anode, leading to higher current densities. However, the increase in CE is smaller because not all of the additional substrate consumed is converted into current; part of it is still used for microbial growth or other non-electrogenic pathways. A similar trend was reported by Sleutels et al. (2011), where raising the anode potential from –0.45 to –0.25 V caused current density to increase more than sixfold, yet CE rose only modestly, from 9% to 21%.

A closer analysis of energy efficiency metrics highlights the limitations of operating at elevated anode potentials. Hydrogen energy efficiency (η_{H_2}) declined from 83.7% at 0 V to 59% at +0.4 V, showing that a larger fraction of the additional energy input was not captured as hydrogen. Cathodic hydrogen recovery ($\eta_{cat,\ H_2}$) also decreased slightly, from 88.5% to 81%, which may be linked primarily to physical hydrogen losses through gas leakage, as well as a portion of electrons diverted to biomass growth and biofilm metabolism (Speers and Reguera, 2012). In addition, hydrogen can itself be consumed by certain electroactive microorganisms such as *G. sulfurreducens*, which possesses uptake hydrogenases enabling hydrogen-dependent respiration (Brown et al., 2005). The normalized hydrogen yield dropped from 0.03 to 0.02 kg H_2/kWh as the voltage increased from 0 to 0.4 V, confirming that higher productivity came at the cost of energy efficiency. Although hydrogen output increased, overall energy return declined because a greater share of input energy was lost instead of being converted to H_2.

Laboratory studies have reported MEC yields ranging from 0.303 kg H_2/kWh under ideal conditions (0.123 V cell potential, 100% cathodic recovery) to about 0.022 kg H_2/kWh under practical conditions (1V, 60% recovery) (Jiang et al., 2023). In this study, operation at an applied anodic potential of 0 V achieved a yield of 0.03 kg H_2/kWh, better than what has usually been seen under real-world conditions.

From an economic standpoint, the production costs at 0 V and +0.4 V were nearly identical (4.02 and 4.01 €/kg H_2, respectively). This outcome suggests that the increased energy consumption at +0.4 V is effectively balanced by the corresponding rise in hydrogen output, resulting in stable cost performance across both conditions. These findings highlight a trade-off between energy efficiency and production capacity: operation at 0 V supports greater energy efficiency and aligns with sustainability goals, whereas +0.4 V offers a viable strategy when the primary objective is to maximize hydrogen yield without significantly impacting cost. It should be noted, however, that the techno-economic analysis presented here only accounts for the electricity cost. In practice, overall profitability will also depend on capital expenditure for reactors, electrodes, and membranes, as well as additional operational costs. Because MECs typically operate at low current densities, achieving competitive hydrogen output often requires larger electrode and membrane surface areas. This increases material demand, making the use of low-cost components essential for economic viability and large-scale commercialization (Park et al., 2022). Nevertheless, MECs offer unique economic benefits by integrating hydrogen production with wastewater treatment, significantly improving their competitiveness compared to conventional electrolysis (Jiang et al., 2023).

4.4. Integration of MEC-derived hydrogen into value-added biochemical production

Autotrophic growth of *C. necator* H16 produced 8.5 mM acetoin using a gas mixture of $H_2/CO_2/O_2$ (73/12/15% (v/v)), consistent with yields reported by Weiler et al. (2024). The production plateau observed after day 7 points to process bottlenecks, most plausibly gas–liquid mass-transfer limits, nutrient depletion, or product accumulation. About 65.1% of the supplied CO_2 and 26.8% of the supplied H_2 were captured as acetoin. These capture rates are not 100%, probably because a portion of the produced H_2 and CO_2 is consumed for microbial respiration and biomass synthesis. Additional losses also occur due to gas–liquid transfer limitations and off-gas emissions. More broadly, these results demonstrate the feasibility of directly coupling bioelectrochemical H_2 generation to biochemical synthesis.

MEC(RDBER)-derived H_2 thereby functions as an intermediate rather than an end product, enabling the production of higher-value chemicals while integrating CO_2 fixation and industrial biotechnology. Integrating H_2 produced by MEC into chemicals (e.g., acetoin, PHB (polyhydroxybutyrate), SCP (single cell protein), VFAs, CH_4) can be preferable to its use as a fuel because it captures CO_2 into higher-value products without the need to compress, liquefy, store, or transport H_2. This approach not only saves energy and reduces safety risks by using H_2 on-site but also offers a clear economic advantage. On-site conversion eliminates the costs of H_2 transport and storage while upgrading a low-value energy carrier into higher-value biochemicals (Sadhukhan et al., 2016). When H_2 is sourced from waste-treating MECs, the integrated process further recovers value from residues, improving overall process economics and strengthening the case for deploying such systems at scale (Kadier et al., 2020). Table 15 compares acetoin with other potential routes for H_2 integration.

Table 15. Overview of H_2 integration approaches in microbial bioprocesses

Product	H_2 integration pathway	Involved organism	Advantages	Limitations	Case study
CH_4	$H_2 + CO_2 \rightarrow CH_4$	Methanogens	Well-studied hydrogenotrophic consortia; single-component product	Strict anaerobic conditions; sensitive to pH, alkalinity, and impurities (H_2S/NH_3)	(Cristiani et al., 2023)
Medium-chain carboxylates (butyrate, caproate)	H_2 acts as a co-electron donor and supports chain elongation	Mixed-culture	Produces higher-value chemicals from waste streams; H_2 improves yields and thermodynamics; aligns with carbon recovery from VFAs	Requires co-substrates (e.g., ethanol); needs strict pH and gas-transfer control; product extraction is complex	(Baleeiro et al., 2021)
Acetate ($C_2H_3O_2^-$)	H_2 reduces CO_2 to acids	*Clostridium ljungdahlii*	Direct CO_2 fixation with high carbon selectivity	Sensitive to O_2; competition with methanogens; requires gas recirculation	(Boto et al., 2023)
Bioplastics (PHB/PHAs)	H_2 provides electrons and energy for CO_2 fixation and PHB synthesis	*C. necator*	High-value product; efficient use of carbon and energy	Requires efficient gas–liquid mixing; requires strict O_2/H_2 control; high gas-transfer demand; sensitive to H_2 purity (CO/H_2S inhibition)	(Zhang et al., 2022)
Acetoin	Autotrophic $H_2/CO_2/O_2$ gas fermentation	*C. necator* H16	CO_2 fixation; high carbon efficiency; less sensitive to CO; produces higher-value chemical intermediate	Requires efficient gas–liquid mixing; sensitive to H_2 purity; scale-up needs careful gas control	(Weiler et al., 2024), this thesis

4.5. Conclusion and outlook

MECs offer a promising method for converting organic waste into hydrogen with relatively low energy input. Their efficiency, however, is highly dependent on specific operational parameters that influence both electrochemical performance and microbial dynamics. This thesis systematically investigated how key operational variables influence biofilm structure and electroactivity, microbial interactions, and hydrogen production in MECs. Experiments across multiple reactor scales were used to identify conditions that maximize hydrogen yield and ensure system stability.

Hydrodynamic conditions play a critical role in biofilm development by influencing bacterial attachment, mass transport, and nutrient delivery. Flow velocity significantly influences the biofilm structure and electroactivity in *S. oneidensis*–*G. sulfurreducens* co-cultures, with distinct differences observed between the 0.2 mm/s and 0.8 mm/s flow velocities. At the same time, biofilms formed at the lower flow were thicker and more porous than biofilms at 0.8 mm/s, showing the strong influence of shear stress on biofilm structure and performance. The biofilm response to changes in flow velocity illustrates its structural adaptability, with the aim of optimizing metabolic activity and electrochemical performance under varying hydrodynamic conditions. Transcriptomic data indicate that *S. oneidensis* actively modulated its gene expression in response to flow velocity, whereas *G. sulfurreducens* exhibited comparatively stable transcriptional patterns. The pronounced and flow-dependent regulation of mechanosensing-related genes, such as *bpfD* (SO_4323), indicates that *S. oneidensis* was the primary driver of the transcriptional response to changing flow conditions. The reduced effects of this gene at biofilms initially developed at low flow velocities suggest that once an efficient basal layer is established, it sustains overall biofilm functionality and electrochemical efficiency under subsequent variations in shear stress.

These findings suggest that the biofilm response in the *S. oneidensis and G. sulfurreducens* co-culture to changes in shear stress is actively regulated by gene expression, rather than being a passive outcome of physical forces alone. As MECs are scaled up, flow conditions become more complex, making it important to understand how hydrodynamics influence both biofilm structure and function. This understanding can support the design of flow conditions that improve biofilm stability, activity, and overall system performance in practical applications.

Optimization of substrate concentration proved essential for improving MEC performance. When the concentration of hydrolysate exceeded 40%, system efficiency declined due to increased carbon competition between exoelectrogenic and non-electrogenic microorganisms, indicating that moderate organic loading yields better results. Operating at alkaline pH improved MEC efficiency by favoring the growth of electroactive species and likely stabilizing the proton gradient within the anodic biofilm. Applying higher anodic potentials further enhanced electrochemical performance by promoting EET, enabling *Geobacter* to dominate over competing microbial populations. The highest current density was obtained at 40% hydrolysate, pH 8, and +0.4 V, conditions that enriched *Geobacter* while suppressing methanogenic activity. In the scaled-up system, although hydrogen production was higher at +0.4 V, energy efficiency was greater at 0 V. Despite these operational differences, the hydrogen production cost stayed about the same, showing that running the system for higher productivity is still economically viable. Overall, these results show that adjusting biological and electrochemical parameters is essential for improving MEC efficiency and practical energy recovery.

The H_2 produced by the MECs, by effectively supporting the autotrophic growth of *C. necator* and enabling acetoin production, demonstrated its sustainability. This highlights the practical

potential of integrating MEC-derived biohydrogen with microbial synthesis pathways for the generation of value-added compounds.

Scaling up MECs is essential for evaluating their industrial feasibility, and the findings of this study offer practical insights to guide that process. The demonstrated influence of hydrodynamic conditions on biofilm structure highlights the importance of maintaining controlled flow velocities in larger reactors to ensure stable electroactive biofilms. Likewise, the effects of substrate composition, pH, and applied potential highlight the importance of these operational parameters in balancing microbial activity, electrochemical performance, and energy input under scalable conditions. The successful use of MEC-derived hydrogen to support the autotrophic growth of *C. necator* further confirms the viability of coupling biohydrogen production with downstream bioconversion processes. A robust techno-economic framework grounded in these operational insights will be essential for enabling cost-effective, scalable, and sustainable hydrogen production through MEC technology.

5. References

Abbasian Hamedani, E., Alenabi, S.A., Talebi, S., 2024. Hydrogen as an energy source: A review of production technologies and challenges of fuel cell vehicles. Energy Reports 12, 3778–3794. https://doi.org/10.1016/j.egyr.2024.09.030

Achenbach, L.A., Michaelidou, U., Bruce, R.A., Fryman, J., Coates, J.D., 2001. Dechloromonas agitata gen. nov., sp. nov. and Dechlorosoma suillum gen. nov., sp. nov., two novel environmentally dominant (per)chlorate-reducing bacteria and their phylogenetic position. Int. J. Syst. Evol. Microbiol. 51, 527–533. https://doi.org/10.1099/00207713-51-2-527

Alotaibi, G.F., 2021. Factors Influencing Bacterial Biofilm Formation and Development. Am. J. Biomed. Sci. Res. 12, 617–626. https://doi.org/10.34297/ajbsr.2021.12.001820

Asrul, M.A.M., Atan, M.F., Yun, H.A.H., Wahab, N.A., Hung, H.H., Lai, J.C.H., Tan, I.A.W., 2024. Optimization of Mathematical Modeling of Microbial Electrolysis Cell for the Production of Hydrogen From Sago Wastewater Substrate. ASEAN Eng. J. 14, 7–17. https://doi.org/10.11113/aej.V14.20419

Baeza, J.A., Martínez-Miró, À., Guerrero, J., Ruiz, Y., Guisasola, A., 2017. Bioelectrochemical hydrogen production from urban wastewater on a pilot scale. J. Power Sources 356, 500–509. https://doi.org/10.1016/j.jpowsour.2017.02.087

Baleeiro, F.C.F., Kleinsteuber, S., Sträuber, H., 2021. Hydrogen as a Co-electron Donor for Chain Elongation With Complex Communities. Front. Bioeng. Biotechnol. 9, 1–15. https://doi.org/10.3389/fbioe.2021.650631

Banerjee, A., Calay, R.K., Mustafa, M., 2022. Review on Material and Design of Anode for Microbial Fuel Cell. Energies 15. https://doi.org/10.3390/en15062283

Barceló, A.M., Cortina, I.C., Rodríguez, A.I.A., Ballesteros, C.R., 2016. Biofilms: Microbial Life on Surfaces. An. la Real Acad. Nac. Farm. 82, 108–126.

Baudler, A., Schmidt, I., Langner, M., Greiner, A., Schröder, U., 2015. Does it have to be carbon? Metal anodes in microbial fuel cells and related bioelectrochemical systems. Energy Environ. Sci. 8, 2048–2055. https://doi.org/10.1039/c5ee00866b

Becerril-Varela, K., Serment-Guerrero, J.H., Manzanares-Leal, G.L., Ramírez-Durán, N., Guerrero-Barajas, C., 2021. Generation of electrical energy in a microbial fuel cell coupling acetate oxidation to Fe3+ reduction and isolation of the involved bacteria. World J. Microbiol. Biotechnol. 37, 1–15. https://doi.org/10.1007/s11274-021-03077-4

Board, T.E., 2015. Petrimonas . Bergey's Man. Syst. Archaea Bact. 8, 1–2. https://doi.org/10.1002/9781118960608.gbm00245

Bond, D.R., Lovley, D.R., 2003. Electricity production by Geobacter sulfurreducens attached to electrodes. Appl. Environ. Microbiol. 69, 1548–1555. https://doi.org/10.1128/AEM.69.3.1548-1555.2003

Boto, S.T., Bardl, B., Harnisch, F., Rosenbaum, M.A., 2023. Microbial electrosynthesis with Clostridium ljungdahlii benefits from hydrogen electron mediation and permits a greater variety of products. Green Chem. 4375–4386. https://doi.org/10.1039/d3gc00471f

Brown, D.G., Komlos, J., Jaffé, P.R., 2005. Simultaneous utilization of acetate and hydrogen by Geobacter sulfurreducens and implications for use of hydrogen as an indicator of redox conditions. Environ. Sci. Technol. 39, 3069–3076. https://doi.org/10.1021/es048613p

Caccavo, F., Lonergan, D.J., Lovley, D.R., Davis, M., Stolz, J.F., Mcinerneyl, M.J., 1994. Geobacter sulfurreducens sp. nov., a Hydrogen- and Acetate- Oxidizing Dissimilatory Metal-Reducing Microorganism. Appl. Environ. Microbiol. 60, 3752–3759.

Call, D., Logan, B.E., 2008. Hydrogen production in a single chamber microbial electrolysis

cell lacking a membrane. Environ. Sci. Technol. 42, 3401–3406. https://doi.org/10.1021/es8001822

Cardeña, R., Cercado, B., Buitrón, G., 2019. Microbial Electrolysis Cell for Biohydrogen Production, Biomass, Biofuels, Biochemicals: Biohydrogen, Second Edition. https://doi.org/10.1016/B978-0-444-64203-5.00007-1

Chao, L., Rakshe, S., Leff, M., Spormanna, A.M., 2013. PdeB, a cyclic di-GMP-specific phosphodiesterase that regulates Shewanella oneidensis MR-1 motility and biofilm formation. J. Bacteriol. 195, 3827–3833. https://doi.org/10.1128/JB.00498-13

Choi, Y., Kim, D., Choi, H., Cha, J., Baek, G., Lee, C., 2023. A study of electron source preference and its impact on hydrogen production in microbial electrolysis cells fed with synthetic fermentation effluent. Bioengineered 14, 2244759. https://doi.org/10.1080/21655979.2023.2244759

Commault, A.S., Lear, G., Packer, M.A., Weld, R.J., 2013. Influence of anode potentials on selection of Geobacter strains in microbial electrolysis cells. Bioresour. Technol. 139, 226–234. https://doi.org/10.1016/j.biortech.2013.04.047

Cristiani, L., Leobello, L., Zeppilli, M., Villano, M., 2023. Role of C/N ratio in a pilot scale Microbial Electrolysis Cell (MEC) for biomethane production and biogas upgrading. Renew. Energy 210, 355–363. https://doi.org/10.1016/j.renene.2023.04.049

Cui, W., Liu, G., Zeng, C., Lu, Y., Luo, H., Zhang, R., 2019. Improved hydrogen production in the single-chamber microbial electrolysis cell with inhibition of methanogenesis under alkaline conditions. RSC Adv. 9, 30207–30215. https://doi.org/10.1039/c9ra05483a

Cusick, R.D., Bryan, B., Parker, D.S., Merrill, M.D., Mehanna, M., Kiely, P.D., Liu, G., Logan, B.E., 2011. Performance of a pilot-scale continuous flow microbial electrolysis cell fed winery wastewater. Appl. Microbiol. Biotechnol. 89, 2053–2063.

https://doi.org/10.1007/s00253-011-3130-9

Cusick, R.D., Kiely, P.D., Logan, B.E., 2010. A monetary comparison of energy recovered from microbial fuel cells and microbial electrolysis cells fed winery or domestic wastewaters. Int. J. Hydrogen Energy 35, 8855–8861. https://doi.org/10.1016/j.ijhydene.2010.06.077

Dange, P., Pandit, S., Jadhav, D., Shanmugam, P., Gupta, P.K., Kumar, S., Kumar, M., Yang, Y.H., Bhatia, S.K., 2021. Recent Developments in Microbial Electrolysis Cell-Based Biohydrogen Production Utilizing Wastewater as a Feedstock. Sustain. 13, 1–37.

Darus, L., 2011. Effect of Substrate Concentration to Anode Chamber Performance in Microbial Electrolysis Cell 16, 53–59.

de Fouchécour, F., Larzillière, V., Bouchez, T., Moscoviz, R., 2022. Systematic and quantitative analysis of two decades of anodic wastewater treatment in bioelectrochemical reactors. Water Res. 214. https://doi.org/10.1016/j.watres.2022.118142

Dhar, B.R., Sim, J., Ryu, H., Ren, H., Santo Domingo, J.W., Chae, J., Lee, H.S., 2017. Microbial activity influences electrical conductivity of biofilm anode. Water Res. 127, 230–238. https://doi.org/10.1016/j.watres.2017.10.028

Elgamoudi, B.A., Starr, K.S., Korolik, V., 2022. Extracellular c-di-GMP Plays a Role in Biofilm Formation and Dispersion of Campylobacter jejuni. Microorganisms 10. https://doi.org/10.3390/microorganisms10102030

Elreedy, A., Härrer, D., Ali, R., Hille-Reichel, A., Gescher, J., 2024. Efficacious enrichment of butyrate-oxidizing exoelectrogens upgrades energy recovery in 2 relevant bioelectrochemical systems. Environ. Technol. Innov. 36, 103871.

Energy Institute, Our World in Data, 2025. Statistical Review of World Energy [WWW Document]. URL https://ourworldindata.org/grapher/global-energy-substitution

(accessed 9.10.25).

Engel, C., Schattenberg, F., Dohnt, K., Schröder, U., Müller, S., Krull, R., 2019. Long-term behavior of defined mixed cultures of geobacter sulfurreducens and Shewanella oneidensis in bioelectrochemical systems. Front. Bioeng. Biotechnol. 7, 1–12. https://doi.org/10.3389/fbioe.2019.00060

Escapa, A., San-Martín, M.I., Mateos, R., Morán, A., 2015. Scaling-up of membraneless microbial electrolysis cells (MECs) for domestic wastewater treatment: Bottlenecks and limitations. Bioresour. Technol. 180, 72–78. https://doi.org/10.1016/j.biortech.2014.12.096

Eurostat, 2025. Electricity price statistics [WWW Document].

Fang, Y. of shear stress on tInfluence of shear stress on the intracellular bis-(30. 625pt′0. 625p.-5′)-cyclic dimeric guanosine monophosphate (c-di-G. level within an M. biofilmhe intracellular bis-(3′-5′)-cyclic dimeric guanosine monophosphate (c-, Xiao, N., Chen, D., Field, R.W., Wu, J.J., Wang, B., 2023. Influence of shear stress on the intracellular bis-(30.625pt′0.625pt-5′)-cyclic dimeric guanosine monophosphate (c-di-GMP) level within an MBR biofilm. Chem. Eng. Sci. 280, 118989. https://doi.org/10.1016/j.ces.2023.118989

Fang, Y., Xiao, N., Chen, D., Min, Y., Field, R.W., Wang, B., 2025. MBR water treatment : A CFD and experimental investigation with a focus upon shear stress and the role of c-di-GMP. Desalin. Water Treat. 321, 100942. https://doi.org/10.1016/j.dwt.2024.100942

Farhangi, S., Ebrahimi, S., Niasar, M.S., 2014. Commercial materials as cathode for hydrogen production in microbial electrolysis cell. Biotechnol. Lett. 36, 1987–1992. https://doi.org/10.1007/s10529-014-1565-7

Feng, G., Zeng, Y., Wang, H.Z., Chen, Y.T., Tang, Y.Q., 2023. Proteiniphilum and

Methanothrix harundinacea became dominant acetate utilizers in a methanogenic reactor operated under strong ammonia stress. Front. Microbiol. 13. https://doi.org/10.3389/fmicb.2022.1098814

Flemming, H.C., Wingender, J., Szewzyk, U., Steinberg, P., Rice, S.A., Kjelleberg, S., 2016. Biofilms: An emergent form of bacterial life. Nat. Rev. Microbiol. 14, 563–575. https://doi.org/10.1038/nrmicro.2016.94

Fritz, B., Lapp, C.J., Gescher, J., 2025. Influence of Different Transposon Families on Genomic Stability of Shewanella oneidensis MR1. Microb. Biotechnol. 18. https://doi.org/10.1111/1751-7915.70188

Fudge, T., Bulmer, I., Bowman, K., Pathmakanthan, S., Gambier, W., Dehouche, Z., Al-Salem, S.M., Constantinou, A., 2021. Microbial electrolysis cells for decentralisedwastewater treatment: The next steps. Water (Switzerland) 13. https://doi.org/10.3390/w13040445

Gao, L., Lu, X., Liu, H., Li, J., Li, W., Song, R., Wang, R., Zhang, D., Zhu, J., 2019. Mediation of extracellular polymeric substances in microbial reduction of hematite by shewanella oneidensismr-1. Front. Microbiol. 10, 1–12. https://doi.org/10.3389/fmicb.2019.00575

Gautam, R., Nayak, J.K., Talapatra, K.N., Amit, Ghosh, U.K., 2023. Assessment of different organic substrates for Bio-Electricity and Bio-Hydrogen generation in an Integrated Bio-Electrochemical System. Mater. Today Proc. 80, 2255–2259. https://doi.org/10.1016/j.matpr.2021.06.223

Gil-Carrera, L., Escapa, A., Mehta, P., Santoyo, G., Guiot, S.R., Morán, A., Tartakovsky, B., 2013. Microbial electrolysis cell scale-up for combined wastewater treatment and hydrogen production. Bioresour. Technol. 130, 584–591. https://doi.org/10.1016/j.biortech.2012.12.062

Godain, A., Vogel, T.M., Fongarland, P., Haddour, N., 2024. Influence of shear stress on

electroactive biofilm characteristics and performance in microbial fuel cells. Biosens. Bioelectron. 244, 115806. https://doi.org/10.1016/j.bios.2023.115806

Grobbler, C., Virdis, B., Nouwens, A., Harnisch, F., Rabaey, K., Bond, P.L., 2018. Effect of the anode potential on the physiology and proteome of Shewanella oneidensis MR-1. Bioelectrochemistry 119, 172–179. https://doi.org/10.1016/j.bioelechem.2017.10.001

Grobbler, C., Virdis, B., Nouwens, A., Harnisch, F., Rabaey, K., Bond, P.L., 2015. Use of SWATH mass spectrometry for quantitative proteomic investigation of Shewanella oneidensis MR-1 biofilms grown on graphite cloth electrodes. Syst. Appl. Microbiol. 38, 135–139. https://doi.org/10.1016/j.syapm.2014.11.007

Güçyetmez, M., Akkaya, S., Uyar, M., Hayber, Ş.E., 2025. Forecasting renewable energy consumption with hydrogen integration: A comprehensive regression approach. Int. J. Hydrogen Energy 142, 981–993. https://doi.org/10.1016/j.ijhydene.2025.03.244

Guerrero-Sodric, O., Baeza, J.A., Guisasola, A., 2023. Exploring key operational factors for improving hydrogen production in a pilot-scale microbial electrolysis cell treating urban wastewater. Chem. Eng. J. 469, 144001. https://doi.org/10.1016/j.cej.2023.144001

Hackbarth, M., Gescher, J., Horn, H., Reiner, J.E., 2023. A scalable, rotating disc bioelectrochemical reactor (RDBER) suitable for the cultivation of both cathodic and anodic biofilms. Bioresour. Technol. Reports 21, 101357. https://doi.org/10.1016/j.biteb.2023.101357

Halim, M.A., Rahman, M.O., Ibrahim, M., Kundu, R., Biswas, B.K., 2021. Effect of Anolyte pH on the Performance of a Dual-Chambered Microbial Fuel Cell Operated with Different Biomass Feed. J. Chem. 2021. https://doi.org/10.1155/2021/5465680

Härrer, D., Elreedy, A., Ali, R., Hille-Reichel, A., Gescher, J., 2022. Probing the Robustness of Geobacter Sulfurreducens Against Fermentation Hydrolysate for Uses in

Bioelectrochemical Systems. SSRN Electron. J. 369, 128363. https://doi.org/10.2139/ssrn.4239421

Härrer, D., Windhorst, C., Böhner, N., Novion Ducassou, J., Couté, Y., Gescher, J., 2021. Production of acetoin from renewable resources under heterotrophic and mixotrophic conditions. Bioresour. Technol. 329. https://doi.org/10.1016/j.biortech.2021.124866

Häuser, L., Erben, J., Pillot, G., Kerzenmacher, S., Dreher, W., Küstermann, E., 2022. In vivo characterization of electroactive biofilms inside porous electrodes with MR Imaging. RSC Adv. 12, 17784–17793. https://doi.org/10.1039/d2ra01162j

Heidrich, E.S., Edwards, S.R., Dolfing, J., Cotterill, S.E., Curtis, T.P., 2014. Performance of a pilot scale microbial electrolysis cell fed on domestic wastewater at ambient temperatures for a 12month period. Bioresour. Technol. 173, 87–95. https://doi.org/10.1016/j.biortech.2014.09.083

Hirose, A., Kasai, T., Aoki, M., Umemura, T., Watanabe, K., Kouzuma, A., 2018. Electrochemically active bacteria sense electrode potentials for regulating catabolic pathways. Nat. Commun. 9, 1–10. https://doi.org/10.1038/s41467-018-03416-4

Hodgson, D.M., Smith, A., Dahale, S., Stratford, J.P., Li, J. V., Grüning, A., Bushell, M.E., Marchesi, J.R., Avignone Rossa, C., 2016. Segregation of the anodic microbial communities in a microbial fuel cell cascade. Front. Microbiol. 7, 1–11. https://doi.org/10.3389/fmicb.2016.00699

Howley, E., Krajmalnik-Brown, R., Torres, C.I., 2023. Cytochrome gene expression shifts in Geobacter sulfurreducens to maximize energy conservation in response to changes in redox conditions. Biosens. Bioelectron. 237. https://doi.org/10.1016/j.bios.2023.115524

Hu, H., Fan, Y., Liu, H., 2009. Hydrogen production in single-chamber tubular microbial electrolysis cells using non-precious-metal catalysts. Int. J. Hydrogen Energy 34, 8535–

8542. https://doi.org/10.1016/j.ijhydene.2009.08.011

Hu, H., Fan, Y., Liu, H., 2008. Hydrogen production using single-chamber membrane-free microbial electrolysis cells. Water Res. 42, 4172–4178. https://doi.org/10.1016/j.watres.2008.06.015

Hua, T., Li, S., Li, F., Zhou, Q., Ondon, B.S., 2019. Microbial electrolysis cell as an emerging versatile technology: a review on its potential application, advance and challenge. J. Chem. Technol. Biotechnol. 94, 1697–1711. https://doi.org/10.1002/jctb.5898

Huang, L., Wan, H., Song, S., Liu, D., Li, G., 2022. Complete removal of heavy metals with simultaneous efficient treatment of etching terminal wastewater using scaled-up microbial electrolysis cells. Chem. Eng. J. 439, 135763. https://doi.org/10.1016/j.cej.2022.135763

Islam, M.A., Ehiraj, B., Cheng, C.K., Dubey, B.N., Khan, M.M.R., 2019. Biofilm re-vitalization using hydrodynamic shear stress for stable power generation in microbial fuel cell. J. Electroanal. Chem. 844, 14–22. https://doi.org/10.1016/j.jelechem.2019.05.013

Jadhav, D.A., Chendake, A.D., Schievano, A., Pant, D., 2019. Suppressing methanogens and enriching electrogens in bioelectrochemical systems. Bioresour. Technol. 277, 148–156. https://doi.org/10.1016/j.biortech.2018.12.098

Jiang, Y. Bin, Zhong, W.H., Han, C., Deng, H., 2016. Characterization of electricity generated by soil in microbial fuel cells and the isolation of soil source exoelectrogenic bacteria. Front. Microbiol. 7, 1–10. https://doi.org/10.3389/fmicb.2016.01776

Jiang, J., Lopez-Ruiz, J.A., Bian, Y., Sun, D., Yan, Y., Chen, X., Zhu, J., May, H.D., Ren, Z.J., 2023. Scale-up and techno-economic analysis of microbial electrolysis cells for hydrogen production from wastewater. Water Res. 241, 120139. https://doi.org/10.1016/j.watres.2023.120139

Jin, J., Amanze, C., Anaman, R., Zheng, X., Qiu, G., Zeng, W., 2022. Electrochemical

Responses and Microbial Community Shift of Electroactive Biofilm to Acidity Stress in Microbial Fuel Cells. Minerals 12. https://doi.org/10.3390/min12101268

Jones, A.-A.D., 2018. Exoelectrogenic Biofilm Growth in Shearing Flows 1–100. https://doi.org/1721.1/115610

Jones, A.A.D., Buie, C.R., 2019. Continuous shear stress alters metabolism, mass-transport, and growth in electroactive biofilms independent of surface substrate transport. Sci. Rep. 9, 1–8. https://doi.org/10.1038/s41598-019-39267-2

Kadier, A., Jain, P., Lai, B., Kalil, M.S., Kondaveeti, S., Alabbosh, K.F.S., Abu-Reesh, I.M., Mohanakrishna, G., 2020. Biorefinery perspectives of microbial electrolysis cells (MECs) for hydrogen and valuable chemicals production through wastewater treatment. Biofuel Res. J. 7, 1128–1142. https://doi.org/10.18331/BRJ2020.7.1.5

Kadier, A., Kalil, M.S., Abdeshahian, P., Chandrasekhar, K., Mohamed, A., Azman, N.F., Logroño, W., Simayi, Y., Hamid, A.A., 2016. Recent advances and emerging challenges in microbial electrolysis cells (MECs) for microbial production of hydrogen and value-added chemicals. Renew. Sustain. Energy Rev. 61, 501–525. https://doi.org/10.1016/j.rser.2016.04.017

Karthikeyan, R., Cheng, K.Y., Selvam, A., Bose, A., Wong, J.W.C., 2017. Bioelectrohydrogenesis and inhibition of methanogenic activity in microbial electrolysis cells - A review. Biotechnol. Adv. 35, 758–771. https://doi.org/10.1016/j.biotechadv.2017.07.004

Kilicaslan, A.F., Dincer, I., Khalvati, A., 2024. Microbial electrolysis cells designed for BioH2 production: Potential improvements with carbon dioxide and nitrogen. Int. J. Hydrogen Energy 62, 794–802. https://doi.org/10.1016/j.ijhydene.2024.03.104

Kitayama, M., Koga, R., Kasai, T., Kouzuma, A., Watanabe, K., 2017. Structures,

compositions, and activities of live Shewanella biofilms formed on graphite electrodes in electrochemical flow cells. Appl. Environ. Microbiol. 83. https://doi.org/10.1128/AEM.00903-17

Klein, E., Weiler, J., Wagner, M., Čelikić, M., Niemeyer, C.M., Horn, H., Gescher, J., 2022. Enrichment of phosphate-accumulating organisms (PAOs) in a microfluidic model biofilm system by mimicking a typical aerobic granular sludge feast/famine regime. Appl. Microbiol. Biotechnol. 106, 1313–1324. https://doi.org/10.1007/s00253-022-11759-8

Klein, E., Wurst, R., Rehnlund, D., Gescher, J., 2024. Elucidating the development of cooperative anode-biofilm-structures. Biofilm 7. https://doi.org/10.1016/j.bioflm.2024.100193

Klein, E.M., Heintz, H., Wurst, R., Schuldt, S., Hähl, H., Jacobs, K., Gescher, J., 2024. Comparative analysis of the influence of BpfA and BpfG on biofilm development and current density in Shewanella oneidensis under oxic, fumarate- and anode-respiring conditions. Sci. Rep. 14, 1–12. https://doi.org/10.1038/s41598-024-73474-w

Knoll, M.T., Jürgensen, N., Weiler, J.R., Gescher, J., 2023. Predictability and robustness of anode biofilm to changing potential in microbial electrolysis system. Bioresour. Technol. Reports 24, 101640. https://doi.org/10.1016/j.biteb.2023.101640

Koch, C., Harnisch, F., 2016. Is there a Specific Ecological Niche for Electroactive Microorganisms? ChemElectroChem 3, 1282–1295. https://doi.org/10.1002/celc.201600079

Korth, B., Harnisch, F., 2019. Spotlight on the energy harvest of electroactive microorganisms: The impact of the applied anode potential. Front. Microbiol. 10, 1–9. https://doi.org/10.3389/fmicb.2019.01352

Koul, Y., Devda, V., Varjani, S., Guo, W., Ngo, H.H., Taherzadeh, M.J., Chang, J.S., Wong,

J.W.C., Bilal, M., Kim, S.H., Bui, X.T., Parra-Saldívar, R., 2022. Microbial electrolysis: a promising approach for treatment and resource recovery from industrial wastewater. Bioengineered 13, 8115–8134. https://doi.org/10.1080/21655979.2022.2051842

Kumar, G., Bakonyi, P., Zhen, G., Sivagurunathan, P., Koók, L., Kim, S.H., Tóth, G., Nemestóthy, N., Bélafi-Bakó, K., 2017. Microbial electrochemical systems for sustainable biohydrogen production: Surveying the experiences from a start-up viewpoint. Renew. Sustain. Energy Rev. 70, 589–597. https://doi.org/10.1016/j.rser.2016.11.107

Kyazze, G., Popov, A., Dinsdale, R., Esteves, S., Hawkes, F., Premier, G., Guwy, A., 2010. Influence of catholyte pH and temperature on hydrogen production from acetate using a two chamber concentric tubular microbial electrolysis cell. Int. J. Hydrogen Energy 35, 7716–7722. https://doi.org/10.1016/j.ijhydene.2010.05.036

Latif, M.A., Mehta, C.M., Batstone, D.J., 2017. Influence of low pH on continuous anaerobic digestion of waste activated sludge. Water Res. 113, 42–49. https://doi.org/10.1016/j.watres.2017.02.002

Le, P.A., Trung, V.D., Nguyen, P.L., Bac Phung, T.V., Natsuki, J., Natsuki, T., 2023. The current status of hydrogen energy: an overview. RSC Adv. 13, 28262–28287. https://doi.org/10.1039/d3ra05158g

Li, S., 2018. Factors Affecting the Effectiveness of Bioelectrochemical System Applications : Data 1–18. https://doi.org/10.3390/batteries4030034

Li, Y., Zong, Y., Feng, C., Zhao, K., 2025. The Role of Anode Potential in Electromicrobiology. Microorganisms 13, 1–23. https://doi.org/10.3390/microorganisms13030631

Liu, H., Cheng, S., Logan, B.E., 2005. Power generation in fed-batch microbial fuel cells as a function of ionic strength, temperature, and reactor configuration. Environ. Sci. Technol.

39, 5488–5493. https://doi.org/10.1021/es050316c

Liu, S., Dong, F., Zhang, D., Zhang, J., Wang, X., 2022. Effect of microfluidic channel geometry on Bacillus subtilis biofilm formation. Biomed. Microdevices 24, 1–11. https://doi.org/10.1007/s10544-022-00612-4

Logan, B.E., Rabaey, K., 2012. Conversion of wastes into bioelectricity and chemicals by using microbial electrochemical technologies. Science (80-.). 337, 686–690. https://doi.org/10.1126/science.1217412

Lu, L., Ren, N., Zhao, X., Wang, H., Wu, D., Xing, D., 2011. Hydrogen production, methanogen inhibition and microbial community structures in psychrophilic single-chamber microbial electrolysis cells. Energy Environ. Sci. 4, 1329–1336. https://doi.org/10.1039/c0ee00588f

Lu, L., Xing, D., Liu, B., Ren, N., 2012a. Enhanced hydrogen production from waste activated sludge by cascade utilization of organic matter in microbial electrolysis cells. Water Res. 46, 1015–1026. https://doi.org/10.1016/j.watres.2011.11.073

Lu, L., Xing, D., Ren, N., 2012b. Pyrosequencing reveals highly diverse microbial communities in microbial electrolysis cells involved in enhanced H2 production from waste activated sludge. Water Res. 46, 2425–2434. https://doi.org/10.1016/j.watres.2012.02.005

Ma, S., Zhang, Y., Tu, L., Li, X., Chen, X., Lin, S., Luo, H., Zhan, X., Liu, G., 2024. Efficient hydrogen production from food waste leachate using single-chamber microbial electrolysis cell. Environ. Res. 263, 120159. https://doi.org/10.1016/j.envres.2024.120159

Manuel, M.F., Neburchilov, V., Wang, H., Guiot, S.R., Tartakovsky, B., 2010. Hydrogen production in a microbial electrolysis cell with nickel-based gas diffusion cathodes. J.

Power Sources 195, 5514–5519. https://doi.org/10.1016/j.jpowsour.2010.03.061

Matsuda, S., Liu, H., Kouzuma, A., Watanabe, K., Hashimoto, K., Nakanishi, S., 2013. Electrochemical Gating of Tricarboxylic Acid Cycle in Electricity-Producing Bacterial Cells of Shewanella. PLoS One 8, 1–8. https://doi.org/10.1371/journal.pone.0072901

Matsumoto, A., Koga, R., Kanaly, R.A., Kouzuma, A., Watanabe, K., 2021. Identification of a Diguanylate Cyclase That Facilitates Biofilm Formation on Electrodes by Shewanella oneidensis MR-1. Appl. Environ. Microbiol. 87, 1–11. https://doi.org/10.1128/AEM.00201-21

Mission Innovation Hydrogen Valley Platform, 2025. Hydrogen cost and sales prices [WWW Document].

Muddasar, M., Liaquat, R., Aslam, A., Ur Rahman, M.Z., Abdullah, A., Khoja, A.H., Latif, K., Bahadar, A., 2022. Performance efficiency comparison of microbial electrolysis cells for sustainable production of biohydrogen—A comprehensive review. Int. J. Energy Res. 46, 5625–5645. https://doi.org/10.1002/er.7606

Nam, J.Y., Logan, B.E., 2012. Optimization of catholyte concentration and anolyte pHs in two chamber microbial electrolysis cells. Int. J. Hydrogen Energy 37, 18622–18628. https://doi.org/10.1016/j.ijhydene.2012.09.140

Nam, J.Y., Logan, B.E., 2011. Enhanced hydrogen generation using a saline catholyte in a two chamber microbial electrolysis cell. Int. J. Hydrogen Energy 36, 15105–15110. https://doi.org/10.1016/j.ijhydene.2011.08.106

Nam, J.Y., Tokash, J.C., Logan, B.E., 2011. Comparison of microbial electrolysis cells operated with added voltage or by setting the anode potential. Int. J. Hydrogen Energy 36, 10550–10556. https://doi.org/10.1016/j.ijhydene.2011.05.148

Nawaz, A., Hafeez, A., Abbas, S.Z., Haq, I. ul, Mukhtar, H., Rafatullah, M., 2020. A state of

the art review on electron transfer mechanisms, characteristics, applications and recent advancements in microbial fuel cells technology. Green Chem. Lett. Rev. 13, 101–117. https://doi.org/10.1080/17518253.2020.1854871

Netsch, A., Latussek, I., Horn, H., Wagner, M., 2025a. Detecting Excess Biofilm Thickness in Microbial Electrolysis Cells by Real-Time In-Situ Biofilm Monitoring. Biotechnol. Bioeng. 122, 2049–2062. https://doi.org/10.1002/bit.29017

Netsch, A., Sen, S., Horn, H., Wagner, M., 2025b. In-Situ Biofilm Monitoring Using a Heat-Transfer Sensor : Impact of Flow Velocity in Pipe and Planar System 0–20. https://doi.org/10.20944/preprints202501.0679.v1

Park, S.G., Rajesh, P.P., Sim, Y.U., Jadhav, D.A., Noori, M.T., Kim, D.H., Al-Qaradawi, S.Y., Yang, E., Jang, J.K., Chae, K.J., 2022. Addressing scale-up challenges and enhancement in performance of hydrogen-producing microbial electrolysis cell through electrode modifications. Energy Reports 8, 2726–2746. https://doi.org/10.1016/j.egyr.2022.01.198

Patil, S.A., Harnisch, F., Koch, C., Hübschmann, T., Fetzer, I., Carmona-Martínez, A.A., Müller, S., Schröder, U., 2011. Electroactive mixed culture derived biofilms in microbial bioelectrochemical systems: The role of pH on biofilm formation, performance and composition. Bioresour. Technol. 102, 9683–9690. https://doi.org/10.1016/j.biortech.2011.07.087

Paul, E., Ochoa, J.C., Pechaud, Y., Liu, Y., Line, A., 2012. Effect of shear stress and growth conditions on detachment and physical properties of biofilms 6, 0–9. https://doi.org/10.1016/j.watres.2012.07.029

Peng, L., You, S.J., Wang, J.Y., 2010. Electrode potential regulates cytochrome accumulation on Shewanella oneidensis cell surface and the consequence to bioelectrocatalytic current generation. Biosens. Bioelectron. 25, 2530–2533.

https://doi.org/10.1016/j.bios.2010.03.039

Pérez-rodríguez, P., 2025. Corona-Martinez et al., 2025 1–18.

Pham, H.T., Boon, N., Aelterman, P., Clauwaert, P., Schamphelaire, L. De, Oostveldt, P. Van, Verbeken, K., Rabaey, K., Verstraete, W., 2008. High shear enrichment improves the performance of the anodophilic microbial consortium in a microbial fuel cell 1, 487–496. https://doi.org/10.1111/j.1751-7915.2008.00049.x

Qiu, S., Zhang, X., Xia, W., Li, Z., Wang, L., Chen, Z., Ge, S., 2023. Effect of extreme pH conditions on methanogenesis: Methanogen metabolism and community structure. Sci. Total Environ. 877, 162702. https://doi.org/10.1016/j.scitotenv.2023.162702

Rabaey, K., Boon, N., Siciliano, S.D., Verhaege, M., Verstraete, W., 2004. Biofuel cells select for microbial consortia that self-mediate electron transfer. Appl. Environ. Microbiol. 70, 5373–5382. https://doi.org/10.1128/AEM.70.9.5373-5382.2004

Rago, L., Baeza, J.A., Guisasola, A., 2016. Increased performance of hydrogen production in microbial electrolysis cells under alkaline conditions. Bioelectrochemistry 109, 57–62. https://doi.org/10.1016/j.bioelechem.2016.01.003

Raheem, A., Hassan, M.Y., Shakoor, R., 2016. Bioenergy from anaerobic digestion in Pakistan: Potential, development and prospects. Renew. Sustain. Energy Rev. 59, 264–275. https://doi.org/10.1016/j.rser.2016.01.010

Reda, B., Elzamar, A.A., AlFazzani, S., Ezzat, S.M., 2024. Green hydrogen as a source of renewable energy: a step towards sustainability, an overview. Environ. Dev. Sustain. https://doi.org/10.1007/s10668-024-04892-z

Sadhukhan, J., Lloyd, J.R., Scott, K., Premier, G.C., Yu, E.H., Curtis, T., Head, I.M., 2016. A critical review of integration analysis of microbial electrosynthesis (MES) systems with waste biorefineries for the production of biofuel and chemical from reuse of CO2. Renew.

Sustain. Energy Rev. 56, 116–132. https://doi.org/10.1016/j.rser.2015.11.015

Saravanan, A., Karishma, S., Kumar, P.S., Yaashikaa, P.R., Jeevanantham, S., Gayathri, B., 2023. Microbial electrolysis cells and microbial fuel cells for biohydrogen production: current advances and emerging challenges. Biomass Convers. Biorefinery 13, 8403–8423. https://doi.org/10.1007/s13399-020-00973-x

Sauer, K., Stoodley, P., Goeres, D.M., Hall-Stoodley, L., Burmølle, M., Stewart, P.S., Bjarnsholt, T., 2022. The biofilm life cycle: expanding the conceptual model of biofilm formation. Nat. Rev. Microbiol. 2022 1–13. https://doi.org/10.1038/s41579-022-00767-0

Sharma, A., Hussain Mehdi, S.E., Pandit, S., Eun-Oh, S., Natarajan, V., 2024. Factors affecting hydrogen production in microbial electrolysis cell (MEC): A review. Int. J. Hydrogen Energy 61, 1473–1484. https://doi.org/10.1016/j.ijhydene.2024.02.193

Shen, R., Liu, Z., He, Y., Zhang, Y., Lu, J., Zhu, Z., Si, B., Zhang, C., Xing, X.H., 2016. Microbial electrolysis cell to treat hydrothermal liquefied wastewater from cornstalk and recover hydrogen: Degradation of organic compounds and characterization of microbial community. Int. J. Hydrogen Energy 41, 4132–4142. https://doi.org/10.1016/j.ijhydene.2016.01.032

Shen, Y., Wang, M., Chang, I.S., Ng, H.Y., 2013. Effect of shear rate on the response of microbial fuel cell toxicity sensor to Cu(II). Bioresour. Technol. 136, 707–710. https://doi.org/10.1016/j.biortech.2013.02.069

Silva, G.O.R. e., Carpanez, T.G., Dos Santos, C.R., Casella, G.S., Moreira, V.R., de Paula, E.C., Amaral, M.C.S., 2024. Biohydrogen production from wastewater: Production technologies, environmental and economic aspects. J. Environ. Chem. Eng. 12. https://doi.org/10.1016/j.jece.2024.114104

Singh, L., Miller, A.G., Wang, L., Liu, H., 2021. Scaling-up up-flow microbial electrolysis

cells with a compact electrode configuration for continuous hydrogen production. Bioresour. Technol. 331, 125030. https://doi.org/10.1016/j.biortech.2021.125030

Sleutels, T.H.J.A., Darus, L., Hamelers, H.V.M., Buisman, C.J.N., 2011. Effect of operational parameters on Coulombic efficiency in bioelectrochemical systems. Bioresour. Technol. 102, 11172–11176. https://doi.org/10.1016/j.biortech.2011.09.078

Sleutels, T.H.J.A., Molenaar, S.D., Heijne, A. Ter, Buisman, C.J.N., 2016. Low substrate loading limits methanogenesis and leads to high coulombic efficiency in bioelectrochemical systems. Microorganisms 4. https://doi.org/10.3390/microorganisms4010007

Sleutels, T.H.J.A., Ter Heijne, A., Buisman, C.J.N., Hamelers, H.V.M., 2012. Bioelectrochemical systems: An outlook for practical applications. ChemSusChem 5, 1012–1019. https://doi.org/10.1002/cssc.201100732

Song, J., Sasaki, D., Sasaki, K., Kato, S., Kondo, A., Hashimoto, K., Nakanishi, S., 2016. Comprehensive metabolomic analyses of anode-respiring Geobacter sulfurreducens cells: The impact of anode-respiration activity on intracellular metabolite levels. Process Biochem. 51, 34–38. https://doi.org/10.1016/j.procbio.2015.11.012

Speers, A.M., Reguera, G., 2012. Electron donors supporting growth and electroactivity of geobacter sulfurreducens anode biofilms. Appl. Environ. Microbiol. 78, 437–444. https://doi.org/10.1128/AEM.06782-11

Spiess, S., Kucera, J., Seelajaroen, H., Sasiain, A., Thallner, S., Kremser, K., Novak, D., Guebitz, G.M., Haberbauer, M., 2021. Impact of carbon felt electrode pretreatment on anodic biofilm composition in microbial electrolysis cells. Biosensors 11. https://doi.org/10.3390/bios11060170

Srivastava, P., García-Quismondo, E., Palma, J., González-Fernández, C., 2024. Coupling dark

fermentation and microbial electrolysis cells for higher hydrogen yield: Technological competitiveness and challenges. Int. J. Hydrogen Energy 52, 223–239. https://doi.org/10.1016/j.ijhydene.2023.04.293

Sun, H., Li, J., Yang, M., Shao, Q., 2019. Influence of initial pH on anodic biofilm formation in single-chambered microbial electrolysis cells. Polish J. Environ. Stud. 28, 1377–1384. https://doi.org/10.15244/pjoes/89503

Sun, M., Liu, B., Yanagawa, K., Ha, N.T., Goel, R., Terashima, M., Yasui, H., 2020. Effects of low pH conditions on decay of methanogenic biomass. Water Res. 179, 115883. https://doi.org/10.1016/j.watres.2020.115883

Sun, Y., ter Heijne, A., Rijnaarts, H., Chen, W.S., 2022. The effect of anode potential on electrogenesis, methanogenesis and sulfidogenesis in a simulated sewer condition. Water Res. 226, 119229. https://doi.org/10.1016/j.watres.2022.119229

Tran, P., Lander, S.M., Prindle, A., 2024. Development in a Minimally Buffered Environment 15, 1–14.

Tymofiiv, V., Al-Rabeei, S., Hovanec, M., Korba, P., 2022. Hydrogen Production for Improved Transportation System as a Part of Smart Cities. Lect. Notes Inst. Comput. Sci. Soc. Telecommun. Eng. LNICST 445 LNICST, 221–233. https://doi.org/10.1007/978-3-031-15101-9_16

Ullah, Z., Zeshan, S., 2020. Effect of substrate type and concentration on the performance of a double chamber microbial fuel cell. Water Sci. Technol. 81, 1336–1344. https://doi.org/10.2166/wst.2019.387

Valiei, A., Dickson, A., Aminian-Dehkordi, J., Mofrad, M.R.K., 2024. Metabolic interactions shape emergent biofilm structures in a conceptual model of gut mucosal bacterial communities. npj Biofilms Microbiomes 10, 1–13. https://doi.org/10.1038/s41522-024-

00572-y

Varanasi, J.L., Veerubhotla, R., Pandit, S., Das, D., 2018. Biohydrogen production using microbial electrolysis cell: Recent advances and future prospects. Biomass, Biofuels, Biochem. Microb. Electrochem. Technol. Sustain. Platf. Fuels, Chem. Remediat. 843–869. https://doi.org/10.1016/B978-0-444-64052-9.00035-2

Venkateswaran, K., Dollhopf, M.E., Lies, D.P., Saffarini, D.A., Gregor, B.J.M., White, D.C., Ni, M., Ri, D.B., Stackebrandp, E., Nealsonl, K.H., Shewanella, K., 2008. Polyphasic taxonomy of the genus Shewanella and description of Shewanella oneidensis sp. now 1–20.

Wagner, M., Taherzadeh, D., Haisch, C., Horn, H., 2010. Investigation of the mesoscale structure and volumetric features of biofilms using optical coherence tomography. Biotechnol. Bioeng. 107, 844–853. https://doi.org/10.1002/bit.22864

Wagner, R.C., Call, D.F., Logan, B.E., 2010. Optimal set anode potentials vary in bioelectrochemical systems. Environ. Sci. Technol. 44, 6036–6041. https://doi.org/10.1021/es101013e

Wang, A., Liu, W., Cheng, S., Xing, D., Zhou, J., Logan, B.E., 2009. Source of methane and methods to control its formation in single chamber microbial electrolysis cells. Int. J. Hydrogen Energy 34, 3653–3658. https://doi.org/10.1016/j.ijhydene.2009.03.005

Wang, H., Ren, Z.J., 2013. A comprehensive review of microbial electrochemical systems as a platform technology. Biotechnol. Adv. 31, 1796–1807. https://doi.org/10.1016/j.biotechadv.2013.10.001

Wang, L., Linowski, K., Liu, H., 2023. Scalable membrane-less microbial electrolysis cell with multiple compact electrode assemblies for high performance hydrogen production. Chem. Eng. J. 454, 140257. https://doi.org/10.1016/j.cej.2022.140257

Wang, L., Long, F., Liang, D., Xiao, X., Liu, H., 2021. Hydrogen production from lignocellulosic hydrolysate in an up-scaled microbial electrolysis cell with stacked bio-electrodes. Bioresour. Technol. 320, 124314. https://doi.org/10.1016/j.biortech.2020.124314

Wang, S., Zhu, H., Zheng, G., Dong, F., Liu, C., 2022a. Dynamic Changes in Bio fi lm Structures under Dynamic Flow. Appl. Environ. Microsc.

Wang, S., Zhu, H., Zheng, G., Dong, F., Liu, C., 2022b. Dynamic Changes in Biofilm Structures under Dynamic Flow Conditions. Appl. Environ. Microbiol. 88, 1–14. https://doi.org/10.1128/aem.01072-22

Wang, X., Feng, Y., Ren, N., Wang, H., Lee, H., Li, N., Zhao, Q., 2009. Accelerated start-up of two-chambered microbial fuel cells: Effect of anodic positive poised potential. Electrochim. Acta 54, 1109–1114. https://doi.org/10.1016/j.electacta.2008.07.085

Wang, X., Lv, M., Zhang, L., Li, K., Gao, C., Ma, C., Xu, P., 2013. Efficient bioconversion of 2,3-butanediol into acetoin using Gluconobacter oxydans DSM 2003. Biotechnol. Biofuels 6, 1–9. https://doi.org/10.1186/1754-6834-6-155

Weiler, J.R., Jürgensen, N., Cornejo Infante, M., Knoll, M.T., Gescher, J., 2024. Strain and model development for auto- and heterotrophic 2,3-butanediol production using Cupriavidus necator H16. Biotechnol. Biofuels Bioprod. 17, 1–16. https://doi.org/10.1186/s13068-024-02549-7

Wijeyekoon, S., Mino, T., Satoh, H., Matsuo, T., 2004. Effects of substrate loading rate on biofilm structure. Water Res. 38, 2479–2488. https://doi.org/10.1016/j.watres.2004.03.005

Xiao, Y., Zheng, Y., Wu, S., Zhang, E.H., Chen, Z., Liang, P., Huang, X., Yang, Z.H., Ng, I.S., Chen, B.Y., Zhao, F., 2015. Pyrosequencing reveals a core community of anodic bacterial

biofilms in bioelectrochemical systems from China. Front. Microbiol. 6, 1410. https://doi.org/10.3389/fmicb.2015.01410

Xiao, Z., Lu, J.R., 2014. Generation of acetoin and its derivatives in foods. J. Agric. Food Chem. 62, 6487–6497. https://doi.org/10.1021/jf5013902

Xiao, Z., Xu, P., 2007. Acetoin metabolism in bacteria. Crit. Rev. Microbiol. 33, 127–140. https://doi.org/10.1080/10408410701364604

Xin, X., Qiu, W., 2021. Linking microbial mechanism with bioelectricity production in sludge matrix-fed microbial fuel cells: Freezing/thawing liquid versus fermentation liquor. Sci. Total Environ. 752, 141907. https://doi.org/10.1016/j.scitotenv.2020.141907

Yang, J., Cheng, S., Li, C., Sun, Y., Huang, H., 2019. Shear stress affects biofilm structure and consequently current generation of bioanode in microbial electrochemical systems (MESS). Front. Microbiol. 10, 1–8. https://doi.org/10.3389/fmicb.2019.00398

Yang, Y., Xu, M., Guo, J., Sun, G., 2012. Bacterial extracellular electron transfer in bioelectrochemical systems. Process Biochem. 47, 1707–1714. https://doi.org/10.1016/j.procbio.2012.07.032

Yi, Y., Wang, H.Z., Chen, Y.T., Gou, M., Xia, Z.Y., Hu, B., Nie, Y., Tang, Y.Q., 2019. Identification of Novel Butyrate- and Acetate-Oxidizing Bacteria in Butyrate-Fed Mesophilic Anaerobic Chemostats by DNA-Based Stable Isotope Probing. Microb. Ecol. https://doi.org/10.1007/s00248-019-01400-z

Yun, W.H., Yoon, Y.S., Yoon, H.H., Nguyen, P.K.T., Hur, J., 2021. Hydrogen production from macroalgae by simultaneous dark fermentation and microbial electrolysis cell with surface-modified stainless steel mesh cathode. Int. J. Hydrogen Energy 46, 39136–39145. https://doi.org/10.1016/j.ijhydene.2021.09.168

Zhang, L., Jiang, Z., Tsui, T.H., Loh, K.C., Dai, Y., Tong, Y.W., 2022. A Review on Enhancing

Cupriavidus necator Fermentation for Poly(3-hydroxybutyrate) (PHB) Production From Low-Cost Carbon Sources. Front. Bioeng. Biotechnol. 10, 1–14. https://doi.org/10.3389/fbioe.2022.946085

Zhao, F., Heidrich, E.S., Curtis, T.P., Dolfing, J., 2020. The effect of anode potential on current production from complex substrates in bioelectrochemical systems: a case study with glucose. Appl. Microbiol. Biotechnol. 104, 5133–5143. https://doi.org/10.1007/s00253-020-10547-6

Zheng, S., Liu, F., Wang, B., Zhang, Y., Lovley, D.R., 2020. Methanobacterium Capable of Direct Interspecies Electron Transfer. Environ. Sci. Technol. 54, 15347–15354. https://doi.org/10.1021/acs.est.0c05525

Zhou, GuangqiRegulation of biofilm formation by BpfA, BpfD, and B. in S. oneidensis, Yuan, J., Gao, H., 2015. Regulation of biofilm formation by BpfA, BpfD, and BpfG in Shewanella oneidensis. Front. Microbiol. 6, 1–11. https://doi.org/10.3389/fmicb.2015.00790

6. Appendix

6.1. Supplementary Tables:

Table S1. Significantly differentially expressed genes (p-value < 0.1; fold change ≥ 5) were identified from transcriptomic analysis of *G. sulfurreducens–S. oneidensis* MR-1 co-culture at a flow velocity of 0.8 mm/s compared to 0.2 mm/s. Positive fold change values indicate upregulated genes; negative values indicate downregulated genes.

Old identifier	Function	Fold change	*p*-Value
GSU0831	P-II family nitrogen regulator	6,5	3E-05
SO_0033	LysM domain-containing protein	5,8	0,06
SO_0144	oligopeptidase B	8,8	0,06
SO_0300	penicillin-binding protein activator	5,4	0,03
SO_0336	Na+/H+ antiporter NhaC family protein	6,9	0,07
SO_0359	bifunctional GTP diphosphokinase/guanosine-3',5'-bis pyrophosphate 3'-pyrophosphohydrolase	15,0	0,01
SO_0380	HsdR family type I site-specific deoxyribonuclease	7,4	0,09
SO_0416	type IV-A pilus assembly ATPase PilB	5,7	0,09
SO_0423	pyruvate dehydrogenase complex transcriptional repressor PdhR	5,5	0,04
SO_0441	phosphoribosylamine--glycine ligase	7,0	0,08
SO_0612	ClpXP protease specificity-enhancing factor	6,8	0,09
SO_0668	phage minor head protein	6,8	0,08
SO_0795	OsmC domain/YcaO domain-containing protein	6,0	0,08
SO_0809	azurin	8,2	0,002
SO_0872	polynucleotide adenylyltransferase PcnB	6,6	0,07
SO_0876	aminopeptidase PepB	6,1	0,08
SO_0913	Fic family protein	10,1	0,05
SO_0949	branched-chain amino acid transport system II carrier protein	9,3	0,06
SO_1056	methyl-accepting chemotaxis protein	7,6	0,06
SO_1060	penicillin-binding protein activator LpoB	10,3	0,0047
SO_1199	phosphoglucosamine mutase	7,4	0,07
SO_1264	FAD-binding oxidoreductase	9,2	0,07
SO_1531	tRNA uracil 4-sulfurtransferase ThiI	11,3	0,02
SO_1634	phosphatidate cytidylyltransferase	7,3	0,09
SO_1899	L,D-transpeptidase family protein	5,1	0,08
SO_2047	prolyl oligopeptidase family serine peptidase	7,6	0,05
SO_2064	YdbH domain-containing protein	9,4	0,06
SO_2420	signal peptide peptidase SppA	10,6	0,04
SO_2441	thiazole synthase	12,9	0,04

Old identifier	Function	Fold change	*p*-Value
SO_2570	DUF885 domain-containing protein	5,5	5,5
SO_2606	MlaD family protein	5,1	5,1
SO_2688	phage protein	8,7	8,7
SO_2710	DoxX family protein	6,9	6,9
SO_2725	LuxR C-terminal-related transcriptional regulator	18,2	18,2
SO_2766	M28 family metallopeptidase	5,2	5,2
SO_2880	Grx4 family monothiol glutaredoxin	9,4	9,4
SO_2889	cache domain-containing protein	7,2	7,2
SO_2956	phage tail tube protein	11,8	11,8
SO_2963	phage major capsid protein	9,7	9,7
SO_2964	head maturation protease, ClpP-related	45,8	45,8
SO_2973	lysozyme	12,1	12,1
SO_3023	tryptophan synthase subunit beta	14,7	14,7
SO_3083	insulinase family protein	12,2	12,2
SO_3105	rhodanese-like domain-containing protein	7,7	7,7
SO_3176	glycosyltransferase	6,3	6,3
SO_3186	glucose-1-phosphate thymidylyltransferase RfbA	9,2	9,2
SO_3188	dTDP-glucose 4,6-dehydratase	8,4	8,4
SO_3191	Wzz/FepE/Etk N-terminal domain-containing protein	13,2	13,2
SO_3206	chemotaxis response regulator protein-glutamate methylesterase	10,6	10,6
SO_3208	protein phosphatase CheZ	5,2	5,2
SO_3223	flagellar hook-length control protein FliK	5,2	5,2
SO_3227	flagellar motor switch protein FliG	5,0	5,0
SO_3233	flagellar export chaperone FliS	5,3	5,3
SO_3239	flagellar hook-associated protein FlgL	19,8	19,8
SO_3242	flagellar basal body P-ring protein FlgI	11,5	11,5
SO_3248	flagellar hook assembly protein FlgD	8,3	8,3
SO_3252	chemotaxis protein CheV	10,3	10,3
SO_3271	UDP-N-acetylglucosamine 4,6-dehydratase (inverting)	10,7	10,7
SO_3273	6-hydroxymethylpterin diphosphokinase MptE-like protein	9,4	9,4
SO_3386	DUF523 and DUF1722 domain-containing protein	11,3	11,3
SO_3440	phosphopyruvate hydratase	5,2	5,2
SO_3555	5-(carboxyamino)imidazole ribonucleotide synthase	6,6	6,6
SO_3772	TIGR04211 family SH3 domain-containing protein	6,6	6,6
SO_3787	DUF6088 family protein	6,4	6,4
SO_4047	c-type cytochrome	7,1	7,1
SO_4066	phosphoribosylaminoimidazolesuccinocarboxamide synthase	6,6	6,6
SO_4149	VCBS domain-containing protein	15,2	15,2
SO_4151	polysaccharide deacetylase family protein	23,8	23,8
SO_4208	porphobilinogen synthase	10,5	10,5
SO_4256	ribonuclease PH	7,3	7,3
SO_4323	EAL domain-containing protein	10,7	10,7

SO_4504	DUF3305 domain-containing protein	7,5	7,5
SO_4520	coproporphyrinogen III oxidase family protein	5,3	5,3
SO_A004	S9 family peptidase	8,2	8,2

Table S2. Oligonucleotides used in this study

Oligo ID	Sequence (5′ → 3′)	Orientation
SO4323	AGTTGATAACGGACTAGCCTTATTTTAACTTGCTAT TTCTAGCTCTAAAACACTTCTTCATCTAGGGATTGG CAACCATTATCACCGCCAGAGGTAAAATAGTCAAC ACGCACGGTGTTA	Forward
	TAACACCGTGCGTGTTGACTATTTTACCTCTGGCGG TGATAATGGTTGCCAATCCCTAGATGAAGAAGTGT TTTAGAGCTAGAAATAGCAAGTTAAAATAAGGCTA GTCCGTTATCAACT	Reverse

Table S3. All primers used in this study

Primer Nr	**Sequence**	**Target**	**Source**
4399	CAGGATAGCTTTAGCGTCA	For Sanger seq – stop codon	This study
4400	CCGTGTTTTCTGGACGA	For Sanger seq – stop codon	This study
4505	TCATTCAGGTTTATTTAAGTGAT	For Sanger seq – stop codon	This study
4506	ATGCAATTACCTCCCATC	For Sanger seq – stop codon	This study
4507	ATGACACTGTTTAGACAGAT	For Sanger seq – stop codon	This study
4508	TTATTCGATATTCTCTGGTGG	For Sanger seq – stop codon	This study

6.2. Supplementary Figures:

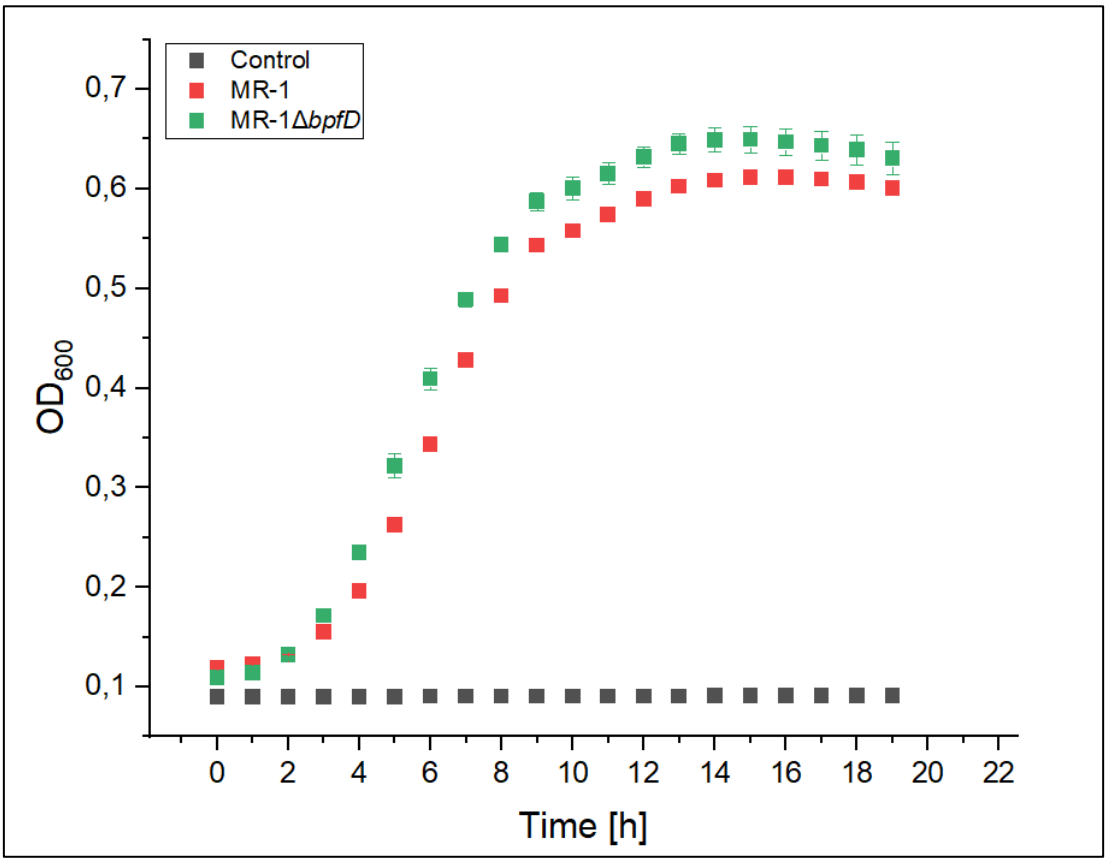

Figure S1. Growth curves of *Shewanella oneidensis* wild-type and mutant strains. Optical density at 600 nm (OD_{600}) was measured over time to assess the growth of the control, wild-type MR-1, and mutant strains MR-1*Δdgc* and MR-1*ΔbpfD*. Cultures were incubated under identical conditions, and values represent the mean ± standard deviation from replicates.

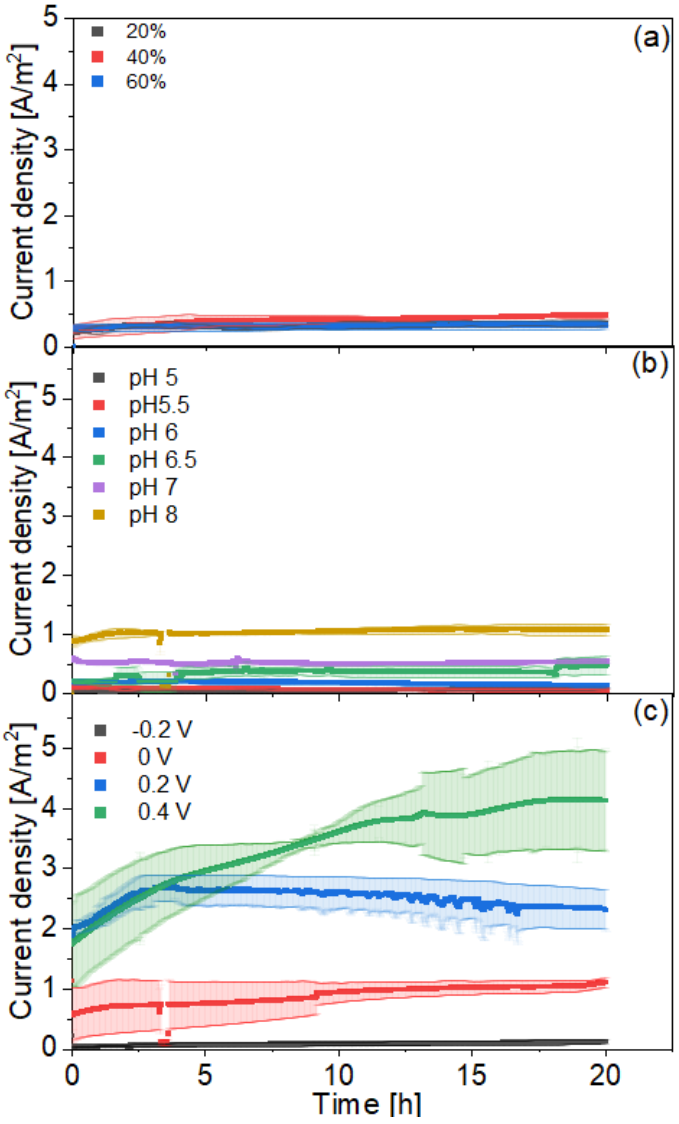

Figure S2. Current density profiles, until reaching steady values, obtained from the examined cylindrical microbial electrolysis cells (C-MECs) under varying (a) hydrolysate concentrations (i.e., 20%, 40%, and 60%), (b) pH values (i.e., 5–8) at a anodic potential of 0 V vs. SHE and 40%-hydrolysate, and (c) anodic potentials (i.e., −0.2 V to 0.4 V vs. SHE) at pH 8 and 40%-hydrolysate. Data represent the mean of triplicate experiments; shaded areas indicate standard deviation.

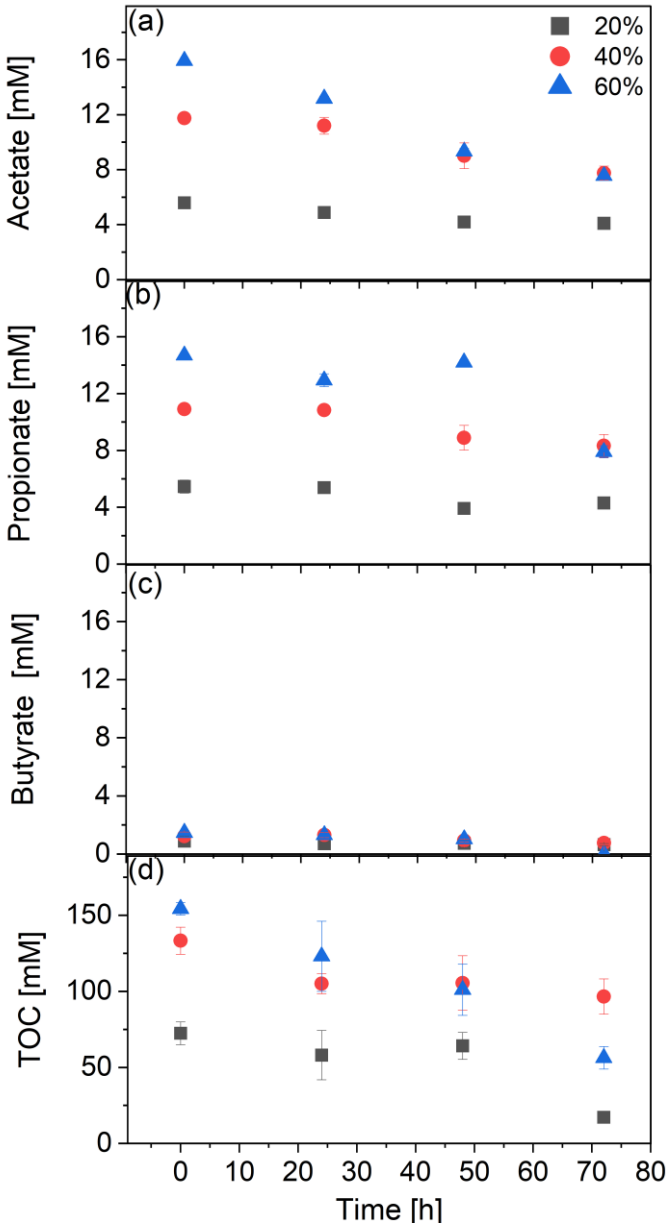

Figure S3. Variations in acetate (a), propionate (b), butyrate (c), and total organic carbon (TOC) concentrations over time in cylindrical microbial electrolysis cells (C-MECs) fed with different hydrolysate concentrations of 20%, 40%, and 60%.

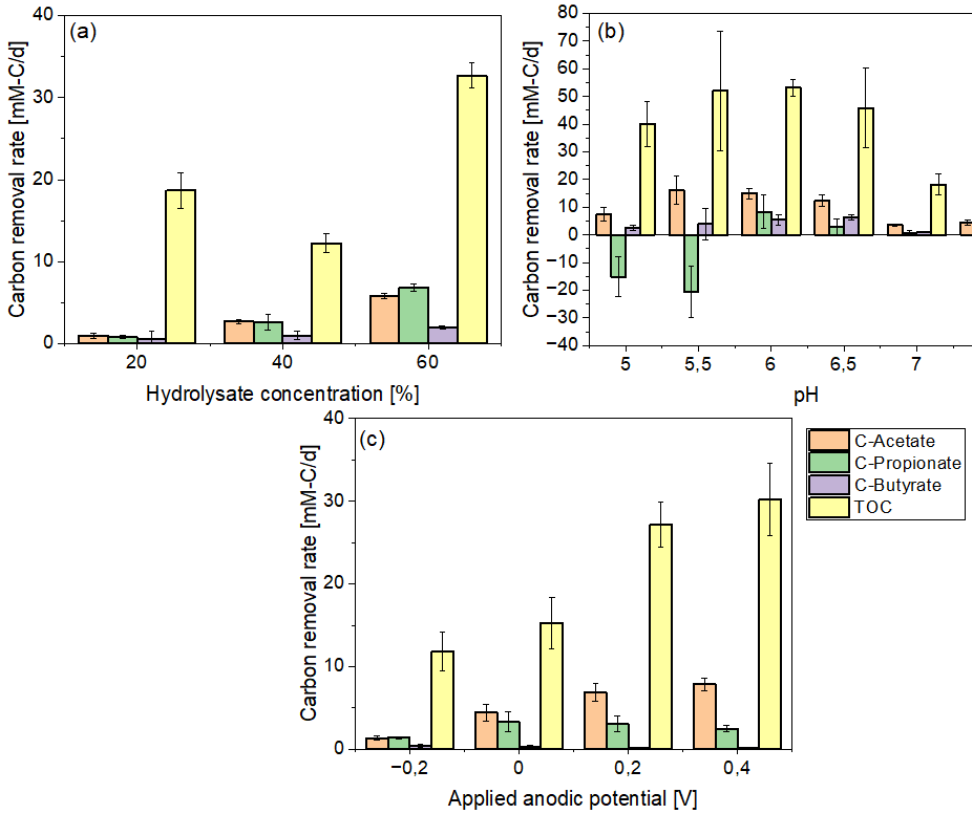

Figure S4. Carbon removal rates obtained from the profiles of total organic carbon (TOC) in comparison with those obtained from each measured volatile fatty acid (VFA) (i.e., acetate, propionate, and butyrate) under different (a) hydrolysate concentrations, (b) pH levels, and (c) applied anodic potentials.

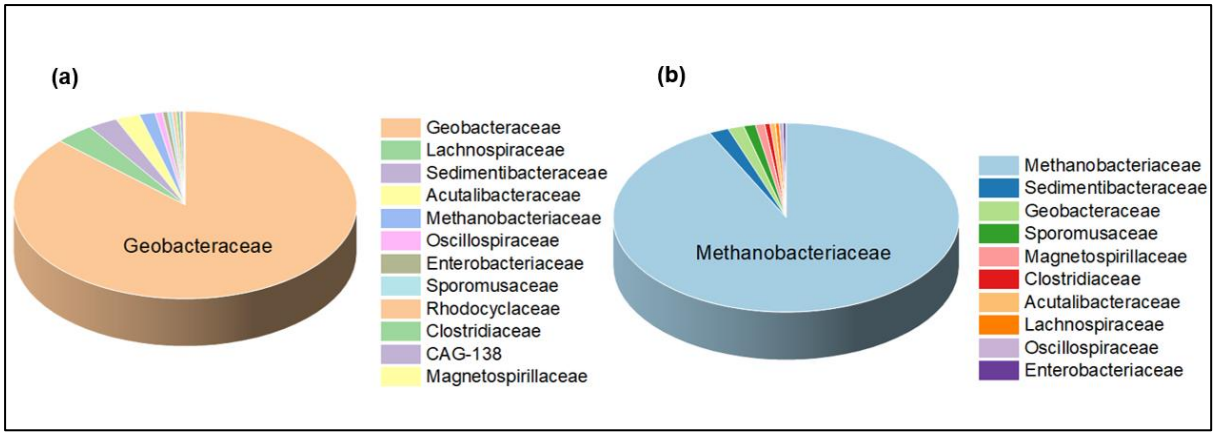

Figure S5. Microbial community composition at the family level on the a) anode and b) cathode of the rotating disk bioelectrochemical reactor (RDBER).

Acknowledgement

A doctoral thesis may carry only one name on its cover, but it is never truly written alone. Behind every experiment, every late evening in the lab, every failed attempt, every small success, and every final sentence, there are people who have contributed in countless ways.

This work was shaped not only by scientific ideas and experimental results, but also by guidance, patience, encouragement, friendship, and support. During the long and sometimes exhausting path of this PhD, I was fortunate to be surrounded by many people who helped me continue, improve, and believe in the value of this work.

First of all, dear Johannes, I would like to express my deepest gratitude to you. Thank you for your unconditional support over the past years, for your patience during the first year of my PhD while I was still finding my place and becoming integrated into the group, and for your incredible understanding and support during my pregnancy and afterwards. I am also deeply grateful for your brilliant ideas, your scientific guidance, and the trust you placed in me throughout this journey. Your support has meant a great deal to me, both professionally and personally.

Dear AG Gescher,

I could not have wished for a better group of people to share this PhD journey with. Thank you for the support, encouragement, kindness, and friendship you have given me over the past years. The atmosphere in the group, the willingness to help each other, and the many moments we shared made this time not only scientifically valuable, but also personally meaningful. I am truly grateful to have been part of this group.

Ahmed, ooof, Ahmed! I honestly cannot imagine what my life and my work would have been like without you. You were always there to answer my questions, help me solve problems, and support me whenever I needed it. The long working days, the late evenings in the lab, our many discussions, and even our occasional arguments taught me a lot, not only scientifically, but also personally. Through working with you, I learned the importance of listening, staying grounded, and seeing things from another perspective.

To my office,

You have all been truly wonderful, and each one of you has grown very close to my heart. Thank you for creating a place that was not only an office, but also a space full of kindness, laughter, support, and friendship.

Beri, thank you for your endless positive energy, your massages, your hugs, and your Turkish coffee. Without you, the Mensa would have been just a place to eat, but with you, even the simplest moments became joyful and special. You truly have a heart of gold, and I am so happy and grateful to have you in my life as my bestie. Beni, thank you for all the breakfasts, the morning welcomes, and the funny afternoon goodbyes we shared. I am also very happy that, although the characters in the books you read never seemed to find love, you found true love in your own life. Leoni, my kind, sympathetic, and wonderfully organized roommate, thank you for all the conversations we had about so many different things. I always appreciated your care for the environment and your thoughtful way of seeing the world. Thank you also for your efforts with my PhD hat, which meant a lot to me.

My lovely Sigi, thank you for all your kind and positive morning greetings and for your everyday support in the lab. I truly believe that AG Gescher is very lucky to have you there. Your place will forever remain in my heart as a friend. Laura, thank you for supporting me throughout this journey, for helping me with all the forms I needed to fill out, and for all the

beautiful conversations we had about our pregnancies and later about our sons. Maybe you do not know it, but I learned a lot from you, also in my personal life. Jonas, thank you for your calm and cool character, for helping me understand molecular biology, and for solving so many of my technical problems. René, thank you for your sense of humor, your curiosity, the “chip knowledge” you so generously shared with me, and of course for your very special fashion style. Vivi, after every message I received from you, even after I was no longer there, I asked myself how one person could be so kind and sympathetic. My feelings about your character are beyond words. Sri, thank you for offering me yoga classes during my pregnancy; they truly made that time easier for me. Thank you also for the beautiful red hat you made for Reymon and for your detailed and honest opinions about my clothes and appearance. Carmen, thank you for visiting us in Wuppertal when I was far away from the group. I learned from you how to think about my experiments in much more detail, and I believe this is one of the qualities that makes you special in your career. Lukas, thank you for being so organized and protective when it came to the lab. Although your serious manner sometimes scared me at first, with time I realized that behind it there is a very kind and responsible person. Janek, thank you for all your help regarding the washing machine and for being a handsome king. Chrisi, Daniel, Daniela, and Fernando, thank you for all your efforts on my Dr.-Wagen. You made it truly special for me. Nadin, thank you for being such an incredibly helpful and kind soul.

Many, many thanks also go to everyone outside the lab who not only put up with my sometimes deeply stressed nature, but also did everything they could to help me get through this time. A very special thank you goes to Akram and Samstagabends group (Aida, Mahya,Leo and Mohammad) for our long and beautiful friendship. I am deeply grateful that we have been by each other’s side for so many years, cheering each other on no matter where we are. Thank you for all the memories, the laughter, the honesty, and of course for all the secrets we have shared, which made our friendship even stronger. A special thank you also goes to Zahra and Abolfazl.

Although our friendship has not been long, it has become very deep and meaningful to me. Thank you for coming to Hamburg to be with me during my defense. Your presence on that special day meant a lot to me.

Last but not least, a massive thank you goes to my family.

Hamideh, thank you for supporting Mum while I have been far away. Knowing that you are there and that you take care of everything has always given me comfort and peace of mind. Mum, thank you for teaching me how to be strong in life and how to keep doing my best, no matter how difficult things become. You, more than anyone else, have shaped the person I am today, and I am deeply grateful for your endless love, support, and strength.

Reymon, my son, thank you for bringing so much light into my life and for letting me experience the amazing feeling of being a mother. Your presence has given my life a new meaning and has made it more special.

Behzad, my love, thank you from the bottom of my heart. I am sorry for all the weekly journeys you had to make between Düsseldorf and Hamburg for three years just to visit me. Thank you for your love, support, and encouragement throughout the past years. Thank you also for your patience during the times when you had to take care of Reymon without my help, while I closed the door to write my thesis and papers. Without you, your love, and your patience, this would have been impossible. But we did it, my love. We did it together!